

**ENERGY FOCUSING THROUGH
DISTRIBUTED BEAMFORMING IN
INTERNET OF THINGS : MECHANISMS
AND APPLICATIONS**

BY XIAORAN FAN

A dissertation submitted to the
School of Graduate Studies
Rutgers, The State University of New Jersey
in partial fulfillment of the requirements
for the degree of
Doctor of Philosophy
Graduate Program in Electrical and Computer Engineering
Written under the direction of
Dr. Dipankar Raychaudhuri
and approved by

New Brunswick, New Jersey

October, 2020

ABSTRACT OF THE DISSERTATION

Energy Focusing through Distributed Beamforming in Internet of Things : Mechanisms and Applications

by Xiaoran Fan

Dissertation Director: Dr. Dipankar Raychaudhuri

In this thesis, we discuss the feasibility of using distributed antenna systems to facilitate the deployment of IoT devices. Our approaches are inspired by Fresnel zone plates focusing light. In our design, in a manner analogous to creating a Fresnel zone plate, we discretize the zone plates into multiple independent phase shifters. Each phase shifter is a far-field RF transmitter in our system. Specifically, by coherently combining the phase of each RF transmitter in a 3D distributed antenna system, the system forms an *energy ball* at the target location where the energy density level is significantly higher than the energy density level at any other locations. Our results demonstrate that this energy ball has great potential to be leveraged to solve many fundamental problems in IoT and enable exciting IoT applications.

In the first part of this thesis, we discuss how a distributed antenna system contributes to an IoT system's confidentiality gains. Ensuring confidentiality

of communication is fundamental to securing the operation of a wireless IoT system, where eavesdropping is easily facilitated by the broadcast nature of the wireless medium. By applying distributed beamforming among a coalition, we show that a new approach for assuring physical layer secrecy, without requiring any knowledge about the eavesdropper or injecting any additional cover noise, is possible if the transmitters frequently perturb their phases around the proper alignment phase while transmitting messages. This approach is readily applied to amplitude-based modulation schemes, such as PAM or QAM. We present our secrecy mechanisms, prove several important secrecy properties, and develop a practical secret communication system design.

In the next part of this thesis, we discuss how a distributed antenna system contributes to an IoT system’s energy efficiency gains. In order to meet the ever-growing energy demand from the next billion IoT devices, we present a new wireless power transfer (WPT) approach by aligning the phases of a collection of radio frequency (RF) energy chargers at the target receiver device. Our approach can ship energy over tens of meters and to mobile targets. More importantly, our approach leads to a highly asymmetric energy density distribution in the charging area: the energy density at the target receiver is much higher than the energy density at other locations. It is a departure from existing beamforming based WPT systems that have high energy along the energy beam path. Such a technology can enable a large array of batteryless IoT applications and render them much more robust and long-running. Thanks to its asymmetric energy distribution, our approach potentially can be scaled up to ship higher level of energy over longer distances.

We design, prototype, and evaluate the proposed distributed antenna system. We implement the testbed that consists of 17 *N*210 and 4 *B*210 Universal Software Radio Peripheral (USRP) nodes, yielding a $20 \times 20 \text{ m}^2$ experiment area. Depending on system parameter settings, we measure that the eavesdroppers failed to

decode 30% – 60% of the bits across multiple locations while the intended receiver has an estimated bit error ratio of 3×10^{-6} . Our results also show the system can deliver over 0.6mW RF power that enables batteryless mobile sensors at any point across the area.

In the last part of this thesis, we build a distributed beamforming system that can continuously charge tiny IoT devices placed in hard-to-reach locations (*e.g.* medical implants) with consistent high power, even when the implant moves around inside the human body. To accomplish this, we exploit the unique energy ball pattern of the distributed antenna array and devise a backscatter-assisted beamforming algorithm that can concentrate RF energy on a tiny spot surrounding the medical implant. Meanwhile, the power levels on other body parts stay at a low level, reducing the risk of overheating. We prototype the system on 21 software-defined radios and a printed circuit board (PCB). Extensive experiments demonstrate that the proposed system achieves 0.37 mW average charging power inside a 10 cm-thick pork belly, which is sufficient to wirelessly power a range of commercial medical devices. Comparisons with the state-of-the-art powering approaches shows that our system achieves $5.4\times$ – $18.1\times$ power gain when the implant is stationary, and $5.3\times$ – $7.4\times$ power gain when the implant is in motion.

Acknowledgements

There are many people that have earned my gratitude for their contribution to my time in graduate school. This thesis would not have been possible to complete without the invaluable support and guidance from all of them.

I would like to express my earnest gratitude to my advisor, Yanyong Zhang. Yanyong opened the door of my research. She has always given me guide, advice, and encouragement with a touch of softness and caringness. She taught me how to identify and formulate a research problem, how to tackle down the problem in scientific ways, how to express and write ideas, and how to balance my relax and work time to achieve a healthy research experience. More importantly, she shaped me into an independent and self-motivated researcher. She forged my mental-toughness and fearlessness in confronting any challenge. It is indeed my life long treasure.

I am thrilled to be advised by Dr. Rich Howard during this wonderful 5 years of my Ph.D. life. Rich is my spiritual leader. His expansive, brilliant and critical thinking deeply inspires me. He taught me thinking critically and helped me build my bull-shit-detector. He always encourages me to try as much as I can to understand the fundamentals when encountering any problem. His viewing the world in a physical way gives me a deep impact in my way of thinking. My Ph.D. journey won't be so enlightened, joyful and fruitful without him.

Special thanks to Prof. Wade Trappe. I have always been inspired by the depth of his technical insight, his passion about exploring and solving problems, and his delicate approach towards research. I have enjoyed the time work with him a lot. Further, I also wish to thank many collaborators, fellow students and

friends, who have influenced my views and efforts during my time inside and outside WINLAB. I cannot thank them enough for all the interesting discussions and fun moments we had. And I would like to thank all the WINLAB faculties and staffs for keeping up such a lively and productive environment.

Besides, I am also very grateful to the rest of the dissertation committee. It's my honor to have Prof. Dipankar Raychaudhuri to be my committee member. His insightful suggestions have driven me to broaden my research and progressively improve this dissertation. I would also like to express my special gratitude to Dr. Longfei Shangguan for serving as my external member and being my lifelong friend.

I would like to give my thank to my parents and my family members, all of whom made countless sacrifices to raise me and to give me the best possible education. They stand with me no matter what happens. Their encouragement let me grow to be strong.

Lastly, I would thank my girlfriend Mouli for all the love and accompany. You are always the one to share happiness and sorrow. You are always the special one in my life.

Dedication

To my girlfriend Mouli Luo and my parents Xiongfei Fan and Yulan Huang, for their love, continuous support and encouragement.

Table of Contents

Abstract	ii
Acknowledgements	v
Dedication	vii
List of Tables	xii
List of Figures	xiii
1. Introduction	1
1.1. Distributed Antenna System	1
1.2. When IoT Meets DAS	2
1.3. Road Map	5
2. <i>Secret-Focus</i>: A Practical Physical Layer Secret Communication System by Perturbing Focused Phases in Distributed Beamforming	7
2.1. Introduction	7
2.2. Background on Secret Communication Systems	10
2.3. Perturbing Aligned Phases for Secret Communication	11
2.3.1. Mechanism 1: Combining Phases Increases μ_y	14
2.3.2. Mechanism 2: Dithering Phase Hurts Eve	18
2.3.3. Effectiveness of the Two Mechanisms	20
2.4. Putting Together a <i>Secret-Focus</i> Communication System	22
2.4.1. Trial-and-Error Distributed Phase Alignment	23
2.4.2. Amplitude Modulation (AM) Based Secret Communication	24

2.4.3. An Example Scenario	26
2.5. Prototype Evaluation	26
2.5.1. <i>Secret-Focus</i> Makes Eavesdropping Impossible	27
2.5.2. Low Decoding Error for Bob vs High Error Rate for Eves .	29
2.5.3. Impact of Important System Parameters	31
2.6. Conclusion	32
3. <i>Energy-Ball</i>: Wireless Power Transfer for Batteryless Internet of Things through Distributed Beamforming	33
3.1. Introduction	33
3.2. Related work and Motivation	37
3.2.1. Electromagnetic Radiation Based Energy Harvesting and Transferring	37
3.2.2. WPT Energy Density Distributions and Their Implications on Safety	39
3.3. <i>Energy-Ball</i> Design Details	41
3.3.1. Overview	41
3.3.2. Energy Transfer through Phase Alignment	41
3.3.3. Charging Mobile Receiver	46
Channel Reciprocity and Channel Correlations	46
Phase Estimation Using Adaptive Kalman Filter	49
3.4. Building <i>Energy-Ball</i> Testbed Using USRPs	50
3.4.1. Testbed Setup	51
3.4.2. GNU Radio Implementation	53
<i>Transmitter Side</i>	54
<i>Receiver Side</i>	55
Robust Pulse-width Modulation Feedbacks	56
3.4.3. Experimentation and Measurement Tools	57

Energy Harvester and Low-Power IoT Sensors:	57
Energy Measurement Robot:	59
Spectrum Analyzer and USRP Calibration:	59
3.5. Evaluation	60
3.5.1. Energy Density Distribution of <i>Energy-Ball</i>	60
3.5.2. <i>Energy-Ball</i> Delivers Energy at Any Point across the Room	63
3.5.3. <i>Energy-Ball</i> Charges Mobile Receivers	64
3.5.4. Application Example- Charging Low-Power PIPs Sensors .	65
3.6. Conclusion	67
4. Towards Flexible Wireless Charging for Medical Implants Using Distributed Antenna System	68
4.1. Introduction	68
4.2. Scope	73
4.3. Beamforming Without CSI Feedback	74
Algorithm overview	75
An example	75
4.4. System Design	76
Carrier Signal	77
4.4.1. Backscatter Assisted Beamforming (BAB)	78
Backscatter Design	82
Beamforming Power Change Inference	84
4.4.2. Cold Start	85
4.4.3. Balancing Convergence and Delay	88
4.5. Implementation	88
4.5.1. Testbed Setup	88
4.5.2. Software Implementation	90

4.5.3. RF Power Limit	91
4.6. Evaluation	92
4.6.1. Micro-benchmark	92
Chirp Synchronization	93
Cold Start	93
Beamforming	95
4.6.2. Field Study	98
4.7. Related Work	102
4.7.1. Wireless Charging in Bioelectronics	102
4.7.2. Backscatter Communication	104
4.8. Discussion	104
4.9. Concluding Remarks	105
4.10. Appendix	106
4.10.1. $P_{CCS(0)}$ extraction	106
4.10.2. Optimal phase searching bound estimation	108
5. Conclusion and Proposed Research	110
5.1. Summary	110
5.1.1. Contribution Summary	110
5.2. End Note	111
5.2.1. IoT identifications using PHY layer fingerprints	111
5.2.2. Channel state information (CSI) inference for massive phase arrays	112
5.2.3. Make the sweet spot of your stereo follows you	112
5.2.4. RF interaction in Biology	113
References	114

List of Tables

2.1. Average Decoding errors statistics for Bob and 3 Eves. Bob has extremely low BER while Eves' BER are over 30%.	28
4.1. The power loss at different part of the round-trip path between the transmitter (outside body) and the receiver (inside body). The transmission power is set to the maximum value under FCC regulation.	77
4.2. Power requirements of several commercial medical implants. In-N-Out can achieve average $372 \mu\text{W}$ by using 24 slave radios, which is sufficient to power up most of commercial pacemakers and cardiac defibrillators, as well as many neuro-stimulators and CIDRs.	98

List of Figures

1.1.	Comparison of the energy density heatmap generated by (a) a linear antenna array and (b) a distributed antenna array with the same number of antennas (24 in both cases). The receiver is placed at the center of the rectangular area.	2
2.1.	(a) shows a beamforming based secure communication system, in which artificial noise is used to jam Eve. (b) illustrates <i>Secret-Focus</i> in which distributed transmitters first align their phase at Bob and then perturb their phases around the alignment phase to focus the secret message at Bob.	11
2.2.	Theoretical secrecy rate as a function of α_y and α_z . Communication is secret when we have $\alpha_y > \alpha_z$, and while keeping α_z small enough.	13
2.3.	(a) Alice generates low bits and high bits following amplitude based modulation. (b) shows a typical distribution of bits received by Bob. Received bits follow a mixed (complex) Gaussian distribution.	14
2.4.	The geometric relationship between Alice, Bob and Eve, which is used in (2.3) and (2.4) when calculating the normalized RSS at Eve's location $Y(d)$	15
2.5.	(a) Analytic results for the normalized RSS function $Y(d)$ in (2.4), where RSS decreases with d . (b) Numerical results of RSS versus d , where 100 transmitters were placed in a circle around the target. The numerical results match analytical results exactly.	16

2.6. (a) Simulation results of RSS distribution in a $1m$ by $1m$ area around Bob. It is clear that the energy is sharply focused around the target location. In (b), we decrease the number of transmitters to 30, and place them on a half circle. Note the target receiver is also not placed at the center. As can be seen, even though the energy focus is wider, the peak is still very pronounced compared to other locations.	17
2.7. (a) The analytical results for $G(d)$ in (2.11). The envelop of $G(d)$, marked in blue, shows that Eve's RSS variation increases with d . (b) The distribution of $G(d)$ in a $2m \times 2m$ area around Bob shows the same trend. We observe the lowest G value at Bob's location.	19
2.8. (a) Raw RSS at Eve for a broadcast channel (neither mechanism employed), (b) raw RSS at Eve for a NO-Perturb system (only mechanism 1 employed), (c) raw RSS at Eve for <i>Secret-Focus</i> (both mechanisms employed), and (d) raw RSS at Bob for <i>Secret-Focus</i> . In this example, only <i>Secret-Focus</i> is able to hinder Eve from decoding received signal and provide secret communication to Bob. .	20
2.9. The <i>Secret-Focus</i> prototype consists of 16 transmitter USRPs. The deployment area of our prototype is $20 \times 20 \times 3 m^3$	21
2.10. <i>Secret-Focus</i> consists of two main stages: distributed phase alignment, and secret communication with phase perturbation.	23
2.11. (a) Histogram of Bob's RSS values, where high bit symbols and low bit symbols are clearly separated. (b) Histogram of Eve's RSS values, where high bit symbols and low bit symbols are largely mixed.	24
2.12. A $7 \times 7 m^2$ test area. We placed Bob (red) in the center, and Eve at 100 possible locations (blue). Eve locations not uniformly distributed, but denser towards the center.	27

2.13. The measured average α_{Bob} is significantly higher than α_{Eve} at all 100 Eve locations. Thus, Bob can have secret conversation with Alice in the presence of Eve at these 100 locations.	27
2.14. Extreme Eve locations outside of the test area. $BER = 12.45\%$ when she is side-by-side with Bob, and $BER = 7\%$ when she is 15cm (half a wavelength) away from one transmitter antenna.	28
2.15. <i>Secret-Focus</i> has much lower α_{Eve} values than Broadcast and NO-Perturb. It provides better support for secret communication.	29
2.16. BER vs. a_L	30
2.17. BER vs. ϕ	30
2.18. BER vs. N	30
2.19. BER vs. t_{sb}	30
3.1. Energy density distribution for beamforming.	34
3.2. Energy density distribution for <i>Energy-Ball</i>	34
3.3. When we place the receiver in the center of the transmitter square, (a) shows the energy distribution around the receiver in a 2D plane and (b) energy distribution under a GWSSUS channel, (c) pictorially shows the ‘energy ball’ relative to transmitters in a 3D space, where blue dots mark the transmitters.	44
3.4. Simulated energy distribution around the target receiver (target receiver is placed at the center) with (a) 8 transmitters (b) 16 transmitters (c) 25 transmitters (d) 50 transmitters.	45
3.5. Energy level distribution in different transmitter-receiver placement settings: (a) receiver placed at the center of transmitter square; (b) receiver placed in the transmitter square, but not the center; (c) receiver placed outside of transmitter square, but close; (d) receiver placed further away to the transmitter square. Among these four cases, the energy ball is formed in the first three case.	46

3.6. Each radio device has separate ports for transmitting and receiving. We define the channel from the transmitter to receiver as ‘energy charging’ channel, and the channel from the receiver to transmis- ter as ‘feedback’ channel. These two channels work at different frequencies but are correlated.	47
3.7. (a) PDD at 915MHz and 964MHz channel. Measurement results indicate the PDDs are correlated for these two different channels. (b) Estimated energy charging channel PDD from the adaptive Kalman filter. We also show the measured energy charging channel PDD as the ground-truth. This result suggests our phase estima- tion algorithm for mobile receiver is indeed accurate.	48
3.8. Real world <i>Energy-Ball</i> testbed.	50
3.9. The illustration of <i>Energy-Ball</i> setup.	50
3.10. (a) Convergence speed comparison for algorithms in different ran- dom adjustments N and simulated annealing. Phase alignment with larger N converges faster. (b) In the first 150 seconds, we turned on/off and measured 12 transmitters one by one. After time 150, we turn on all transmitters and started phase alignment. RSS quickly converges after that.	52
3.11. <i>Energy-Ball</i> TX and RX signal processing flow.	55
3.12. (a) We use different beacon width to indicate feedback informa- tion. Only one threshold is used to differentiate environmental noise and beacons. (b) Powercast P2110-EVB board and our PIPs sensor board. (c) Energy measurement robot scans Chilitags (on the ceiling) for navigation.	57

3.13. Using the topology shown in Figure 3.9, we measure the power level distribution of <i>Energy-Ball</i> in a 6×6 meter area centered at the receiver. (a) presents the 3D view of distribution, while (b) presents the histogram of the power level measurements. The distribution clearly shows that the energy density level at the receiver (marked by the red X) is much higher than that at other spots within the measurement area.	60
3.14. Comparison experiments show the energy distribution of beam-forming WPT systems. (a) Real world set up of our 16 by 16 beamforming USRP Rack. (b) Measured received power in the area between the beamforming rack and target receiver. (c) Statistics of measured power, there are still lots of locations have received power greater than the target receiver.	61
3.15. In our $20 \times 20 m^2$ test area, we place the <i>Energy-Ball</i> receiver at 42 locations, in which location 1 is the center of the area and the other 41 locations are randomly chosen. We show the received power at each of these receiver locations here. Results show the received power at most of the locations is higher than the received power level at the center of the deployment area (location 1).	63
3.16. (a) We place the receiver on the robot, which moves at a constant speed along a 0.6 meter long trajectory. We measure received power at 13 different positions on the trajectory (transmitters are placed at 4 corners). (b) The received power percentage values at the mobile receiver with different moving speeds. The rightmost box represents the received power percentage value when <i>Energy-Ball</i> is turned off (transmitter phases are still aligned to the original receiver location).	65

3.17. In this experiment, we investigate whether sensors at locations other than the target can be powered. (a) Data reported by PIPs, including timestamp, dropped packet ID, server ID, sensor ID, RSSI and sensed data. (b) shows the experiment set up where the target sensor (O) is in the center of the red block, and A , B , C , and D are within the red blocks, 30cm away from O , and a few others are located in the blue squares. (c) shows how sensors at different locations operate when the energy is focused at O . O can work perfectly, $A-D$ can work partially even though they are only 30cm away, and those sensors that are placed in the blue blocks do not have sufficient power to sense or communicate.	67
4.1. An illustration of In-N-Out deployment. The leader radio coordinates multiple slave radios to charge the pacemaker during bedtime.	69
4.2. The energy heatmap produced by (left) a linear 24-antenna array and (right) a distributed 24-antenna array. The linear antenna array produces an energy beam spreading in the direction of the target, while the distributed antenna array produces an energy spot surrounding the target.	71
4.3. A running example of the one-bit phase alignment algorithm with three transmitters. Each transmitter adjusts its phase based on the feedback from the receiver and gradually converges to the optimal phase alignment.	76
4.4. RSS measurements in different time offset settings. A larger time offset leads to a higher RSS fluctuation rate. The RSS converges to a relatively stable value when all chirps are tightly time synchronized.	79
4.5. A snapshot of RSS samples (top) and the fluctuation rate (bottom) in one period. The fluctuation rate decreases with time. The signal amplitude converges when the two radios are synchronized.	80

4.6. Our monotonic backscatter radio design (left) and the PCB board prototype (right). We envision the board size can be reduced to the sub-centimeter scale when implementing In-N-Out on an Integrated Circuit (IC)	81
4.7. Non-monotonic (top, passive RFID [1]) and monotonic backscatter radio (bottom, In-N-Out). The top figure is adapted from [1].	83
4.8. (a) RSS and (b) $P_{CCS(0)}$ measurements of the received backscatter signal as the carrier signal power grows linearly.	84
4.9. Beamforming energy patterns with different phase perturbations: (a) optimal phase alignment, (b)-(d) with different phase perturbations. With phase perturbations, we observe an enlarged main lobe and many side lobes. These side lobes can provide sufficient energy to wake up the backscatter radio.	87
4.10. Phase perturbation range σ analysis (a) Scanning ratio CDF vs. number of perturbations. (b) Scanning ratio values after 100 perturbations vs. σ	88
4.11. Testbed setup. Our testbed consists of 17 USRP N210 and four USRP B210 nodes, all mounted on the ceiling of an office building.	89
4.12. Message flow of In-N-Out	90
4.13. CDF of residual time offset without and with chirp synchronization.	91
4.14. Chirp synchronization delay vs. number of slave radios.	91
4.15. Cold start success rate (left) and delay (right) vs. number of slave radios.	91
4.16. Cold start success rate (left) and delay (right) vs. L-B distance. .	91
4.17. RSS during a beamforming episode.	95
4.18. Beamforming delay vs. number of slave radios.	95
4.19. Power percentage vs. chirp bandwidth.	95

4.20. Power percentage vs. backscatter orientation.	95
4.21. Power percentage across different media.	95
4.22. In-tissue 3D power distribution.	95
4.23. Power percentage vs. slave count.	96
4.24. Beamforming power samples.	96
4.25. Experimental setup for mobile cases.	99
4.26. Average beamforming power vs speed.	99
4.27. CDF of the beamforming power. ($v = 5 \text{ cm/s}$)	99
4.28. Beamforming power samples. ($v=1 \text{ m/s}$)	99
4.29. Optimal phase searching bond and its corresponding 7 order polynomial fitting curve in the context of backscatter assisted beamforming.	107

Chapter 1

Introduction

1.1 Distributed Antenna System

Recently, wireless access point designs are undergoing a major shift from co-located antennas to distributed antennas connected to a centralized processor for signal processing [2, 3]. The primary reason behind this shift is that the distributed antenna systems (DAS) achieve better spatial diversity, higher cell and network capacity, and scale better to the increasing number of end-devices [4, 5]. Today, major cellular providers like Verizon, AT&T, and Vodafone have already planned their DAS worldwide, *e.g.*, cloud radio access networks (C-RAN). In wireless local area networks (WLAN), we also witness the trend of Wi-Fi access points coupled with multiple extenders per geographical area. These spatially distributed transmitters/receivers essentially form a distributed antenna system.

Noticing the proliferation of distributed antenna systems in both global and local settings, in this thesis we ask an important question – *is it possible to facilitate the deployment of IoT devices with distributed antenna systems?* Our discussion in this thesis gives an affirmative answer and points out the way to achieve this: performing *beamforming* on distributed antenna systems, or *distributed beamforming* for short. Specifically, by coherently combining the phase of each antenna in a 3D distributed antenna system, we form an *energy ball* at the target location where the energy density level is significantly higher than the

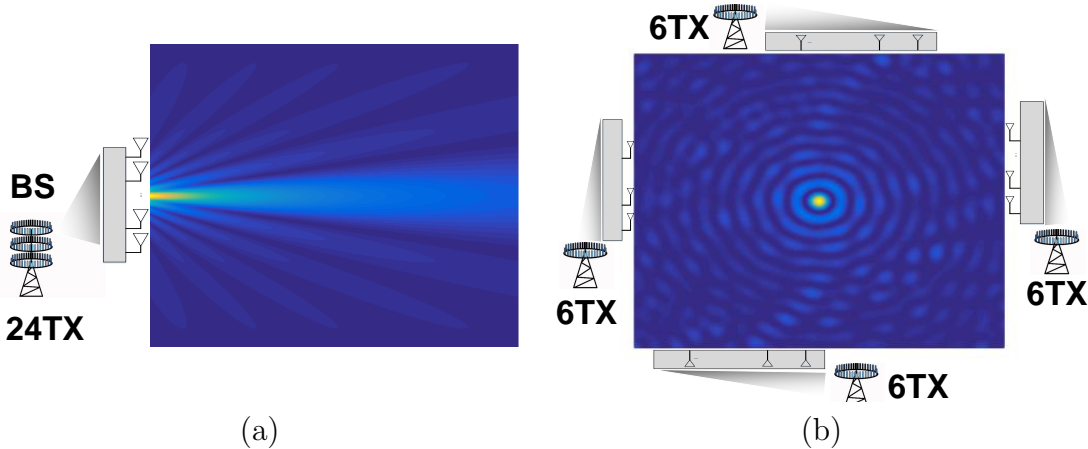


Figure 1.1: Comparison of the energy density heatmap generated by (a) a linear antenna array and (b) a distributed antenna array with the same number of antennas (24 in both cases). The receiver is placed at the center of the rectangular area.

energy density level at any other locations¹. This energy ball differs from the conventional energy beam generated by the co-located antenna array, as shown in Figure 1.1.

1.2 When IoT Meets DAS

The Internet of Things (IoT) envisions an ubiquitous connectivity among billions of everyday objects. Today's IoT devices are energy efficient, consuming orders of magnitude lower power than the conventional sensors on computing, sensing, and communication. Today's IoT devices are also becoming increasingly smaller, which makes them deployable anywhere, on any item, *e.g.*, swallowed or injected into human body for vital signs monitoring [6], placed on a tiny insect for habitat monitoring [7]. While these IoT devices have proved their utilities in many ways, they are still facing fundamental challenges such as security and energy efficiency when deployed at scale or operated in long-term periods. On the other hand, the unique energy pattern of DAS has been largely overlooked since the industrial

¹This energy ball maps to an energy disk in 2D space.

and research focus in DAS are synchronization, communication throughput gain, and deployment. This energy pattern in fact provides a plausible angle to solve fundamental challenges in IoT systems. We envision at least three ways DAS can facilitate IoT deployment:

Secure IoT communication. By examining how the transmitter signals coherently combine at the receiver, we show that phase alignment accomplishes highly efficient secret communication against eavesdroppers without knowing their location, nor introducing any additional signal/noise. Also, to engage in secret communication, a distributed phase alignment system only needs to introduce very minor modifications to their normal transmission procedure. Once the transmitters' phases are adjusted so that they are aligned at the receiver, they may start to communicate secretly to the receiver, by periodically dithering its phase around the proper alignment phase during transmission. In this way, the system naturally achieves secret communication. Firstly, the secret recipient's SNR is largely increased by aligning the phases at the intended recipient (and the SNR at eavesdroppers' locations are significantly decreased). After the phase alignment is achieved, slight dithering of the phases has negligible impact on the alignment, but can create high received signal strength (RSS) variation at other locations, hindering anyone else from decoding the signal. Thirdly, it does not involve utilizing interference for secrecy, which complicates system design, requires complex interference cancellation and decoding schemes, which are unlikely to be allowed in practical systems.

Pushing the Limit of Wireless Power Transfer for Batteryless IoT.

As people endeavor to deliver higher amount of energy over longer distances, *it is hard to strike the balance between delivering high energy level at target location and lowering energy density at other non-target locations* because many wireless transfer systems incur higher energy on the transmitter-receiver path than at the target. In our study, we design and build a distributed beamforming based

WPT approach that can (1) deliver energy over tens of meters and (2) have the maximum energy level at the target location. Such an approach can potentially lead to safe and practical wireless charging solutions - by controlling the power level at the target within a safe range, we can ensure that the power level at other locations is also safe. Also, due to its distributed nature, our approach can efficiently transfer energy even when there are human subjects or other large obstacles in the space; while in a traditional beamforming based WPT system, having obstacles on the beam may significantly undermine the energy transfer efficiency.

Deliver power to tiny and battery-free IoT devices that are placed in extreme environments. Maintaining batteries are usually not feasible as these tiny IoT devices may be deployed in an inaccessible environment (*e.g.*, volcano or swamp) or injected into the human body. It is possible to power up in-body IoT devices using DAS. However, the major challenge is that the RF signals experience severe attenuation as they propagate in human tissues. Blindly amplifying the signal power is unfeasible due to the inherent health hazard. *e.g.*, skin burning. The state-of-the art system, IVN [8], combines multiple signal streams transmitted over different frequencies to boost the received power at the target location under unknown channel conditions. However, this algorithm inevitably overheats the other parts of human bodies as well, which may inherently violates FCC's regulation on RF exposure. In contrast, by leveraging the energy ball, we can increase the energy density level at the target location (*i.e.*, where the in-body IoT device stays) while avoiding overheating at other parts of the human body. However, there are new challenges in the context of distributed beamforming for implants. The implants usually run in extremely low power fashion, which prohibiting them undergo complex computing tasks. Also the RF signal experiences excessive path loss in the human tissue. Realizing distributed beamforming based on feedback can be a daunting task. Last but not least, the

implanted devices can work in a fully passive manner. It is a 'chicken or the egg' problem. A proper plan to bootstrap is required.

1.3 Road Map

In the first part, we show, when distributed transmitters align their phases at a common receiver, that several secrecy-supporting properties result. Further, secrecy is possible without requiring knowledge of the eavesdropper or the use of interference. By leveraging these properties, we present a new approach, referred as *Secret-Focus*, that builds a highly efficient secret communication channel on top of distributed phase alignment. We implemented a prototype *Secret-Focus* system that used amplitude-based modulation on top of phase alignment, to achieve secret communication between a coalition and an intended receiver. We presented an implementation using USRPs and experimental results that shows *Secret-Focus* can be built practically with a distributed set of transmitters employing phase alignment. Our detailed measurements demonstrate that Bob can achieve a very low BER, 3.1×10^{-6} when more than $160M$ bits are transmitted, while Eve's BER is between 30% – 60% across multiple measurement locations. In addition, we also show that Eve cannot eavesdrop even at extreme locations, such as in the close proximity of Bob, or one wavelength away from one of the transmitters antennas.

In the next part, we present a new WPT approach that transfers wireless energy to intended receivers by arranging a group of distributed transmitters around the receiver and coherently combining their phases at the receiver. This approach is a departure from existing beamforming based WPT approaches which have high energy on the energy beam path. The key innovation of our approach is that it can maximize the received power solely at the receiver, and have low received power at other locations across the space. Through detailed evaluation

using 21 USRP nodes across a $20 \times 20 m^2$ area, we show that the proposed approach can maximize the power level at the target receiver, can deliver a consistent amount of power to any point in the area, can charge a mobile receiver, and can continuously power a low-power IoT node at any point across the area.

Lastly, we propose a multi-antenna system that can continuously charge the medical implant at the near optimal beamforming power, even when the implant moves around inside the human body. But there are several challenges needed to be tackled down. RF signal generation is quite power hungry, which becomes especially challenging for medical implants that are deeply power constrained [9]. In practice, to minimize power consumption, the RF radio of a medical implant typically adopts a rather low power amplification coefficient [10]. Therefore, the resulting preamble signals are very weak, which are then made even worse by the fast decaying radiation efficiency of an in-body antenna. The antenna's radiation efficiency decays significantly due to its miniature size, i.e., 10 – 20 dB loss compared to the weak transmission signals [11, 12]. Furthermore, RF signals experience exponentially more attenuation in human tissues than in air, *e.g.*, 40 dB loss over just a few centimeters in muscles [13]. As a result, the received signal is usually well below the noise floor, hence the failure to provide accurate CSI estimation. We have to overcome the above challenges for a robust inbody wireless power delivery system.

Chapter 2

Secret-Focus: A Practical Physical Layer Secret Communication System by Perturbing Focused Phases in Distributed Beamforming

2.1 Introduction

Ensuring confidentiality of communication links is among the most fundamental objectives in developing communication systems. It is crucial for many applications to be able to distribute secure bit strings, such as higher-layer encryption keys, to wireless entities. Providing confidentiality is often a daunting task due to the broadcast nature of wireless links and therefore the ease of eavesdropping.

In addition to cryptographic mechanisms, many mechanisms that exploit a communication system's physical layer properties to protec secrecy have been proposed. These mechanisms usually aim to make the channel to the intended receiver much better than the channel to the eavesdropper. For example, wireless signal's propagation and fading properties have been exploited to increase capacity and enhance security in [14, 15, 16, 17]. Beamforming has been leveraged to increase the signal to noise ratio (SNR) at the intended receiver as well as to minimize the SNR for the eavesdropper using zero-forcing [18]. Artificial noise has been targeted at the eavesdropper to jam their reception [19]. Though these systems have demonstrated capabilities to communicate secretly, they have several drawbacks. Firstly, most of them assume that the eavesdropper's location is known, and there are only a small number (often just one) eavesdropper. Secondly, the practicality and efficient distribution of the secret in these proposed

systems is questionable. Thirdly, many systems have shadow areas where the anti-eavesdropping mechanism is less effective. Fourthly, some systems assume the eavesdroppers possess less knowledge than the receiver. Therefore, supporting confidentiality remains a significant challenge in wireless communication systems.

Recently, distributed communication systems that involve a distributed collection of transmitters have received attention in the community. For example, a cellular provider may employ multiple basestations that are connected by dedicated backhaul. At the other end, it could just be a group of transmitters who are willing to coordinate their transmissions to a common receiver [20, 21]. In such systems, referred as distributed beamforming [22], the transmitters can form a coalition and achieve constructive superpositioning of signals at the intended receiver by aligning the received signals' phases, with the receiver sending a small amount of feedback. In this study, we refer to this type of distributed systems as *distributed phase alignment* systems and leverage such a system to facilitate secret communication.

By examining how the transmitter signals coherently combine at the receiver, we show that phase alignment accomplishes highly efficient secret communication against eavesdroppers without knowing their location, nor introducing any additional signal/noise. Also, to engage in secret communication, a distributed phase alignment system only needs to introduce very minor modifications to their normal transmission procedure. Once the transmitters align their phases at the receiver, they may start to communicate secretly to the receiver, by periodically dithering its phase around the proper alignment phase during transmission. In this way, the system naturally achieves secret communication. Firstly, the secret recipient's SNR is largely increased by aligning the phases at the intended recipient. Slight dithering of the phases later on has negligible impact on the alignment, but can create high received signal strength (RSS) variation at other locations,

hindering anyone else from decoding the signal. Thirdly, it does not involve using interference for secrecy, which complicates system design, requires complex interference cancellation and decoding, and regulations suggest is unlikely to be allowed in practical systems. We refer to this highly efficient yet practical secret communication mechanism as *Secret-Focus*.

In this thesis, we show the effectiveness of *Secret-Focus* through both analysis and prototyping (using N210 USRPs). Our experimental results show that the intended recipient has bit error ratio (BER) as low as 3×10^{-6} while eavesdroppers have a much higher BER ranging from 31% to 38%, from measuring different eavesdropper locations for a total of $164.79M$ bits. In addition to the main test area, we have also examined extreme eavesdropper locations to further demonstrate it has little shadow area. We show that when the eavesdropper antenna is side by side(approx. 1cm) with the receiver antenna, the resulting BER is 12.45%; when the eavesdropper antenna is one wavelength (approx. 30cm) away from one of the transmitter antennas, the BER is 27%.

To summarize, we make the following contributions in this work. Going beyond beamforming and jamming based techniques, we propose a new phase combining and dithering based secret communication mechanism, prove its salient properties, and build a prototype system to validate these properties. Without interfering with the underlying communication or hurting the data rate, our mechanism can be easily combined with any amplitude-based modulation schemes such as PAM or QAM. More importantly, our approach works without requiring the system to know the eavesdropper's location or injecting noise before hand, and can disable eavesdroppers even at tricky locations such as in close proximity to the intended receiver or in close proximity (one wavelength) to a transmitter antenna.

2.2 Background on Secret Communication Systems

As a starting point, we provide a background of physical layer secret communication systems. In a secret communication system, a sender (Alice) wishes to reliably deliver a secret message S to an intended receiver (Bob) in the presence of an eavesdropper (Eve). The secret message S is then subsequently encoded into a signal X that is transmitted by Alice, Bob receives a signal Y while Eve receives a signal Z . The objective in information-theoretic secrecy is to ensure that Eve learns as little information as possible about the original secret message S . The past decade has seen the physical layer community makes significant contributions in providing secrecy for wireless channels.

Physical Layer Secret Communication for Wireless Channel: Several mechanisms have been discussed for achieving secrecy communication over the wireless channel. For example, the properties of wireless signal propagation and fading have been exploited for improving secrecy [23]. Also, the broadcast nature of the wireless channel allows one to introduce interference to hinder eavesdropping [24, 25, 26].

Physical Layer Secret Communication for Beamforming Systems: A number of secret communication mechanisms have been discussed for beamforming systems, such as those in [27, 28, 2]. With beamforming, Alice can leverage the directionality of the beam pattern to gain a better spatial diversity and ensure Bob's SNR is significantly higher than Eve's SNR at most locations. Moreover, by adopting zero-forcing [18], Alice can perform beam-nulling at Eve's location to further decrease their SNR. Further, Eve can also be jammed by the system intentionally sending artificial noise towards its direction [19], as illustrated in Fig. 2.1(a).

However, beamforming-based schemes have drawbacks and are quite different in effect than *Secret-Focus*. Firstly, in order to perform beam-nulling or jamming,

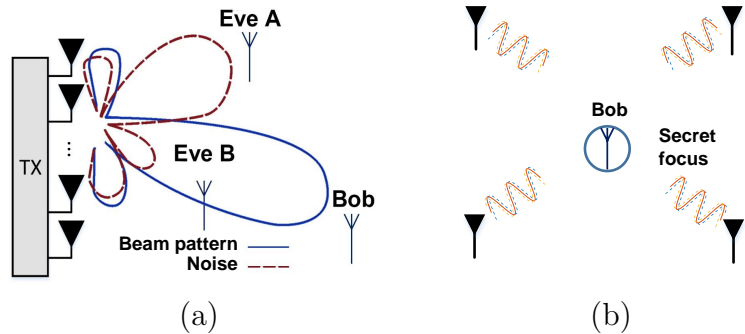


Figure 2.1: (a) shows a beamforming based secure communication system, in which artificial noise is used to jam Eve. (b) illustrates *Secret-Focus* in which distributed transmitters first align their phase at Bob and then perturb their phases around the alignment phase to focus the secret message at Bob.

a common assumption is that Alice knows Eve’s locations. In many scenarios, it is impossible to predict Eve’s location. Secondly, some of them may not need to know Eve’s location [27], introducing artificial noise can be costly, which may also impair Alice’s transmission towards Bob. Thirdly, such a design implies that any eavesdropper in the path of the main side lobe may be empowered to decode the signal. Consequently, linear-array style beamforming is not ideally suited for secrecy communication. Instead, as illustrated in Fig. 2.1(b), it is desirable to leverage a set of distributed transmitters to collectively communicate to the target receiver. Those are what motivate the design of *Secret-Focus*. By adopting our methods, we achieve highly secure communication without knowing Eve’s location or sending any additional noise.

2.3 Perturbing Aligned Phases for Secret Communication

Secret-Focus involves a collection of transmitters that are distributed geographically, and who transmit secret bit strings to the intended recipient in a coordinated fashion: first reaching a steady state by aligning their phases at the recipient and then dithering their phases around the steady state phase (which we refer to as Φ_{alg}) while communicating bit strings. Specifically, each transmitter adjusts the phase of their communication signal and, with the help of a small amount of

feedback from the recipient (Bob), without assuming any knowledge about Eve, they achieve significantly improved signal quality at the recipient compared to that witnessed by an unintended receiver (Eve).

There are many approaches for transmitters to align their phases, but the specific details for how this alignment occurs has little bearing on how secrecy is achieved. Later, in Section 2.4.1, we explain the phase alignment procedure we use to prototype Secret-Focus, but here we focus on examining how phase alignment creates Alice-Bob advantage relative to Alice-Eve, and thereby supports secrecy for Alice-Bob.

To do this, we assume all transmitters know the secret message to transmit. Then, motivated by [23, 29], which showed that discrete signaling can often outperform Gaussian signaling for secrecy, Secret-Focus starts with a basic pulse amplitude modulation scheme in which each transmitter will transmit a suitably phase-aligned *high* signal to transmit a 1 bit, and a phase-aligned *low* signal to convey a 0 bit (see Fig. 2.3(a)). These will constructively add at Bob to produce a received signal Y , while an eavesdropper Eve will witness a signal Z . With each transmitter slightly dithering phases after alignment, each mode of Y will have a mean corresponding to how well the phase alignment combines constructively at Bob, and a variance from noise. Hence, signal values Y can be modeled by a mixed (complex) Gaussian with two modes, where one mode corresponds to the 1 bit and the other corresponds to 0 bit (see Fig. 2.3(b)), and similarly for Z .

We may calculate the secrecy rate $I(X; Y) - I(X; Z)$, which captures the achievable rate at which Alice-Bob could secretly communicate in the presence of Eve, with the high/low discrete signaling. Using $I(X; Y) = H(Y) - H(Y|X)$, and the differential entropy $H(Y)$ for a mixed Gaussian[30], we define the intermediate terms, the ratio of the means to variances, as the *secret communication ratio* (*SCR*) $\alpha = \frac{\mu}{\sigma}$ for each recipient (be it Bob or Eve), where μ and σ are the average signal value and standard deviations, illustrated in Fig. 2.3(b). Noting that the

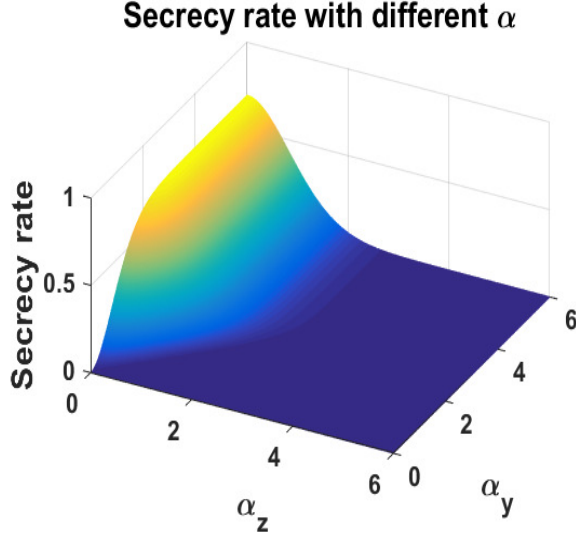


Figure 2.2: Theoretical secrecy rate as a function of α_y and α_z . Communication is secret when we have $\alpha_y > \alpha_z$, and while keeping α_z small enough.

$H(Y|X)$ collapses to $H(Y|X) = \frac{1}{2} \ln(2\pi e \sigma_y^2)$, $I(X;Y)$ becomes $I(X;Y) = \alpha_y^2 - I_y$, where:

$$I_y = \frac{2}{\sqrt{2\pi}\alpha_y} e^{-\alpha_y^2/2} \int_0^\infty e^{-x^2/2\alpha_y^2} \cosh(x) \ln(\cosh(x)) dx. \quad (2.1)$$

Thus, the secrecy rate for our choice of X is $(I(X;Y) - I(X;Z))^+ = (\alpha_y^2 - \alpha_z^2 + I_z - I_y)^+$. We illustrate the secrecy rate in Fig. 2.2.

Then in order to differentiate Alice-Bob from Alice-Eve, a positive and higher secrecy rate is desirable, hence we design Secret-Focus such that $\alpha_y > \alpha_z$, and a higher α_y and lower α_z yields a better secrecy (as illustrated in Fig. 2.2). Specifically, since $\alpha = \frac{\mu}{\sigma}$, our design goal is to *achieve a higher SNR and lower signal variation at Bob while having a lower SNR and higher signal variation at Eve*.

Secret-Focus achieves this objective through two complementary mechanisms: first, significantly improve μ_y using multiple transmitters focusing their efforts; and, second, relatively increase σ_z at Eve through intentionally introducing additional phase perturbations following phase alignment, which has a minimal effect at Bob. In the rest of this section we discuss these two mechanisms in detail, and also present a discussion in the end.

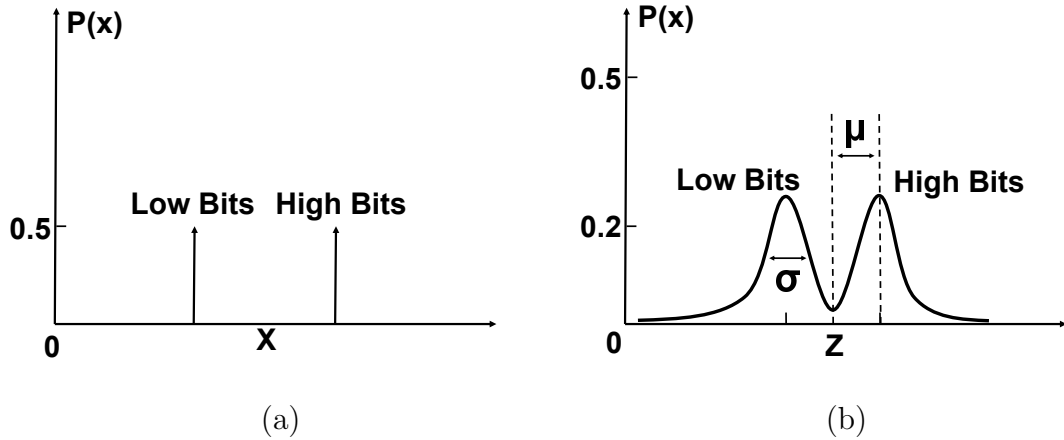


Figure 2.3: (a) Alice generates low bits and high bits following amplitude based modulation. (b) shows a typical distribution of bits received by Bob. Received bits follow a mixed (complex) Gaussian distribution.

2.3.1 Mechanism 1: Combining Phases Increases μ_y

The first key idea of our design is to place transmitters around the target receiver, as illustrated in Fig. 2.1(b), to achieve an effect similar to how Fresnel zone plates [31] focus light at a focal point. In optical systems, Fresnel zone plates act as a phase shifter for the passing light, similar to how our transmitters alter the phases of emitted radio waves.

To understand the radio focusing effects, suppose we place transmitters on a circle with radius R in free space around the receiver, and they coherently combine their phases at the center. Assuming, without loss of generality, that they align their phases at 0 degrees at the center, then the normalized magnitude of the signal values (RSS) is given by:

$$Y_{target} = \left| \frac{R}{N} \sum_{i=1}^N \frac{1}{R} e^{j0} \right| = 1. \quad (2.2)$$

As shown in Fig 2.4, suppose we want to measure the normalized RSS at an Eavesdropper's location at a distance d to the target receiver. For an arbitrary transmitter and with the free space model, and with the free space model, the

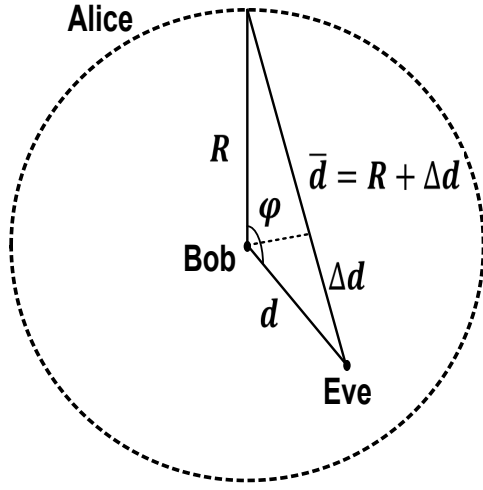


Figure 2.4: The geometric relationship between Alice, Bob and Eve, which is used in (2.3) and (2.4) when calculating the normalized RSS at Eve's location $Y(d)$.

phase difference between the focus location and the measurement location is:

$$\Delta\phi = 2\pi \frac{\sqrt{R^2 + d^2 - 2Rd \cos \varphi} - R}{\lambda}. \quad (2.3)$$

As we approach an infinite amount of transmitters around the circle, we can write the normalized RSS at the measurement location as:

$$\begin{aligned} Y(d) &= \left| \lim_{N \rightarrow \infty} \frac{R}{N} \sum_{i=1}^N \frac{1}{\bar{d}} e^{j2\pi \frac{\sqrt{R^2+d^2-2Rd \cos \varphi_i}-R}{\lambda}} \right|, \varphi_i \in [0, 2\pi] \\ &= \frac{R}{2\pi} \left| \int_0^{2\pi} \frac{e^{j2\pi \frac{\sqrt{R^2+d^2-2Rd \cos \varphi}-R}{\lambda}}}{\sqrt{R^2 + d^2 - 2Rd \cos \varphi}} d\varphi \right|. \end{aligned} \quad (2.4)$$

Fig. 2.5 compares the result from analytic RSS expression $Y(d)$ and the simulation result, for a RF signal being emitted with frequency 3GHz. In the simulation, we placed 100 transmitters on a circle, with the focus location at the center. Note that the results are identical, and therefore verify our analytical derivation. Using our analytical result, for an asymptotically large number of transmitters, one can verify that the 3dB-down distance from the receiver is $d_{3dB} \approx 0.22\lambda$. For a smaller number of transmitters, d_{3dB} would still be proportional to the radio wavelength λ as long as transmitters are placed around the target receiver.

Further, we can see in Fig. 2.6(a) that the results for the normalized RSS expression $Y(d)$ has a spatial pattern similar to the magnitude of a sinc function,

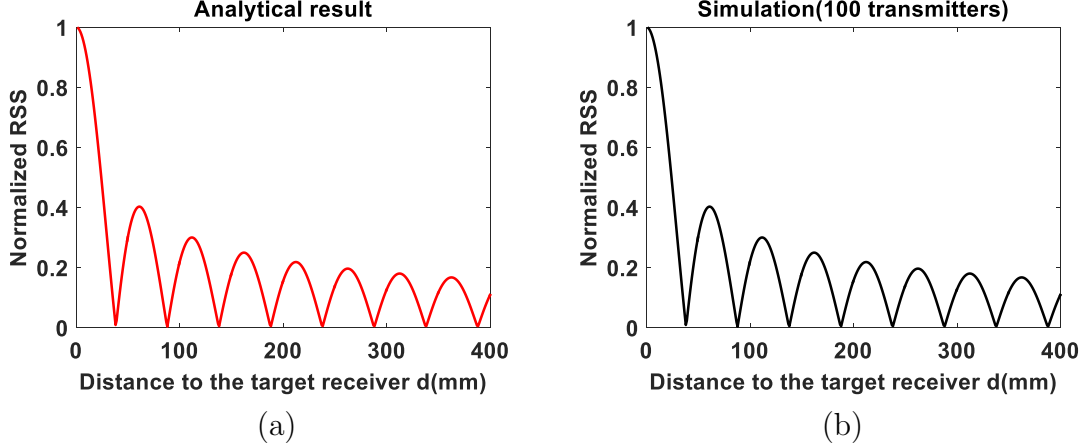


Figure 2.5: (a) Analytic results for the normalized RSS function $Y(d)$ in (2.4), where RSS decreases with d . (b) Numerical results of RSS versus d , where 100 transmitters were placed in a circle around the target. The numerical results match analytical results exactly.

with the maximum at the target receiver location. This location corresponds to where transmitter signals coherently combine (phases aligned) and, intuitively, there is no other location with such high energy.

Mathematically, the normalized RSS function $Y(d)$ gives us what we desire for Secret-Focus: we only have one maximum energy location spatially, and low energy at other locations. Now we take a look at the normalized RSS expression $Y(d)$, due to the symmetry of transmitters placement respect to the focus location, we can ignore the path loss term $\frac{1}{d}$ in our analysis, giving:

$$\begin{aligned} Y(d) &= \frac{1}{2\pi} \left| \int_0^{2\pi} e^{j2\pi \frac{\sqrt{R^2+d^2-2Rd\cos\varphi}-R}{\lambda}} d\varphi \right|, \\ &= \left| \lim_{N \rightarrow \infty} \frac{1}{N} \sum_{i=1}^N e^{j2\pi \frac{\sqrt{R^2+d^2-2Rd\cos\varphi_i}-R}{\lambda}} \right|, \varphi_i \in [0, 2\pi]. \end{aligned} \quad (2.5)$$

While performing above summation, if d is not zero, as φ_i varies in $[0, 2\pi]$, $\sqrt{R^2 + d^2 - 2Rd \cos \varphi_i}$ will vary, so that the phase term $2\pi \frac{\sqrt{R^2+d^2-2Rd\cos\varphi_i}-R}{\lambda}$ will not be the same for different i in the summation. We know that the maximum of this summation is achieved when the phase of each term aligns, and as a result we have:

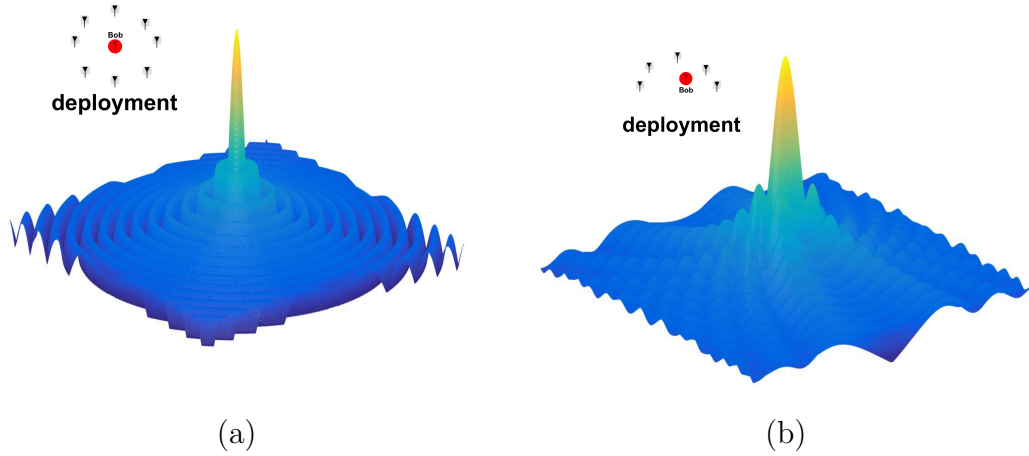


Figure 2.6: (a) Simulation results of RSS distribution in a $1m$ by $1m$ area around Bob. It is clear that the energy is sharply focused around the target location. In (b), we decrease the number of transmitters to 30, and place them on a half circle. Note the target receiver is also not placed at the center. As can be seen, even though the energy focus is wider, the peak is still very pronounced compared to other locations.

$$\begin{aligned} Y(d) &= \left| \lim_{N \rightarrow \infty} \frac{1}{N} \sum_{i=1}^N e^{j2\pi \frac{\sqrt{R^2+d^2-2Rd \cos \varphi_i}-R}{\lambda}} \right|, \varphi_i \in [0, 2\pi] \\ &\leq \left| \lim_{N \rightarrow \infty} \frac{1}{N} \sum_{i=1}^N e^{j2\pi \frac{\sqrt{d^2-d}}{\lambda}} \right| = Y(0). \end{aligned} \quad (2.6)$$

As d varies from 0 to $+\infty$, according to the above analysis, the only way to align the phase term is to set $d = 0$. Hence, $Y(0)$ is the unique global maximum. In other words, as transmitters aligning their phases at a certain location, the RSS at other locations would be less than the RSS at that location.

In real world implementations, a large number of transmitters are usually prohibitive. However, as long as we have sufficient transmitters placed around the receiver (regardless of whether they are placed in a regular or irregular pattern), we can still achieve a focus on the target receiver. Fig. 2.6(b) shows another result when only 30 transmitters are placed on a half circle around the target receiver (target receiver is not placed at center). Further, in practice, these results extend straight-forward to three-dimensional deployment scenarios.

2.3.2 Mechanism 2: Dithering Phase Hurts Eve

The second key idea of our design is to have the transmitters, once phase aligned, repeatedly perturb their phases around the alignment phase. In doing so, the signal values measured by Eve fluctuate significantly, hindering Eve's ability to decode the received signal. At the same time, as we will show, such perturbation does not harm Bob's decoding ability. Below we will prove the effectiveness of this mechanism.

Bob's RSS Remains Stable Even with Perturbation: First, note that the received signal in the free space model at an arbitrary location is:

$$\vec{Y}(\phi_1, \phi_2, \dots, \phi_N) = \sum_i^N A_i e^{j\phi_i}. \quad (2.7)$$

where A_i and ϕ_i denote the amplitude and phase of the i^{th} signal source received at the location, and N is the number of signal sources (transmitters). Next, the real and imaginary part of the received signal are:

$$\begin{aligned} \vec{Y}_{real} &= A_1 + A_2 \cos \theta_1 + A_3 \cos \theta_2 + \dots + A_n \cos \theta_{N-1}, \\ \vec{Y}_{img} &= A_2 \sin \theta_1 + A_3 \sin \theta_2 + \dots + A_n \sin \theta_{N-1}. \end{aligned} \quad (2.8)$$

in which θ_i is the phase difference between signal $i+1$ and the first signal (i.e., with ϕ_1 as the reference phase). Thus, the squared amplitude of the received signal is $Y^2(\theta_1, \theta_2, \dots, \theta_{N-1}) = \vec{Y}_{real}^2 + \vec{Y}_{img}^2$. The derivative of Y^2 with respect to θ_{i-1} is given by:

$$\begin{aligned} \frac{\partial Y^2}{\partial \theta_{i-1}} &= 2A_{i+1}(-A_1 \sin \theta_{i-1} + A_2 \sin(\theta_1 - \theta_{i-1}) + \\ &\quad A_3 \sin(\theta_2 - \theta_{i-1}) + \dots + A_N \sin(\theta_{N-2} - \theta_{i-1})). \end{aligned} \quad (2.9)$$

in which $i \in [2, N]$. Considering $\theta_1, \theta_2, \dots, \theta_{N-1}$ are independent, the impact of small phase perturbations upon $Y^2(\theta_1, \theta_2, \dots, \theta_{N-1})$, is the sum of the partial derivatives:

$$\begin{aligned} G(\theta_1, \theta_2, \dots, \theta_{N-1}) &= \sum_i^{N-1} \frac{\partial Y^2}{\partial \theta_i}, \\ &= -2A_1(A_2 \sin \theta_1 + A_3 \sin \theta_2 + \dots + A_N \sin \theta_{N-1}). \end{aligned} \quad (2.10)$$

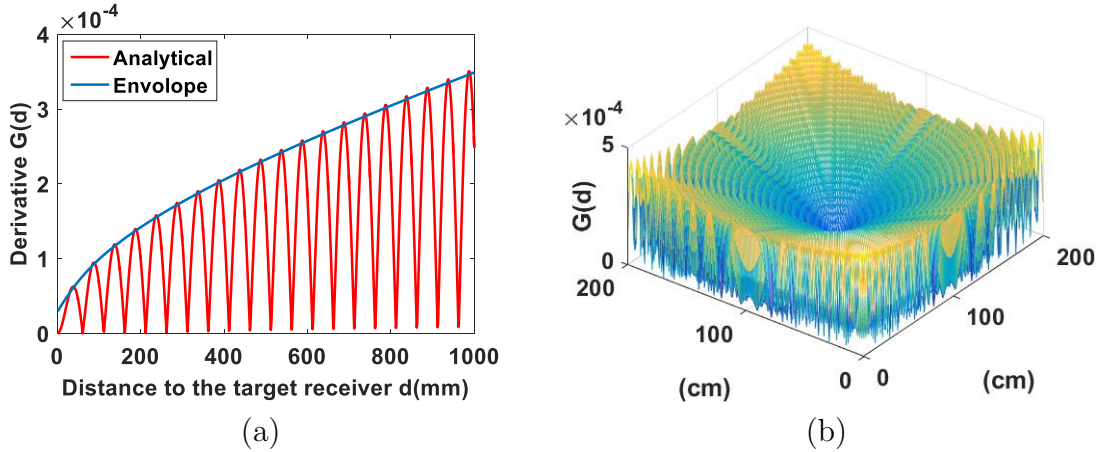


Figure 2.7: (a) The analytical results for $G(d)$ in (2.11). The envelop of $G(d)$, marked in blue, shows that Eve's RSS variation increases with d . (b) The distribution of $G(d)$ in a $2m \times 2m$ area around Bob shows the same trend. We observe the lowest G value at Bob's location.

Here, $\theta_1 = \theta_2 = \dots = \theta_{N-1} \approx 0$ since the signal sources are properly phase aligned, giving $G(\theta_1, \theta_2, \dots, \theta_{N-1}) \approx 0$ at the target receiver. In particular, the target location has the lowest variability with respect to phases $\theta_1, \theta_2, \dots, \theta_{N-1}$ because the slope $G = 0$. Hence, we have shown that *Bob's RSS values will NOT fluctuate much due to small phase perturbations we choose to introduce.*

Eve’s RSS Becomes Unstable and Has Large Variation: Next, we examine the impact that small fluctuations around the phase alignment optimum would have upon Eve. Assume a large number of transmitters on a circle $N \rightarrow \infty$, and the target receiver at the center. Similar to Equation 2.4, we calculate $G()$ at a distance d from Bob’s location, which we refer to as $G(d)$. By taking the limit, we get the integral:

$$G(d) = -2 \int_0^{2\pi} \frac{\sin(2\pi \frac{\sqrt{R^2+d^2-2Rd\cos\varphi}-R}{\lambda})}{(R-d)\sqrt{R^2+d^2-2Rd\cos\varphi}} d\varphi. \quad (2.11)$$

In order to understand the implication of $G(d)$ in our design, we show the $G(d)$ distribution in Fig. 2.7 ($R = 10m$ and $\lambda = 0.1m$). From the results, we observe that if we make a small change in phases around the optimal value for Alice-Bob, then since Eve’s $G(d)$ is large, her signal variation will be large, and this variation increases with d (as shown by the envelop curve in Fig. 2.7(a)). Here, an

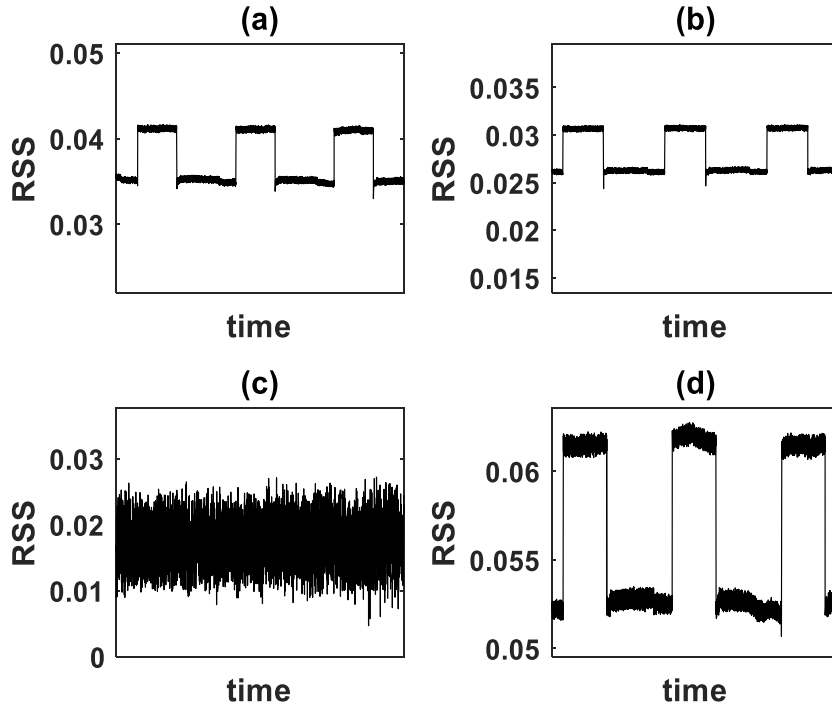


Figure 2.8: (a) Raw RSS at Eve for a broadcast channel (neither mechanism employed), (b) raw RSS at Eve for a NO-Perturb system (only mechanism 1 employed), (c) raw RSS at Eve for *Secret-Focus* (both mechanisms employed), and (d) raw RSS at Bob for *Secret-Focus*. In this example, only *Secret-Focus* is able to hinder Eve from decoding received signal and provide secret communication to Bob.

interesting observation is that, in some cases, Eve’s $G(d)$ values actually do reach zero. However, we note that at those points, a tiny change in the distance/phase will lead to substantial changes in $G(d)$. As a result, even if Eve momentarily has $G(d) = 0$, frequent dithering of the phase will lead to a new state with large $G(d)$. Overall, Eve’s RSS variation is significantly higher than Bob’s, which as we will show later leads to an intolerably high decoding error.

2.3.3 Effectiveness of the Two Mechanisms

Fig. 2.8 shows: (a) the raw RSS at Eve when transmitters are completely distributed and do not coordinate among themselves (thus a normal broadcast channel in which neither mechanism is employed), (b) the raw RSS at Eve when

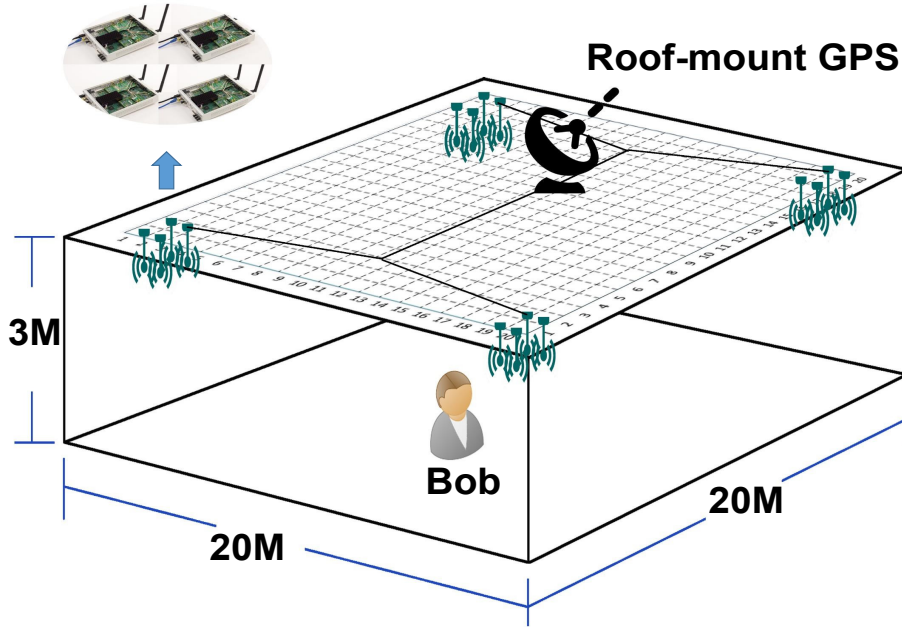


Figure 2.9: The *Secret-Focus* prototype consists of 16 transmitter USRPs. The deployment area of our prototype is $20 \times 20 \times 3 \text{ m}^3$.

transmitters perform phase combining, but keeping the phase at Φ_{align} during communication without perturbing the phase (which we refer to as *NO-Perturb* in which only mechanism 1 is employed), (c) the Raw RSS at Eve in *Secret-Focus* that employs both mechanisms, and (d) the raw RSS at Bob in *Secret-Focus*.

We observe that for the broadcast channel, both Eve and Bob receive the same RSS time series (with slightly different amplitude), and hence no secret between Alice and Bob. We have the similar observation in the NO-Perturb system which also fails to protect secrecy between Alice and Bob. However, applying both mechanism, the signal Eve receives in *Secret-Focus* fluctuates greatly over time, hiding the secret from Eve.

Having explained how *Secret-Focus* achieves secrecy, we next build a prototype system in Section 2.4 and evaluate its effectiveness in Section 2.5.

2.4 Putting Together a *Secret-Focus* Communication System

We have proved that having distributed transmitters align their phases and then employ slight dithering (around the proper alignment phase Φ_{algn}) can achieve a positive secrecy rate as it leads to higher and more stable RSS values at the intended receiver, but lower and less stable RSS values at other locations. These properties can be readily harnessed to facilitate secret communication through amplitude-based modulation schemes, such as on off key (OOK) communication, pulse amplitude modulation (PAM), or quadrature amplitude modulation (QAM). In this section, we discuss how we can design a practical *Secret-Focus* system and present our effort in building a *Secret-Focus* prototype using USRP N210s. Our objective in this thesis is to demonstrate that distributed phase alignment among a group of transmitters can achieve secret communication at the target location using the N210s.

Our prototype consists of 16 transmitters mounted on a ceiling, at four corners of a $20 \times 20 \text{ m}^2$ area. We used WBX RF daughter boards on the N210s, and our working frequencies are 915 and 964 MHz in this study. There is no communication back-channel between the transmitters, so they are completely distributed in nature. We synchronized the transmitter clocks through a roof-mount GPS. Fig. 2.9 shows a typical prototype setup, with 4 N210s at each of the four corners (these four USRPs are 1 meter apart from each other). The receiver can be *anywhere* in the deployment area.

Fig. 2.10 shows how a *Secret-Focus* system works. It goes through two main stages: the distributed phase alignment stage and the secret communication stage. We next discuss the design and implementation of these two stages.

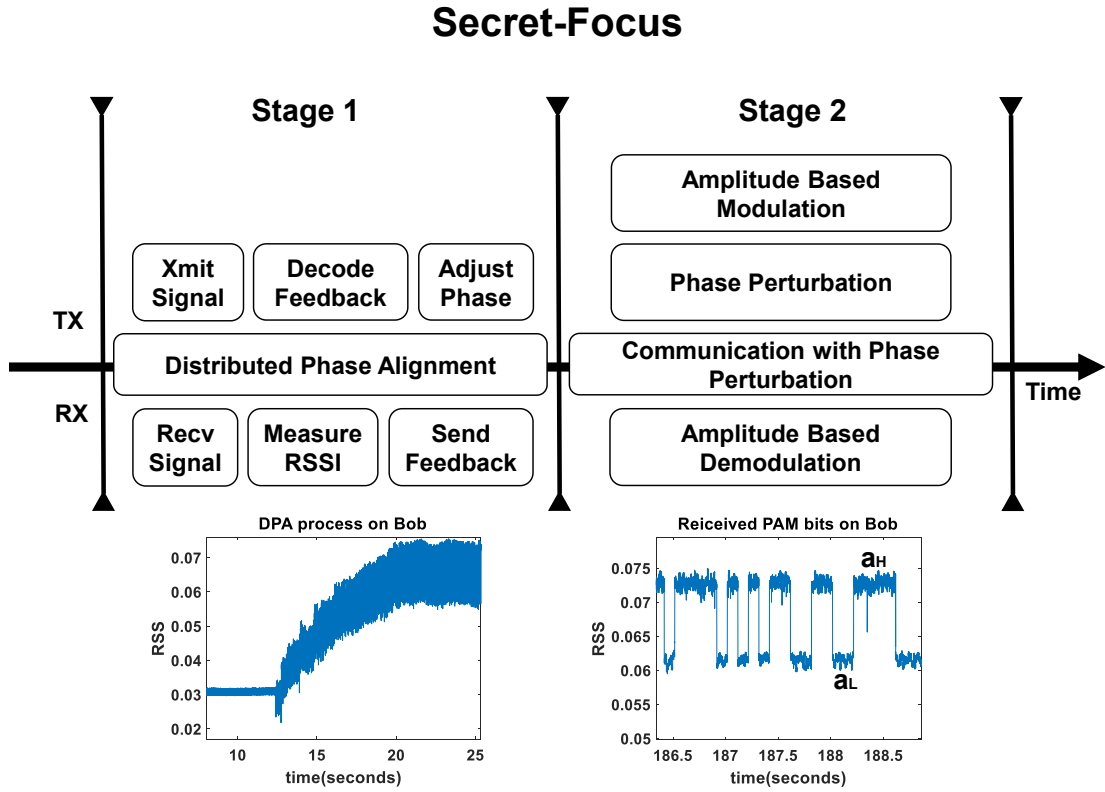


Figure 2.10: *Secret-Focus* consists of two main stages: distributed phase alignment, and secret communication with phase perturbation.

2.4.1 Trial-and-Error Distributed Phase Alignment

We chose to adopt a simple trial-and-error approach proposed in [22]. Assuming all nodes share the same clock, we partition the time into rounds of equal duration. Within each round, every transmitter sends a signal to the receiver at a randomly adjusted phase, with the phase randomly picked within $\pm\Phi^\circ$ of the previous phase value. At the end of each round, the receiver sends a small feedback message to indicate whether the new phase combination gives higher energy than before. If so, each transmitter holds this new phase value; otherwise, it goes back to its previous value. The phase adjustment is defined as:

$$\theta_i(n+1) = \begin{cases} \theta_i(n) + \delta_i(n), & \text{if } Y[n] > \max_{k < n} Y[k], \\ \theta_i(n), & \text{otherwise.} \end{cases} \quad (2.12)$$

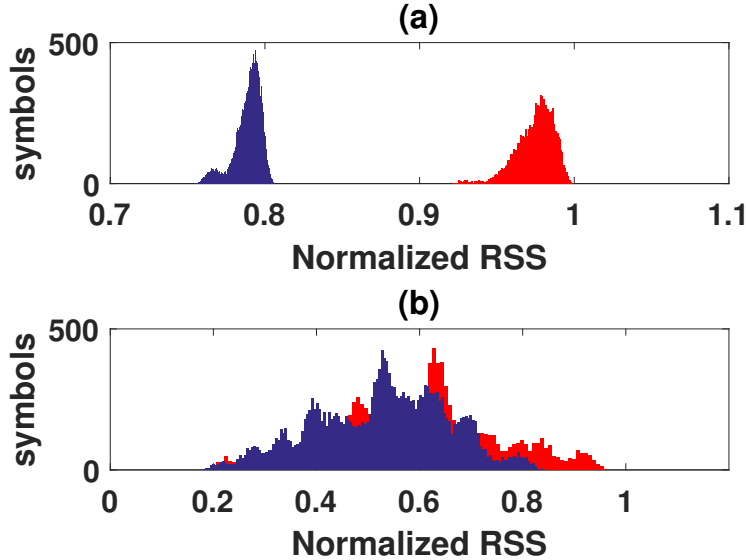


Figure 2.11: (a) Histogram of Bob’s RSS values, where high bit symbols and low bit symbols are clearly separated. (b) Histogram of Eve’s RSS values, where high bit symbols and low bit symbols are largely mixed.

where $\theta_i(n)$ denotes transmitter i ’s phase in round n , and we have $-\Phi \leq \delta_i(n) \leq \Phi$.

Though simple, we find that this approach effective in focusing transmitting signals and aligning their phases to Φ_{algn} . In implementing this algorithm, we write multiple out-of-tree GNU radio modules (GNU radio version 3.7.6.1.) and adopt a width-based modulation method to encode/decode the receiver feedback beacons. We fix the feedback rate at 25 Hz, which is also the transmitter phase adjustment rate. Received signal at Bob during an example phase alignment is included in Fig. 2.10.

2.4.2 Amplitude Modulation (AM) Based Secret Communication

When the transmitter phases are properly aligned at Φ_{algn} , the receiving USRP (Bob) broadcasts a pre-defined constant signal in 964 MHz to tell the transmitters to start communication. This explicit signaling ensures that all transmitters and

receivers enter the communication stage at the same time. In the communication stage, the transmitters (Alice) focus on two tasks: amplitude based modulation and frequent phase perturbation. In our prototype, we chose to use one-bit pulse amplitude modulation (PAM) for its simplicity, in which each symbol's amplitude is modulated as $\bar{A} = [a_L, a_H]$. Here, the amplitude of high bits and low bits, a_H and a_L , are important system parameters. We evaluate their impact and present the results in Section 2.5.3.

Phase perturbation in the communication phase ensures the RSS values at any non-target location have much greater variation than those at the target location, while ensuring all transmitter phases are still aligned at the target location. Specifically, each transmitter perturbs its phase around Φ_{algn} at a certain rate: in each perturbation interval, it randomly picks a value within $\pm\phi$ and adds that value to Φ_{algn} . In the evaluation, we have studied the impact of ϕ and present the results in Section 2.5.3. In addition, the perturbation rate is also an important parameter. Faster perturbation can handle more capable eavesdroppers. In our prototype, we set the perturbation rate as 100Hz.

At the communication stage, the receiver focuses on measuring the received RSS and decoding each bit accordingly. We assume the receiver (both Bob and Eve) knows the symbol duration t_{sb} . We apply a window based demodulation scheme. Specifically, after receiving the header, for each incoming payload bit, we measure the RSS during its symbol period and compare it against the average RSS within a pre-set window duration. If the current bit RSS is higher than the recent window average, the bit is decoded as 1; otherwise, it is a 0. In this thesis, we assume that Eve and Bob both have the knowledge of t_{sb} and header length, but in reality we note that Eve often is not equipped with such knowledge.

2.4.3 An Example Scenario

To illustrate the point, let us look at a typical secret communication scenario. In the example setting, we have 16 USRP N210 transmitters (shown in Fig. 2.9), in which Bob is at the red dot in Fig. 2.12 and Eve is at the E2 location in Fig. 2.12. In this example, the transmitters send 1200 bits to Bob, with 80 consecutive low bits as the header, and the rest as the payload (consisting of randomly generated 1s and 0s). We have $a_H = 1$ and $a_L = 0.8$.

For each transmitted bit, we measure the RSS, normalize the value to between 0 and 1, and place it in the corresponding RSS bins. We plot the histogram in Fig. 2.11. For each normalized RSS bin, we plot the number of bits whose RSS values fall in that bin. We further separate the number of high bits and low bits within each bin. The RSS values for Bob's high bits and low bits are clearly separated by a large margin, while the RSS values for Eve's high bits and low bits are largely overlapped with each other, hard to be separated.

Here, the decoding bit error ratio (BER) is the ratio between the number of incorrect bits and the total bits transmitted. Here Eve's BER is 42.1%, which is close to a completely random system with BER of 50%. At the same time, Bob correctly decodes all the bits. Hence, communication between transmitters and Bob is kept secret. We assume that Bob and Eve both have the knowledge of symbol duration, header length, and communication start time.

2.5 Prototype Evaluation

In this section, we report the measured results and show that *Secret-Focus* is indeed able to provide efficient secret communication between the transmitters and the receiver, regardless of eavesdropper's count and locations. Throughout our evaluation, we assume Bob and Eve have the same knowledge and capability.

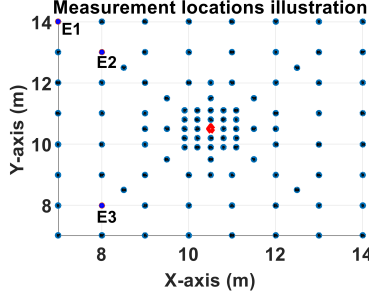


Figure 2.12: A $7 \times 7 \text{ m}^2$ test area. We placed Bob (red) in the center, and Eve at 100 possible locations (blue). Eve locations not uniformly distributed, but denser towards the center.

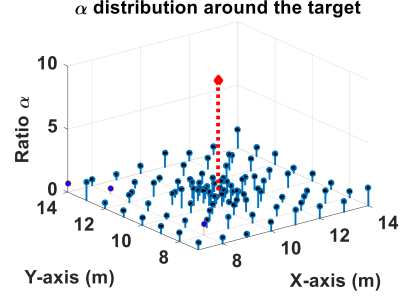


Figure 2.13: The measured average α_{Bob} is significantly higher than α_{Eve} at all 100 Eve locations. Thus, Bob can have secret conversation with Alice in the presence of Eve at these 100 locations.

2.5.1 *Secret-Focus* Makes Eavesdropping Impossible

The objective of the first set of experiments is to show that Eve cannot eavesdrop the communication regardless of the location. For this purpose, we use the $7 \times 7 \text{ m}^2$ square in the center of the deployment area as the test area (illustrated in Fig. 2.12). We place a USRP receiver (Bob) at the center of the test area (see the red dot in Fig. 2.12) and placed another USRP receiver (Eve) at 100 different locations in the test area (see the blue dots in Fig. 2.12). We measured more eavesdropper locations closer to the target receiver to investigate whether eavesdroppers near Bob are able to decode the communication. In these experiments, we used all of the transmitters $N = 16$, with $a_H = 0.7$, $a_L = 0.5$, and $\phi = 15^\circ$. At each location, we collected a total of 20,000 high bit symbols and 20,000 low bit symbols with symbol duration $t_{sb} = 20\text{ms}$.

Fig. 2.13 shows the measured average α_{Bob} and 100 different α_{Eve} values. We observe that α_{Bob} is clearly much higher than α_{Eve} . Specifically, we have $\alpha_{Bob} = 9.42$, $\alpha_{Eve}^{max} = 1.54$, and $\alpha_{Eve} < 1$ for 81 out of 100 locations.

Next, we compare *Secret-Focus* with a normal broadcast channel and a NO-Perturb system (in which transmitters do not perturb their phases once aligned).

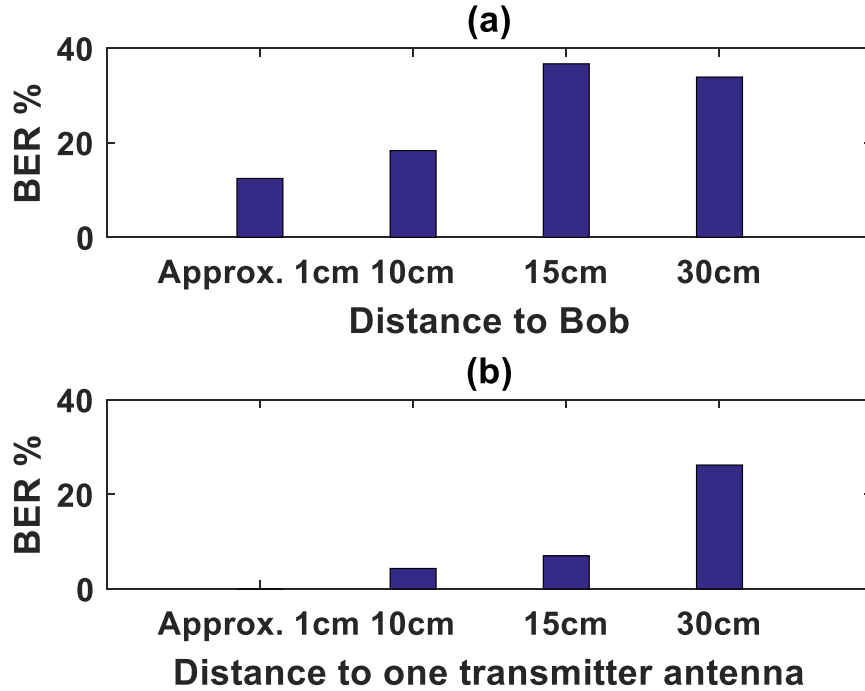


Figure 2.14: Extreme Eve locations outside of the test area. $BER = 12.45\%$ when she is side-by-side with Bob, and $BER = 7\%$ when she is 15cm (half a wavelength) away from one transmitter antenna.

Measuring the same 100 Eve locations, we plot the α_{Eve} distributions for the three systems in Fig. 2.15. Please recall, as shown in Fig. 2.2, a system with *better* secret communication has *lower* α_{Eve} values. The results show that *Secret-Focus* fares much better than the other two systems. In *Secret-Focus*, α_{Eve} values are within [0.12, 1.53], while [3.03, 5.98] for NO-Perturb, [4.01, 5.99] for Broadcast only.

Table 2.1: Average Decoding errors statistics for Bob and 3 Eves. Bob has extremely low BER while Eves' BER are over 30%.

	Bob	Eve ₁	Eve ₂	Eve ₃
Total Number of Bits Transmitted (bits)	164.79M			
Total Number of Bits Incorrectly Decoded (bits)	52.31K	52.29M	62.70M	60.36M
Estimated BER	3.1×10^{-6}	0.3173	0.3805	0.3663

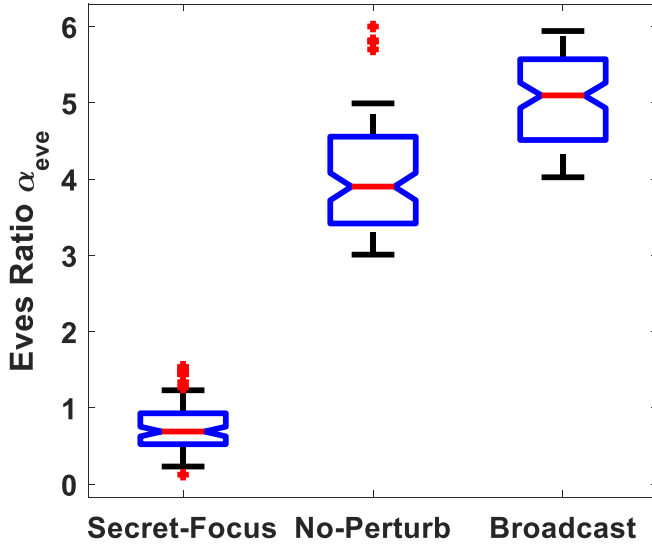


Figure 2.15: *Secret-Focus* has much lower α_{Eve} values than Broadcast and NO-Perturb. It provides better support for secret communication.

2.5.2 Low Decoding Error for Bob vs High Error Rate for Eves

The objective of the second set of experiments is to show that Bob can decode the secret bit strings with a very high success rate while Eve cannot. In order to estimate Bob’s BER that is very low, we send $164.79M$ bits from Alice to Bob in total. Considering the amount of time taken to make the measurements, we only measured the BER values at three Eve locations instead of the entire 100 locations in Fig. 2.12 (we marked these three locations as E1, E2, and E3 using bright blue color). In the experiments, we have $N = 16$, $a_H = 1$, $a_L = 0.8$, $t_{sb} = 0.05ms$, and $\phi = 15^\circ$.

Table 2.1 summarizes the BER values for Bob and three Eve locations. The results show that Bob has very low BER, $BER = 3.1 \times 10^{-6}$, while the BER at each Eve location is much higher, ranging from 31.73% to 38.05%. As a result, we conclude that *Secret-Focus* is highly effective in providing secret communication.

In addition, we have also tested several extreme Eve locations outside of the test area. First, we placed Eve very close to Bob, and present Eve’s BERs in

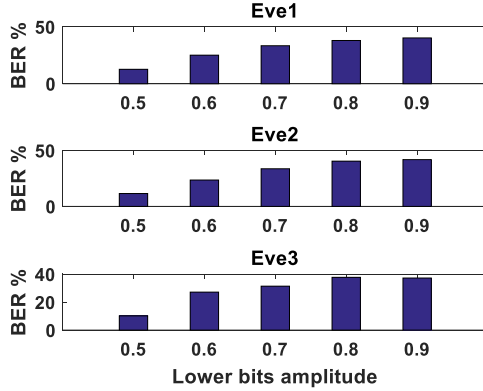
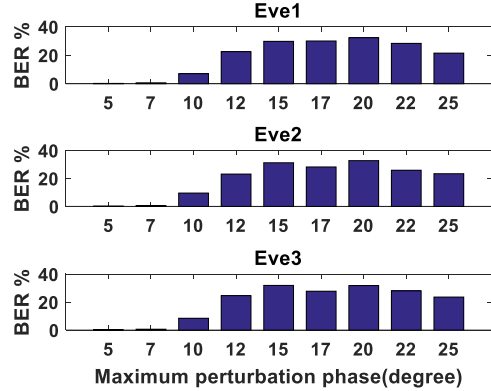
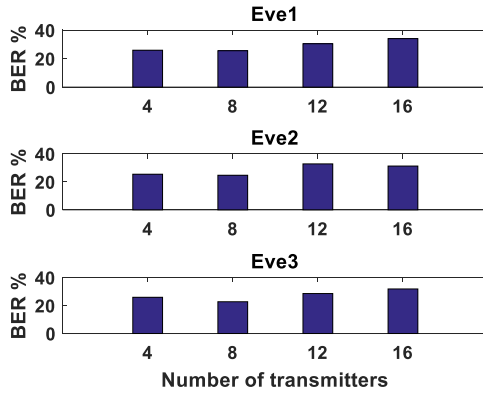
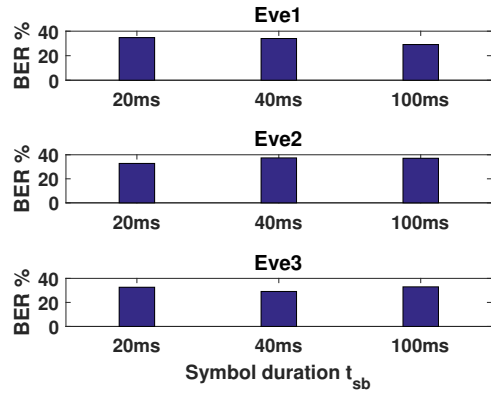
Figure 2.16: BER vs. a_L .Figure 2.17: BER vs. ϕ .Figure 2.18: BER vs. N .Figure 2.19: BER vs. t_{sb} .

Fig. 2.14(a). We found that even when Eve is in close proximity with Bob, her BER is 12.45% while Bob was able to decode all the bits sent in this example. Finally, we placed Eve very close to the transmission antenna of a transmitter. As shown in Fig. 2.14(b), we find that when Eve's antenna is close (approximately 1cm) to the transmitter antenna, it has comparable BER with Bob, but its BER increases to 27% when it is 30 cm away. These results further demonstrate that *Secret-Focus* is indeed very powerful in protecting secret communication.

2.5.3 Impact of Important System Parameters

The objective of the third set of experiments is to study the impact of several important system parameters.

Impact of a_L . Here, we use the same experimental setting as in last set of experiments, Bob in the center of the test area and three Eve locations. we set $N = 16$, $t_{sb} = 20ms$, $a_H = 1$, and $\phi = 15^\circ$, and vary the low bits amplitude in our amplitude modulation: $a_L = 0.5, 0.6, 0.7, 0.8$ and 0.9 . We calculate the three sets of BER values and show the results in Fig. 2.16. From the results, we observe that larger a_L values lead to a higher BER for Eves. This observation agrees with our previous theoretic analysis in Section 2.3.2. With a larger a_L value, the RSS values at Eve become even less stable, and hence higher BER. Under a more aggressive system parameter setting, $a_L = 0.95$, BER for Eve and Bob are 57.1% and 2.2×10^{-6} respectively.

Impact of ϕ . Here, we use the same experimental setting as in the last set of experiments, Bob in the center of the test area and three Eve locations. We set $N = 16$, $t_{sb} = 20ms$, $a_H = 1$, and $a_L = 0.8$, and vary the maximum perturbation angle $\phi = 5^\circ, 7^\circ, 10^\circ, 12^\circ, 15^\circ, 17^\circ, 20^\circ, 22^\circ$ and 25° . We calculate the three sets of BER values and show the results in Fig. 2.17. We observe the same trend for all three Eve locations. The results show that there is a sweet spot for ϕ , between 15° and 20° . This can be explained as follows. If ϕ is too large, it may make Bob's RSS values less stable. Meanwhile, if ϕ is too small, then it does not disturb Eve's RSS sufficiently.

Impact of N . Here, we use the same experimental setting with Bob in the center of the test area and three Eve locations. We set $\phi = 15^\circ$, $t_{sb} = 20ms$, $a_H = 1$, and $a_L = 0.8$, and vary the number of transmitters $N = 4, 8, 12$ and 16 (by having 1, 2, 3 and 4 USRP(s) at each corner, respectively). We present the three sets of BER values in Fig. 2.18. The results show that having more transmitters can

yield a higher BER for Eves. We note that having 4 transmitters is sufficient to prevent Eves from eavesdropping, indicating that our system is not only effective, but also very practical.

Impact of t_{sb} . Here, we use the same experimental setting with Bob in the center of the test area and three Eve locations. We set $\phi = 15^\circ$, $N = 16$, $a_H = 1$, and $a_L = 0.7$, and vary the symbol duration $t_{sb} = 20, 40$ and 100ms . We present the three sets of BER values in Fig. 2.19. The results show that choosing different symbol duration values has no significant bearing on Eve’s BER values.

2.6 Conclusion

In this work, we showed, when distributed transmitters align their phases at a common receiver, that several secrecy-supporting properties result. Further, secrecy is possible without requiring knowledge of the eavesdropper or the use of interference. By leveraging these properties, we present a new approach, referred as *Secret-Focus*, that builds a highly efficient secret communication channel on top of distributed phase alignment. We implemented a prototype *Secret-Focus* system that used amplitude-based modulation on top of phase alignment, to achieve secret communication between a coalition and an intended receiver. We presented an implementation using USRPs and experimental results that shows *Secret-Focus* can be built practically with a distributed set of transmitters employing phase alignment. Our detailed measurements demonstrate that Bob can achieve a very low BER, 3.1×10^{-6} when more than $160M$ bits are transmitted, while Eve’s BER is between 30% – 60% across multiple measurement locations. In addition, we also show that Eve cannot eavesdrop even at extreme locations, such as in the close proximity of Bob, or one wavelength away from one of the transmitters antennas.

Chapter 3

Energy-Ball: Wireless Power Transfer for Batteryless Internet of Things through Distributed Beamforming

3.1 Introduction

Ever since the invention of electricity, a world free of batteries and power cords has been the aspiration of many scientific investigations. Now, this vision is ever more appealing, with the proliferation of Internet of Things (IoT) systems, and at the same time ever more realistic thanks to recent advances in low-power embedded design and energy harvesting. As an example of low power IoT devices, in the year of 2016, Graule et al. [32] made a robotic drone that only needs 19mw to fly, and a couple of micro watts to remain perched on objects. Such extremely low power devices can be potentially powered through simple mechanisms such as ambient energy harvesting from lights, Wi-Fi router, TV and cellular signals [33, 34, 35]. While ambient energy harvesting has proven effective in the above examples, it becomes less effective in many other situations, especially when the required energy density exceeds what the environment offers. As such, near-field wireless charging techniques [36, 37, 38] have proven useful in delivering higher amount of energy. However near-field charging is either limited by its range or require large-scale facilities to achieve larger ranges.

As people endeavor to deliver higher amounts of energy over longer distances, they either choose to design wireless power transfer (WPT) systems using highly

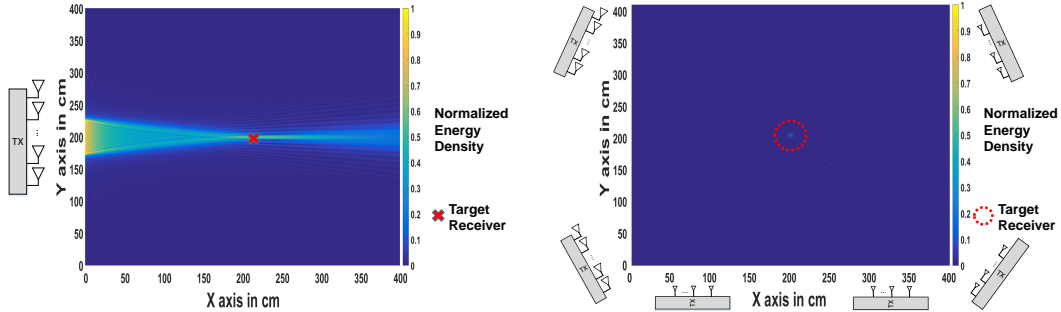


Figure 3.1: Energy density distribution for beamforming. Figure 3.2: Energy density distribution for *Energy-Ball*.

directional energy chargers or phased arrays that can steer the energy beam towards the target [39, 37, 40, 41]. However, such beamforming techniques have potential safety concerns as they often lead to high energy concentration along the beam, which poses risk to people or objects in those areas. Using simulations, we show the energy density distribution of an example beamforming system in Figure 3.1, where the energy density level along the beam is higher than that at the target receiver. As a result, a beamforming based WPT system requires extra measures to ensure (a) the energy level along the beam is low enough not to be harmful, and (b) the energy level at the target receiver is high enough to be useful.

In this thesis, we set out to design a new wireless power transfer system that can focus the energy around the target and minimize energy density in other areas. Towards this goal, we arrange our transmitters in a fully distributed fashion by surrounding them around the target receiver, as shown in Figure 3.2. A salient property of this arrangement is that, by aligning their phases at the receiver, the energy level at the target receiver is higher than the energy level at any other spot in the charging area. In fact, a small energy ball is formed around the receiver, hence the system name of *Energy-Ball*. Figure 3.2 shows the energy density distribution of *Energy-Ball* using simulation results. In designing *Energy-Ball*, we draw inspiration from the design of the surround sound system, in which

multiple speakers are arranged around the audience for better audio experiences.

When devising *Energy-Ball*, we have overcome the following main challenges:

- *Realizing Energy-Ball in a Realistic Setting.* Due to its completely distributed nature, it is hard to achieve phase alignment among the transmitters, especially when the amounts of transmitters increases. In a realistic setting, these transmitters do not have phase level synchronized clocks among them , nor do they communicate with each other. Furthermore, there often exist complex multipaths where *Energy-Ball* is deployed, which makes those algorithms that rely upon channel state information (CSI) less useful.

In this thesis, we carefully address this challenge by adopting a simple yet effective phase alignment technique that is closed-loop and that does not require any CSI information. In an iterative fashion, it uses the receiver's feedback to guide the transmitter's phase adjustments towards the optimal phases, with which the maximum received power is achieved at the receiver. We achieve phase level synchronization among the transmitters through a master-slave GPS architecture.

- *Continuously Charging Mobile Target.* *Energy-Ball* is designed to charge devices in an IoT system, where devices may be mobile, such as low power drones/robots or sensors that are attached to a mobile platform. In order to achieve continuous charging in this scenario, we have to figure out mechanisms to continuously re-align the phases of transmitters in a timely manner.

When the receiver moves, we need to look for a more direct way of keeping transmitter phases around their optimal values. Specifically, if the phase difference between the transmitter and the receiver was known, then the transmitter would directly adjust its phase according to the difference. Though

this information is not available to the transmitter, we propose to estimate it using the phase difference between the receiver and transmitter (which can be conveniently measured by the transmitter), considering that the phase differences in these two directions are highly correlated.

In summary, our work has the following contributions:

- We have devised a new wireless power transfer system, *Energy-Ball*, that can precisely focus energy on the receiver while having low energy density at other areas. To transfer the same amount of energy to a device, such a system leads to much less RF energy in the charging area than traditional beamforming systems. We believe *Energy-Ball* provides a viable and practical charging solution to rapidly growing IoT systems. We envision that *Energy-Ball* can be deployed to surround the target IoT nodes, such as in a smart factory, warehouse, or store, delivering energy to nodes one by one before they perform the required sensing/processing/networking functions, without the need to ever replace batteries for these nodes. Moreover, *Energy-Ball* can also be used to continuously power drones or robots that are used in agriculture, rescue, industrial assembly lines [42, 43, 44].
- We have built an *Energy-Ball* testbed using USRPs and validated its charging ability and resulting energy distribution using real-world experiments. Our results show that *Energy-Ball* can deliver over 0.6 mW RF power at any point in a $20 \times 20 \times 3 \text{ m}^3$ charging space, using 24 transmitters transmitting at 1.7W (which is the highest transmitting power allowed on our facility). Since *Energy-Ball* emits very low energy in the charging space, we will be able to deliver much higher energy by boosting the transmission power and/or increasing the transmitter number. Further, we show that a low-power tag [45] can be continuously powered by *Energy-Ball* at all the locations we have tried in the experiments.

- We have developed a fast phase adjustment algorithm that transmitters can adopt to continuously align their phases at a mobile receiver. For a mobile receiver whose speed is lower than 0.5 m/s, the received energy is on average around 80% of the energy received by a stationary receiver located at each point on the trajectory.

3.2 Related work and Motivation

3.2.1 Electromagnetic Radiation Based Energy Harvesting and Transferring

Many wireless charging systems transfer energy through electromagnetic radiation. We broadly group these systems into three categories: near field wireless charging, passive energy harvesting, and far field wireless energy transfer.

Near Field Wireless Charging: The near field is that part of the radiation field that is below the Fraunhofer distance $d_f = 2D^2/\lambda$ [46], where D is the source of the diffracting edge or antenna diameter, and λ is the wavelength. Transferring energy through coupling magnetic coils is a typical near-field energy delivery system, which is also the most commercially successful wireless charging method [47, 48], ranging from charging cell phones, tooth brushes, to cars and buses. Traditionally, this method had limited charging distance and required the device be placed in a certain position [49]. Fortunately, recent development has improved their performance. Adopting the idea of closed loop beamforming, MagMIMO [37] shapes a magnet flux into a steerable beam with multiple coils to charge iPhones. Due to the nature of closed loop beamforming, MagMIMO charges the iPhone regardless of its orientation and position. Meanwhile, in 2016, Disney research has created a $54m^3$ quasistatic cavity resonance room, which can deliver up to 1900 watts of power [36] in the whole room.

In summary, near field wireless charging systems can transfer a decent amount of energy, but it either suffers from very limited charging distances or it requires special large-scale facilities to achieve larger charging ranges. Neither case is suitable for our BF-IoT scenarios.

Passive Energy Harvesting: Passively harvesting is also called ambient harvesting. It is proposed for charging sensors, medical implants and many other extremely low power sensors [50, 51, 52]. For example, Ambient Backscatter [35] is a prototype end-to-end system with the capability of harvesting energy from TV and cellular signals in the environment to activate smart cards and grocery tags. It enables ubiquitous communication between inexpensive devices that need near-zero maintenance. Talla et al. [34] harvest WiFi signal to charge low power streaming cameras and sensors. However, passive harvesting is only suitable for battery free devices that need micro watt level power, but not for IoT applications that require higher power.

Far Field Wireless Energy Transfer: Actively transferring energy to the target device has long been proposed as a promising way of transferring heftier power over longer distances. In this paper, we specifically refer to this type of wireless charging systems as WPTs. From the early Tesla’s Wardenclyffe tower to the later Air Force mission of wirelessly powering an unmanned helicopter, until now people are still actively exploring new possibilities in this space. Point source far field WPT methods have lower efficiency than their near-field counterparts due to path loss, $\frac{P_r}{P_t} = G_r G_t \frac{\lambda}{4\pi d^\alpha}$, where we have α between 2 and 8 depending on the environment. For example, with an isotropic receiver and transmitter, the power transfer efficiency can be lower than 0.1% for a 10 meter charging distance. Thus, in order to deliver a certain amount of energy over 10 meters away, it is not realistic to have only one isotropic energy transmitter.

One approach to addressing this challenge is to increase the directionality of

the transmission. Using directional antennas [53] or laser beams [39] can significantly increase the received energy given the same transmitting power and distance. The other approach, however, is based on beamforming, which uses a large array of transmission antennas for enhancing the signal towards certain directions. For example, Ossia [40] and Energous [54], two recent start ups, have created WPT solutions through beamforming by using a large array of WiFi band transmitters. Similarly, WPTs using distributed beamforming have also been investigated in [55, 56, 57], where closed form solutions for distributed beamforming realization and energy delivery efficiency are studied.

We take the viewpoint that far-field active transferring is the most promising approach to enabling a large array of BF-IoT systems with diversity charging energy and distance requirements. In this paper, we propose a new WPT approach that leverages a group of transmitter antennas to increase the delivered energy. Our approach, referred to as *Energy-Ball*, is however drastically different from beamforming based WPTs in that it arranges the transmitter antennas in a completely different manner and thus yields completely different energy density distribution in the charging area. In the next subsection, we will then take a close look at the energy density distribution of these two types of WPT approaches.

3.2.2 WPT Energy Density Distributions and Their Implications on Safety

The risks of excessive RF energy exposure have been studied in the past, which have revealed that harmful biological effects may stem from strong RF radiation [58, 59, 60, 61, 62, 63]. High energy density across the charging space in WPT systems may cause excessive RF energy exposure, which we strive to avoid in the design of *Energy-Ball*.

Existing beamforming based WPTs have unwanted RF energy exposure along

the beam. Due to path loss, the energy density on the beam path is higher than that at the target receiver. Specifically, the simulation results in Figure 3.1 show that on the beam path, the energy density at 1 meter away from the transmitter array is 13 times higher than the energy density at the target receiver. If the beamforming system is designed with only the received energy in mind, without realizing that the energy level on the path may become much higher, then it is hard to guarantee that the energy density on the beam is low enough to meet the FCC regulations or to be safe. FCC establishes different exposure limits for different RF ranges. These limits are codified in Title 47 of the Code of Federal Regulations (CFR). Specifically, as for conventional far field wireless charging frequency of 915MHz, maximum permissible exposure (MPE) for uncontrolled environment is $0.6\text{mw}/\text{cm}^2$ [64]. In addition, due to skin depth effect [65], WPT systems operating at higher frequencies naturally interact more strongly with the human body than lower frequency WPTs [66].

Clearly, guaranteeing safety is one of the key objectives when designing a wireless charging system, especially those that can work over several meters or longer [55]. A safe WPT approach has been investigated in [67]. In this work, under the MPE constraint, the proposed approach selects specific energy chargers for a given set of available energy chargers. On the other hand, a laser based wireless power transfer approach is proposed in [39], where it automatically detects people in its laser beam path and turns the laser beam off. In *Energy-Ball*, as shown in Figure 4.1, the peak energy exists precisely at the target receiver, and it is much higher than the received energy at other locations. Thus, by controlling peak energy level at the receiver at a proper level, the entire charging area should also be safe.

3.3 *Energy-Ball* Design Details

3.3.1 Overview

We have two main objectives when designing *Energy-Ball*:

1. **Precise Wireless Energy Transfer:** Taking a significant departure from beamforming based WPT systems, *Energy-Ball* arranges transmitters around the target devices, like speakers in a surround sound system. When these transmitters align their phases at the target, an energy ball is precisely formed around the target. The received energy density at the target is maximized while the energy density elsewhere is kept low.
2. **Charging Mobile Receiver:** We design an adaptive Kalman filter based framework to quickly re-align phases for mobile receivers. Based on the fact that phase differences between transmitters to the receiver and the receiver to transmitters are correlated, transmitters can estimate the needed phase differences for phase alignment by using their measured phases. Transmitters then adapt their phases locally.

3.3.2 Energy Transfer through Phase Alignment

Energy-Ball has two main components. Firstly, we arrange the transmitters around the target receiver (we will discuss the spatial relationship between transmitters and receiver later in this subsection), and secondly we align their phases at the receiver.

There are various approaches to aligning the transmitter phases. In our implementation, we extend the algorithm presented in [22]. We partition time into rounds of equal duration, and within each round, every transmitter transmits energy to the receiver at several randomly chosen phases, and expects a feedback beacon from the receiver at the end of the round indicating whether any of the

phase combinations gives higher energy than in the previous round. After receiving the feedback, the transmitters choose a phase combination that has given the highest energy level at the receiver, and then performs next round of random phase adjustments around this combination. Repeating this process round by round, the receiver can guide transmitters to adjust their phases towards the optimal phase combination which gives the optimal energy at the receiver. This algorithm does not need complex channel state estimation, and it naturally takes into consideration the multipaths in the environment. Though a heuristic based approach, it always led to fast convergence in many experiments we have conducted on our testbed, mostly because our transmitters emit sine waves which have rather smooth slopes around the peak region. More details on the implementation of our phase alignment algorithm will be further presented in Section 3.4.2.

Can We Form an Energy Ball? Our simulation results show that when all transmitters align their phases at the receiver, we can indeed form an energy ball at the receiver. That is, the energy density at the target is higher than the energy density at any other location within the charging area. For example, in the results presented in Figures 3.3 (a) and (b), we place 100 transmitters equally spaced on the edge of a circle with a radius of 10m, and place the receiver at the center of the circle. Transmitters are isotropic, emitting narrow band RF signal at 1GHz. Signals are coherently added up at the target receiver. Figures 3.3(a) and (b) pictorially show the energy density distribution in a 10×10 meter area around the target receiver in free space and multipath environment (with GWSSUS multipath channel [68]), respectively. In both settings, we witness a sharp energy peak around the target receiver (circled using dotted red circle, the same for other energy distribution simulations). Specifically, the peak to average energy ratio in the free space case is 90.9, while the peak to average energy ratio in the multipath scenario is 81.1. Further, Figure 3.3(c) shows a 3D view of the resulting energy ball and the corresponding transmitter deployment.

Besides having simulation results and actual experimental measurements that show the energy ball, we have also mathematically proved that the energy at the target receiver is indeed the maximum energy across the entire charging area. Interested readers are referred to [69] for detailed proof. Note that in practice, if the number of transmitters is too small (say, 4 transmitters) or the receiver is placed far outside of the transmitter area, the received power at the target location might not be the maximum received power across the entire space. However, this observation still holds in most of the practical settings, as we will later show in Section 3.5.1.

How Small is the Energy Ball? Considering an asymptotically large number of transmitters, we have verified in [69] that the distance between the point that receives the maximum energy level and the first point that receives half of the maximum energy, which is usually called 3dB-down distance (d_{3dB}) in communication, is:

$$d_{3dB} \approx 0.22\lambda. \quad (3.1)$$

We can use d_{3dB} to represent the size of the energy ball, which is proportional to the RF wavelength we use for charging. For an operating frequency of 1GHz, d_{3dB} is around 13cm, which is quite focused. Further, through simulation studies, we find that even for a smaller number of transmitters or asymmetric transmitter placement, d_{3dB} would still be a fraction of λ as long as transmitters are placed around the target receiver.

How Many Transmitters We Need to Form the Energy Ball? In the above simulation studies, we have 100 transmitters. In reality, deploying such a large number of transmitters is not only prohibitively expensive, but will also be hard to achieve synchronization/phase alignment among them.

Figures 3.4(a)-(d) show simulation results of the energy density distribution

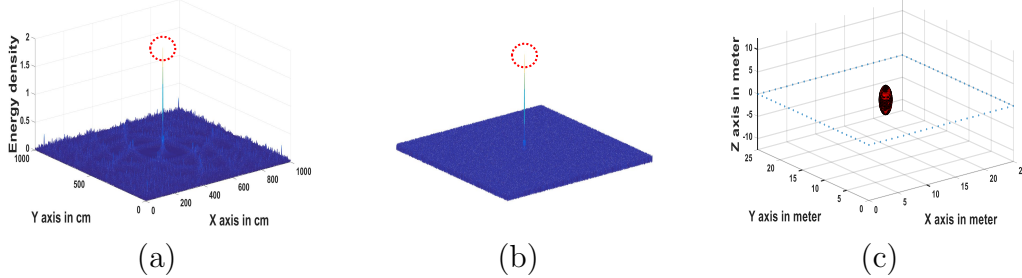


Figure 3.3: When we place the receiver in the center of the transmitter square, (a) shows the energy distribution around the receiver in a 2D plane and (b) energy distribution under a GWSSUS channel, (c) pictorially shows the ‘energy ball’ relative to transmitters in a 3D space, where blue dots mark the transmitters.

around the target receiver with different transmitter numbers. In these simulations, transmitters are still placed on a circle centered around the receiver. The results show that no matter how many transmitters we have, the energy level at the receiver is the highest. Further, when we have 25 transmitters, the peak to average energy ratio is already 13.4. In practice, we built an actual testbed consisting of 24 transmitters, and we will show later in section 3.5 that the energy at the receiver is indeed considerably higher than any other spot.

Does the Receiver Need to be Placed at the Center? We have shown one can form a tight energy ball around the target receiver when placing the target receiver at the geometric center of the transmitters. We next investigate the impact of receiver placement using simulations, in which we consider 100 transmitters that are equally spaced along a 25×25 meter square. We vary the location of the receiver, and look at the energy distribution within a 10×10 meter area around the receiver, which are shown in Figures 3.5(a)-(d).

In Figure 3.5(a), the receiver is placed at the center of the square. In Figure 3.5(b), the receiver is placed within the square, but not at the center. In Figure 3.5(c), the receiver is placed outside of the square, but its distance to the square is comparable to the length of the side (its distance to the center of square is 85 meters). In Figure 3.5(d), the receiver is placed far away from the square (its

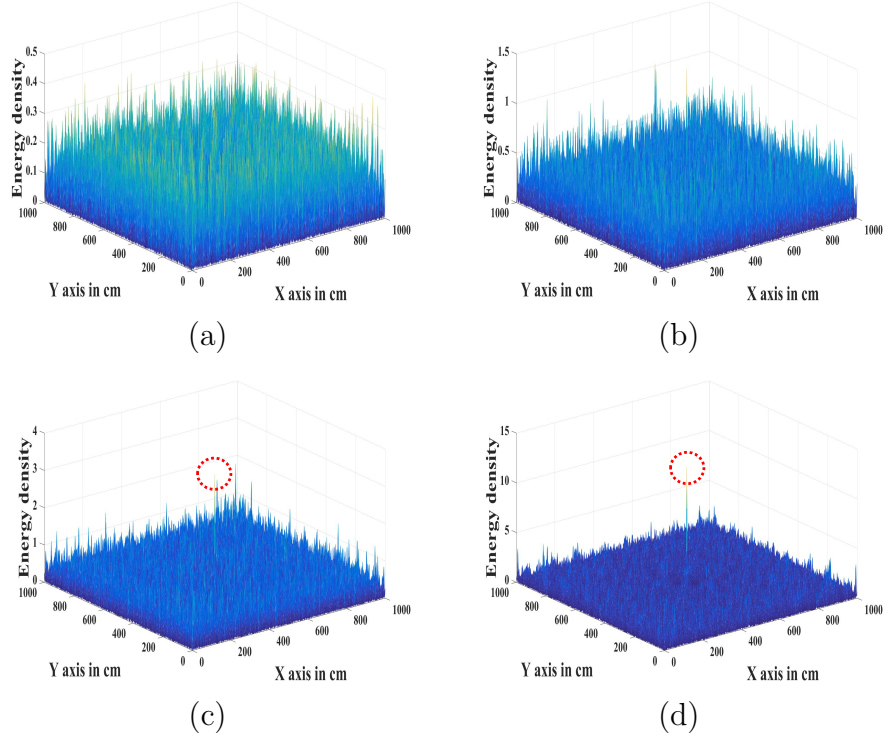


Figure 3.4: Simulated energy distribution around the the target receiver (target receiver is placed at the center) with (a) 8 transmitters (b) 16 transmitters (c) 25 transmitters (d) 50 transmitters.

distance to the square is 200 meters). We observe that, as long as the receiver is within the square, the energy concentration around the receiver is quite narrow, hence precise energy delivery. Once the receiver is outside of the square, the width increases. However, we consider the energy distribution in Figure 3.5(c) still precise, but not in Figure 3.5(d). Through extensive simulations, we observe that, not only do we not need to place the receiver exactly at the center, but the key to precise energy delivery is that *the distance between transmitters and receiver is comparable to the distance between transmitters*. The reason is, when the distance between the transmitters and receiver is much larger than the distance between the transmitters themselves, the setup approaches traditional beamforming and loses the advantage of *Energy-Ball*.

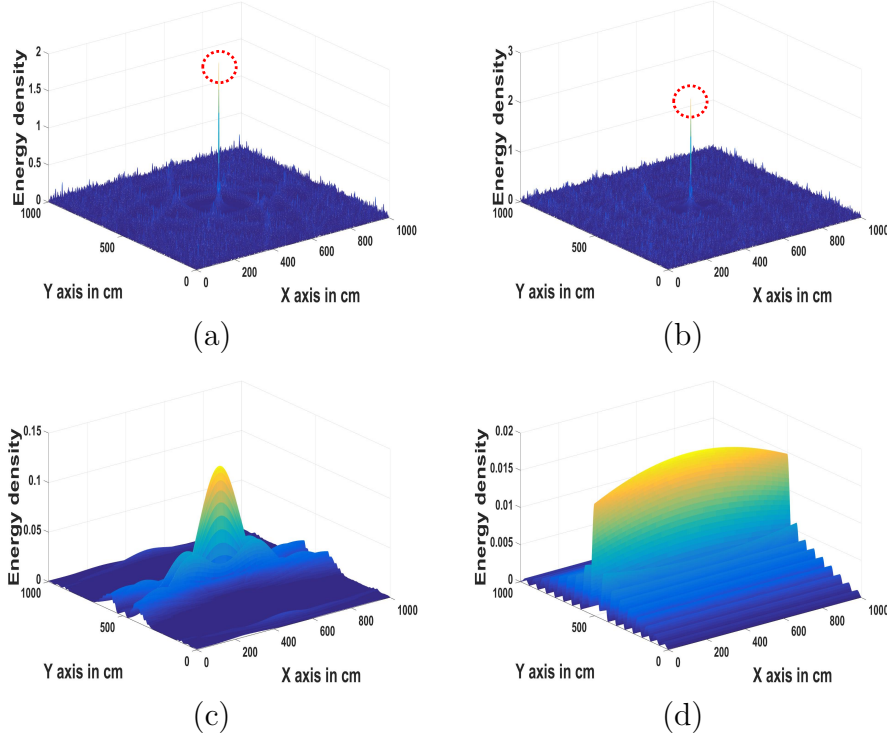


Figure 3.5: Energy level distribution in different transmitter-receiver placement settings: (a) receiver placed at the center of transmitter square; (b) receiver placed in the transmitter square, but not the center; (c) receiver placed outside of transmitter square, but close; (d) receiver placed further away to the transmitter square. Among these four cases, the energy ball is formed in the first three case.

3.3.3 Charging Mobile Receiver

The second salient feature of our system is the ability to focus energy to devices while they are moving. Below we discuss how we manage to charge mobile receivers.

Channel Reciprocity and Channel Correlations

The key to charging a mobile receiver is the ability to quickly focus the transmitters' phases at the new location of the mobile receiver as it moves. In order to ensure smooth re-alignment, it is important to align each transmitter's phase in a timely manner. Indirect methods such as inferring phase differences by observing the Received Signal Strength (RSS) value at the receiver [22], are not sufficient

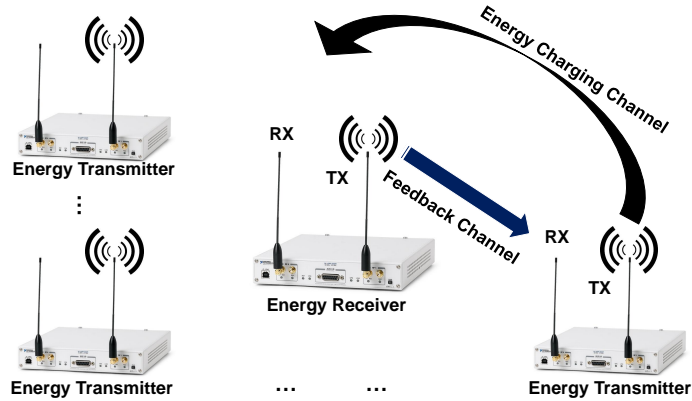


Figure 3.6: Each radio device has separate ports for transmitting and receiving. We define the channel from the transmitter to receiver as ‘energy charging’ channel, and the channel from the receiver to transmitter as ‘feedback’ channel. These two channels work at different frequencies but are correlated.

because the convergence process may take tens of seconds. Meanwhile, sequential methods in which each node’s phase is adjusted one by one [70, 71] are also not fast enough.

In this study, we deal with this problem as follows. If we assume all the nodes are synchronized, and the channel is time invariant, then the link from the energy transmitter to receiver (referred to as the energy charging channel) and the link from the receiver to transmitter (referred to as the feedback channel) are **reciprocal** – the absolute values of phase differences on these two channels should be the same [72, 73, 74, 75]. Hence phase alignment can be quickly realized by taking advantage of channel reciprocity. Specifically, we can have the receiver broadcast pilot beacons to all transmitters, such that each transmitter can measure the phase difference and then adjust its phase locally according to the measured phase difference.

Unfortunately, the above method requires the two channels to be strictly reciprocal, which in turn requires all the nodes to work in a dedicated Time Division Duplex (TDD) fashion¹. That is, both the transmitter and receiver should have

¹The full duplex radio is the best candidate to align phases using the channel reciprocity, however it involves even more complex hardware and software design.

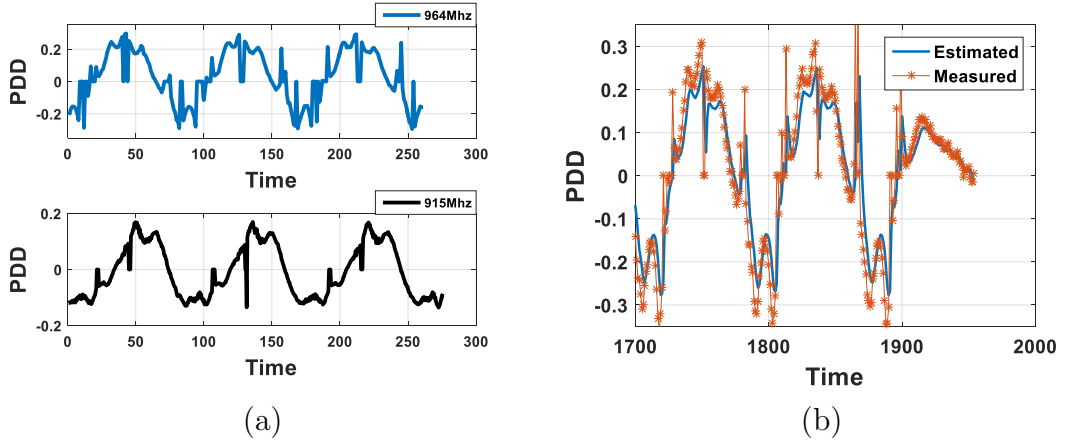


Figure 3.7: (a) PDD at 915MHz and 964MHz channel. Measurement results indicate the PDDs are correlated for these two different channels. (b) Estimated energy charging channel PDD from the adaptive Kalman filter. We also show the measured energy charging channel PDD as the ground-truth. This result suggests our phase estimation algorithm for mobile receiver is indeed accurate.

an antenna that can switch between receiving and transmitting without re-locking its phase. The TDD mode requires a specifically designed hardware that is not readily available on most low-cost IoT nodes. Instead, it is more often that nodes work in the Frequency Division Duplex (FDD) mode. As shown in Figure 3.6, in this setting, each node will use two RF ports, one for transmitting and the other for receiving, both working simultaneously but at different frequencies. These two ports are spatially separated but close to each other.

Perfect channel reciprocity does not hold in our case since the energy charging channel and the feedback channel work in different frequency bands that have different multipaths [76, 77]. However, considering the fact that the two ports on a node are very close, and the receiving antenna and transmitting antenna on the energy receiver move in a correlated trajectory, we have the hypothesis that the phase difference values for these two channels are highly correlated.

We have conducted experimental investigations to confirm this hypothesis. Specifically, we use two USRP N210s and configured each USRP to transmit and receive using two different antennas. The two USRPs are synchronized by GPS

where one is transmitting at 915MHz and receiving at 964MHz while the other is transmitting at 964MHz and receiving at 915MHz. Then we attach the two antennas of the receiver USRP to a rotor, which spins at a constant speed of 0.4m/s. Figure 3.7(a) shows the measured phase difference derivatives (PDD) – the differences between adjacent phase difference values for a feedback rate of 20Hz – at different frequencies. We observe that the two channels' PDD values exhibit strong correlation and have similar trends. Hence, we believe our hypothesis is true and can estimate the phase differences at the energy charging channel using the phase differences from the feedback channel. As such, transmitters can measure the phase difference on the feedback channel, estimate the phase difference on the energy charging channel, and then adjust their phases locally to achieve rapid phase alignment.

Phase Estimation Using Adaptive Kalman Filter

We adopt an adaptive Kalman filter based estimation method. On a transmitter node, we can model the received beacons as a state space model, in which y_n denotes the n -th feedback channel PDD, and x_n denotes the n -th energy charging channel PDD. We have the following:

$$x_{n+1} = Ax_n + w_n, \quad y_n = Cx_n + v_n. \quad (3.2)$$

The signals w_n, v_n are mutually-independent, zero-mean, white-noise signals with covariance matrices Q_n and R_n : $E[w_n w_i^T] = Q_n \delta_{ni}$, $E[v_n v_i^T] = R_n \delta_{ni}$, and $E[w_n v_i^T] = 0$.

We first use our observed x_n and y_n data for pre-processing. Specifically, the initialization Kalman filter parameters $\theta = [A, C, Q, R]$ are calculated by Expectation Maximization (EM) [78] algorithm from the pre-processing data. Next, in order to timely estimate x_n , we pass y_n through the initialized Kalman filter and adopt EM algorithm to adaptively update the Kalman filter parameters

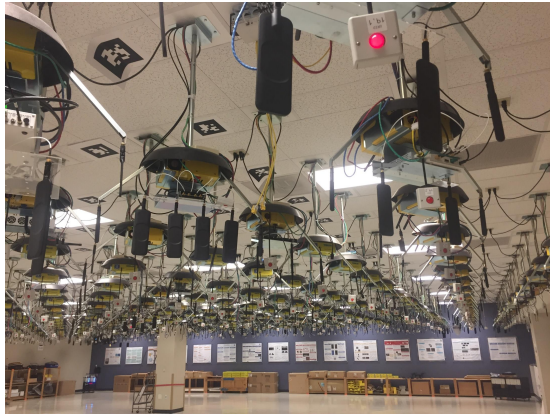


Figure 3.8: Real world *Energy-Ball* testbed.

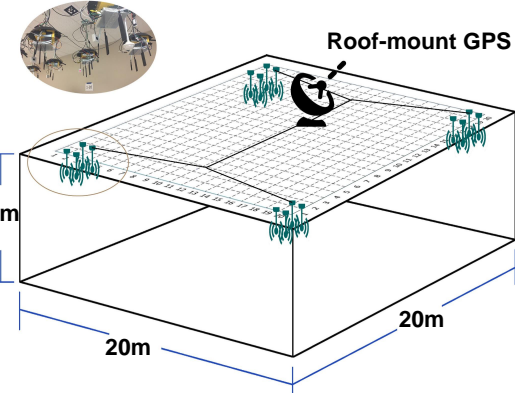


Figure 3.9: The illustration of *Energy-Ball* setup.

$\theta = [A, C, Q, R]$ periodically. Specifically, each transmitter estimates and adjusts its new energy charging channel PDD x_n upon receiving a feedback beacon, and each transmitter updates its Kalman filter parameters using EM algorithm upon receiving every M beacons. In this way, each transmitter can locally adjust its phase to achieve rapid phase alignment. Figure 3.7(b) shows an example PDD estimation sequence. The estimated energy charging channel PDD values (blue curve in Figure 3.7(b)) are in close agreement with the measured PDD values (orange dots in Figure 3.7(b)). In this experiment, the average PDD estimating error is 2.4 degree, which is more than enough for achieving distributed phase alignment for our purpose².

3.4 Building *Energy-Ball* Testbed Using USRPs

In order to implement and evaluate the *Energy-Ball* design presented in Section 3.3, we develop an actual testbed consisting of 17 N210 and 4 B210 USRP nodes.

²Through simulations, we find that as long as the transmitter's phase is within 45 degrees of the optimal phase, *Energy-Ball* can still reach at least 90% of the optimal energy at the receiver. Hence, we do not require the transmitter phases to be exactly the optimal value.

3.4.1 Testbed Setup

USRP Deployment and Configuration: We deploy 16 USRP N210 and 4 B210 as transmitters, which are mounted on the 3-meter high ceiling of our laboratory, forming a $20 \times 20 m^2$ area. Another N210 acts as the receiver in our testbed. It keeps broadcasting feedback beacons to all transmitters to guide their phase adjustments towards the optimum. Our working frequencies are 915 and 964 MHz in this study. The maximum output power for each transmitter in our testbed is around $71mw$ ($18.5dbm$). We use a WBX RF daughterboard on the USRPs. There are two RF ports on each N210 and four RF ports on each B210, in total we have 24 transmitters. Transmitters and the target receiver work in FDD (with different antennas for transmitting and receiving) full duplex mode. The energy charging channel is set as 915MHz narrow band, and the feedback channel is set as 964MHz.

The receiver is set up on the floor, and the receiving antenna is attached to our specifically designed robot, making it easier to change the receiver location. Transmitters' antennas are fixed, TG.35.8113 in our testbed, with quasi-isotropic radiation patterns and low return loss in 915 and 964 MHz. The testbed itself is shielded from outside, but the indoor RF multipath situation is quite complex. Our testbed is housed in a cluttered laboratory, with floor, walls, and ceiling made of high reflection materials.

Figure 3.9 shows a typical testbed deployment, 4 *N210s* and 1 *B210* at each of the four corners of the ceiling, with 1 meter between them. There is no communication channel between the transmitters. We could place the receiver anywhere in the deployment area.

GPS Synchronization: We synchronize the transmitters through a master-slave GPS system. Specifically, we use a rooftop-mounted GPS antenna that provides reference signals (as the master clock) to the indoor GPS splitter. An

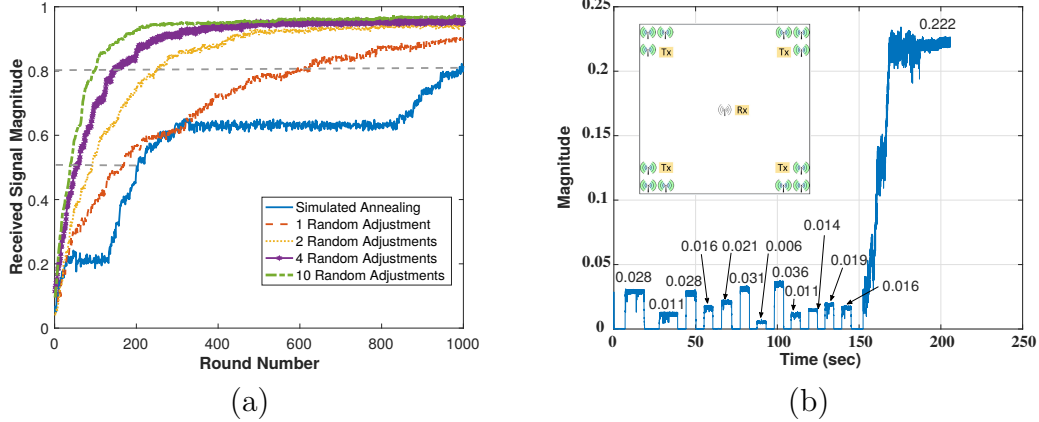


Figure 3.10: (a) Convergence speed comparison for algorithms in different random adjustments N and simulated annealing. Phase alignment with larger N converges faster. (b) In the first 150 seconds, we turned on/off and measured 12 transmitters one by one. After time 150, we turn on all transmitters and started phase alignment. RSS quickly converges after that.

Octoclock-G unit containing a GPS disciplined oscillator (GPSDO) generates the PPS and 10MHz reference signals which are distributed via equal length cables (75ft + 7.5ft) to 8 other Octoclock units which do not have GPSDOs. Four of these Octoclock units are installed in the corners of the testbed to split the reference signals using equal length cables (10ft). The use of equal length cables and a symmetric topology ensures that all connected devices will see the same reference signals with little deviation in phase and time.

Distributed Phase Alignment: How to achieve phase alignment is orthogonal to the design of *Energy-Ball*, and we can potentially pick any practical phase alignment algorithm. In this study, we build our phase alignment algorithm on the 1-bit phase alignment algorithm that is proposed in [79, 22]. That is, upon receiving a 1-bit feedback from the receiver, transmitters will randomly adjust their phases. The energy receiver will measure the resultant energy level, and send a feedback to indicate if this phase adjustment has led to a better received energy. If yes, the transmitters adopt this new phase combination; otherwise, they continue to use their old phase combination. In either way, at the end of each round,

the transmitters keep the best phase combinations they have attempted thus far. Repeating this process, the transmitter phase combinations will approach optimal values that result in the optimal energy level at the receiver. In this study, we extend the 1-bit phase alignment algorithm. In each round, instead of trying one phase adjustment, the transmitters try N different phase adjustments. The receiver will then notify the transmitters whether any of the N new phase combinations gives higher energy than the old phase combination; if yes, which new phase combination is the best.

Our extension converges much faster compared to the 1-bit algorithm. Figure 3.10(a) shows simulation results (with 100 transmitters) of convergences for several different N values, with the simulated annealing algorithm [80] and 1-bit algorithm ($N = 1$) as baseline results. The results show that the convergence is significantly faster than base line algorithms with larger N .

Figure 3.10(b) shows an example experiment of real world distributed phase alignment. There are 12 transmitters in this experiment, the feedback rate is 20Hz and $N = 2$. In this experiment, we turn on and off 12 transmitters one by one to record the RSS contribution from each transmitter in the first 150 seconds. After 150 second, we turn on all transmitters and run the phase alignment algorithm. The RSS converges to near optimal after 9 seconds. Specifically, the optimal RSS is 0.222, and *Energy-Ball* reaches of the optimal RSS in this experiment.

3.4.2 GNU Radio Implementation

Signal processing tasks are performed by the GNU radio version 3.7.6.1. An overview of implementation flow for transmitters and the receiver is illustrated in Figure 3.11. We write multiple out-of-tree GNU radio modules to implement our functions. We next describe the GNU radio signal processing flow in detail.

Transmitter Side

The transmitters first receives feedback beacons in a narrow band 964 MHz channel by a USRP Hardware Driver (UHD) source block. Then after low pass filtering, the transmitter demodulates the incoming signal using the preset width-value mapping and guard band design in the demodulation block. By changing the threshold parameter on this block, we can calibrate the threshold that differentiates noise and beacons at the beginning of each experiment. This is important since the experimental environment is changing with time. The transmitter will do different tasks according to the demodulated beacons.

Stationary Scenario: The transmitter applies N phase adjustments after demodulating the beacon in the next block. Note that the transmitter holds its phase for the period of a slot τ , $\tau = t/N$, where t is the duration for a round, we set $t = 50ms$ in our testbed. Due to the complexity involved in having large N values, we implement $N = 2$ in our testbed. At last, after an output control block, the transmitter sends out the narrow band 915 MHz phase adjusted signal by a UHD sink block.

Mobile Scenario: The transmitter measures the phase difference of each incoming beacon and calculates the PDD accordingly. Within each incoming beacon, every two adjacent samples will yield out a phase difference, and the phase difference of this beacon is calculated by averaging the phase difference of all adjacent samples. Since USRP could only calculate wrapped phases, we apply Fast Fourier Transform (FFT) for each beacon to do phase unwrapping before calculating the phase difference.

Then the calculated PDD is sent to the Kalman filter to estimate the PDD of 915MHz channel. Lastly the transmitter adjusts its current phase using this estimated new phase. The Kalman filter parameters are updated by the EM algorithm once for every 60 beacons.

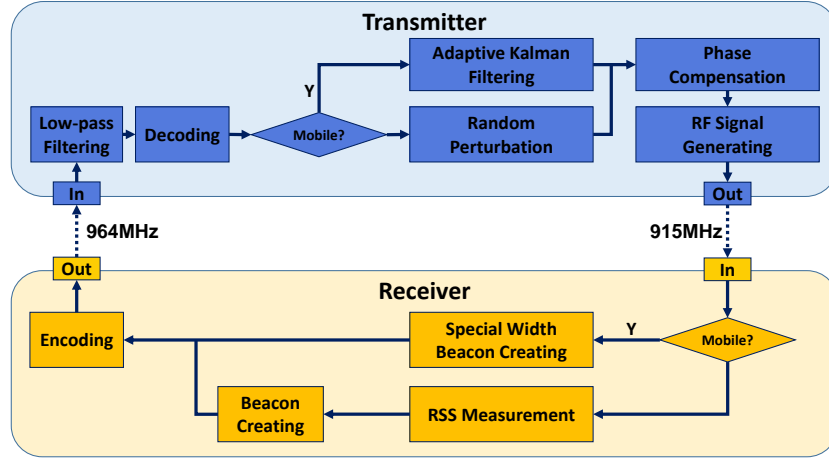


Figure 3.11: *Energy-Ball* TX and RX signal processing flow.

Receiver Side

The receiver acts as a coordinator for transmitters, sending out instructions to guide the transmitters' phase adjustment towards constructive interference among them. By broadcasting different beacon width, the receiver sends different beacons to indicate if its stationary or mobile.

Stationary Scenario: The receiver first receives all incoming signals in a narrow band 915 Mhz channel. In the following block, after low pass filtering, the receiver measures the received energy by averaging the RSS of all incoming signals for each of the N phase adjustments. It sends out an instruction to the next block at the end of each round after comparing the average RSS values for each phase combination, telling the next block which phase adjustment in this round has the highest energy. Then, the next block modulates a width-based beacon following the preset width-value mapping. Finally, this beacon is sent out by the last UHD sink block in a narrow band 964 MHz channel. In our system, the receiver broadcasts 20 beacons every second. Hence it has to process receiving signal every 50 milliseconds.

Mobile Scenario: In this case the receiver keeps broadcasting 20 special width

beacons every second. Transmitters measure the phase difference of 964MHz channel according to this beacon.

Robust Pulse-width Modulation Feedbacks

Next, we take a closer look at the feedback mechanism for the receiver. In the feedback control phase alignment method, the receiver sends feedbacks to transmitters to signify which phase combination out of the $N + 1$ options gives the strongest signal to the receiver. Below, we use $N = 1$ to simplify the discussion. In this case, the feedback has two values, 0, meaning the transmitter should use its old phase value, and 1, meaning the transmitter should adopt the randomly picked phase value. In [81], the receiver feedback uses signal amplitude to modulate: low amplitude denoted as 0 and high amplitude denoted as 1. Such a scheme requires two preset amplitude thresholds, one threshold for differentiating noises and valid feedback beacons, while the other for differentiating lower amplitude from higher amplitude. Choosing suitable amplitude threshold values, however, is quite challenging as different settings have significantly different radio environments; even the same setting may experience considerable fluctuation with time. Also, N feedback control phase alignment method needs $N + 1$ vulnerable thresholds, which is extremely difficult to realize while the receiver is moving. In [82], a GMSK-based feedback scheme is used, which only requires one threshold to differentiate noise from feedback beacons. On the downside, it requires phase-level synchronization among the transmitters and receiver, which is not always available in such a distributed system.

In order to address this issue, we choose to adopt a width-based modulation method and show that it is simple but robust. In each round, the receiver broadcasts a feedback beacon that has $N + 2$ possible widths, in which $N + 1$ different widths are for feedback control phase alignment method while the receiver is stationary and another special width is used for adaptive Kalman filter while the

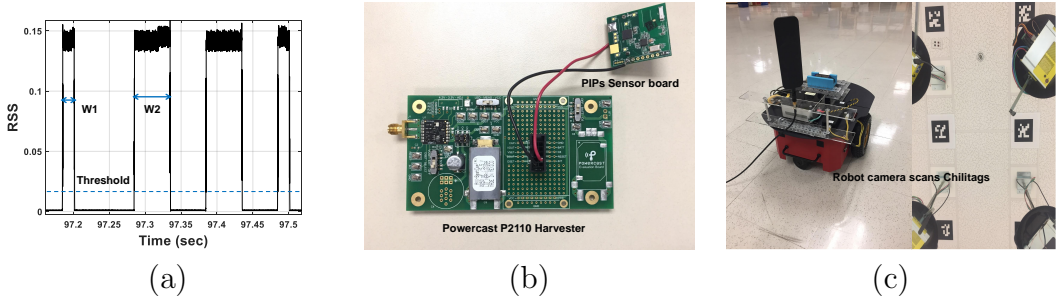


Figure 3.12: (a) We use different beacon width to indicate feedback information. Only one threshold is used to differentiate environmental noise and beacons. (b) Powercast P2110-EVB board and our PIPs sensor board. (c) Energy measurement robot scans Chilitags (on the ceiling) for navigation.

receiver is mobile. The mapping between beacon width and specific values is pre-determined and known to each transmitter and receiver. After receiving a feedback beacon, transmitters infer its value based upon the beacon width and the pre-determined mapping. It is very likely that the received beacon width does not exactly match any of the preset values, and so we set a small tolerance space $\delta = \pm \frac{d}{5}$, where d is the expected beacon width, as a guard band (in time domain) to address this problem.

Compared to amplitude-based feedback beacons, width-based beacons are more robust since they only need one threshold to decode the feedback (the threshold differentiating environmental noise and receive beacons, shown in Fig 3.12(a)). We note that the downside of the width-based beacon scheme is the relatively limited beacon values it can support, which is not a concern in our system because large N values are not realistic anyway.

3.4.3 Experimentation and Measurement Tools

Energy Harvester and Low-Power IoT Sensors:

In the testbed, we utilize the delivered energy to power an in-house low-power IoT sensor, PIPs [45, 83, 84], which has been designed for smart building applications.

Figure 3.12(b) shows the PIPs board and the energy harvester board. A Powercast P2110-EVB [85] serves as the energy harvester in our system. It converts input RF energy into DC energy, charging a 500uF capacitor on the P2110-EVB board. The output voltage of P2110-EVB is then set as 3.3v by a regulator and the regulator will only be turned on when the voltage across the capacitor exceeds 1.2v. The regulator consumes the stored energy in the capacitor. Note at 915Mhz, the P2110-EVB energy harvester has around 50% RF-DC efficiency. Hence the actual rectified DC power received at the end device is less than the absolute delivered RF power.

We charge PIPs by using the 3.3v output voltage. An Agilent E4405B [86] is used to measure the absolute incoming RF signal strength. Though the harvester could be turned on as long as its input RF signal strength is over -12 dbm, around -7 dbm signal strength is needed to make the regulator work continuously. Otherwise, voltage between the capacitor pins would drop while powering the regulator, hence failure to provide a stable 3.3v output voltage.

PIP is an ultra low-power sensor board, consisting of a moisture, temperature, and magnet open/close sensor. Normally, PIP is powered by a coin cell. Here we configure PIP such that it collects and reports data every 10 seconds. It takes $45.7 \mu J$ to collect and transmit data, and consuming $3 \mu W$ to stay idle.

In order to charge PIPs, we first attach the receiver N210's antenna onto a tripod with a coax cable and run feedback control phase alignment method to achieve the optimal energy at the receiver. Next, keeping the receiving antenna in the same location, we connect it to the P2110-EVB harvester board that converts the received RF energy to DC energy. As soon as sufficient energy is generated, PIPs would start transmitting sensed data to its receiver.

Energy Measurement Robot:

Figure 3.12(c) shows a picture of our energy measurement robot and Chilitags on the ceiling. The robot is controlled via ROS (Robot Operating System) [87] and it's a Pioneer-p3dx robot [88]. The robot is differentially driven, and uses a Logitech c920 webcam for localization via the Chilitags library [89]. There are approximately 460 11" by 11" fiducial markers placed in a grid on the ceiling with a one meter spacing. For the purposes of this experiment, the robot was controlled via teleoperation, though it is designed to be operated autonomously. The Rosaria package provides a ROS compatible interface to the robots on-board controller, allowing any other program in the ROS ecosystem to communicate with it. A simple logger was created in python to record the robots position, and plot the path that the robot followed during the experiment.

Spectrum Analyzer and USRP Calibration:

We use a spectrum analyzer Agilent E4405B to measure the absolute RF channel power. The spectrum analyzer can be used for acquiring absolute channel power on USRPs. USRPs can only measure RSS without units. But since the RSS measured on USRPs and their daughterboards is linear to the absolute RSS [90], we can figure out the absolute measured power on a USRP by calibration. Specifically, we set a USRP N210 broadcasting RF energy constantly, and we connect the receiving antenna to a calibrated spectrum analyzer through a coax cable to measure the narrow band 915 MHz channel power. While keeping the receiving antenna at the same location and RF source USRP broadcasting the same signal, we then disconnect the coax cable from the spectrum analyzer and connect this cable to the receiving RF port of another USRP. By this calibration process, we can map the unitless USRP measured RSS to the absolute power (in Watt).

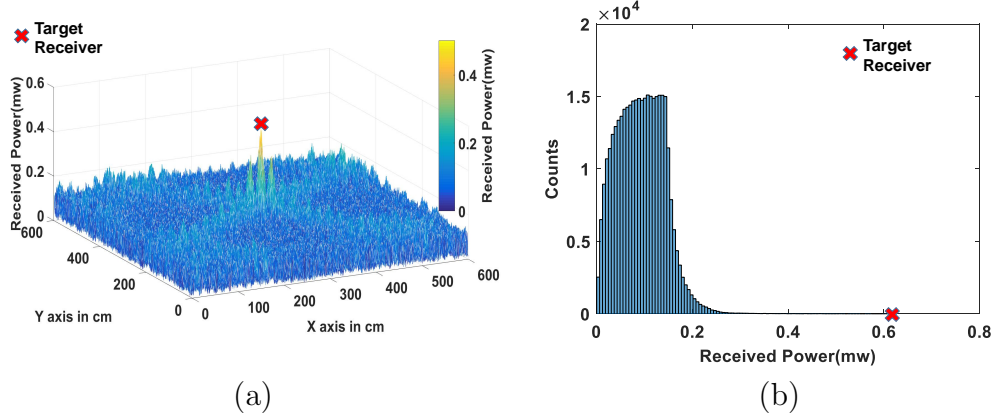


Figure 3.13: Using the topology shown in Figure 3.9, we measure the power level distribution of *Energy-Ball* in a 6×6 meter area centered at the receiver. (a) presents the 3D view of distribution, while (b) presents the histogram of the power level measurements. The distribution clearly shows that the energy density level at the receiver (marked by the red X) is much higher than that at other spots within the measurement area.

However, we note that our calibration process does have limitations. For instance, the receiving RF port on USRP N210s most likely saturates if the received RF power exceeds 9dBm (around 7.9 miliwatt), in which case the USRP likely loses its linearity between the recorded RSS and the absolute received RF power. As a result, we limit the received power accordingly in our experiments.

3.5 Evaluation

Using the USRP-based testbed, we have conducted thorough and carefully designed experiments to evaluate the proposed merits of *Energy-Ball*. We also demonstrate *Energy-Ball* can charge PIPs sensors across the room, enabling battery free IoT communication.

3.5.1 Energy Density Distribution of *Energy-Ball*

First, we measure the energy density distribution in the charging area. We show that with *Energy-Ball*, the energy level at the target receiver is the maximum

across the entire area. We have also implemented a traditional beamforming based WPT system and compare its energy distribution pattern with *Energy-Ball*.

Experimental Setup: We use the topology shown in Figure 3.9 for *Energy-Ball* implementation in this experiment. On the other hand, for comparison, as shown in Figure 3.14(a), we custom build a beamforming rack which has 16 transmitting antennas and 16 receiving antennas to perform MRC [41] beamforming based WPT.

The main challenge in conducting this experiment is measuring the energy distribution in the area. Manually sampling the area would take a significant amount of time (e.g., tens of hours), and it is very hard to keep the radio environment around the receiver stable within this period. Performing parallel measurements with multiple USRPs is not a viable approach either, due to differences in their hardware.

We thus use a specifically designed robot to address this challenge. The receiver's antenna is attached onto the robot. In this method, as soon as the phase combining at the receiver stabilizes, we stop the receiver from sending feedback messages. As a result, the locked phases at the transmitters lead to coherent

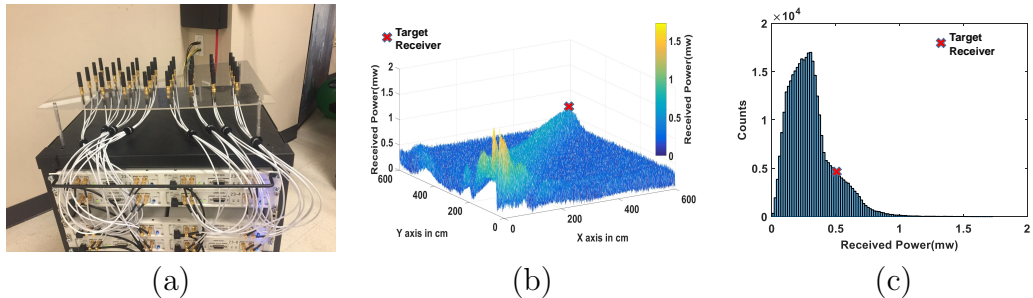


Figure 3.14: Comparison experiments show the energy distribution of beamforming WPT systems. (a) Real world set up of our 16 by 16 beamforming USRP Rack. (b) Measured received power in the area between the beamforming rack and target receiver. (c) Statistics of measured power, there are still lots of locations have received power greater than the target receiver.

phase combining at the original receiver's location. Next the robot will traverse the intended scanning area by a preset trace, which will cover the intended area as much as possible. Meanwhile the receiving USRP is recording the RSS during the whole process, and the RSS values are eventually mapped to their corresponding locations by comparing the timing information of the robot and the receiving USRP. During our experiment, we also make sure that the observed $RSS_{combined}$ value at the energy delivery destination (the original receiver location) does not have noticeable variation.

Results: In our topology (shown in Figure 3.9), we have measured a $6 \times 6 m^2$ (this size is limited by the maximum length of the coax cable) rectangular area around the receiver. Figure 3.13 (a) shows the measured received power distribution in a 3D view. We clearly witness a sharp energy peak around the target receiver location, while the energy at other locations are very low. Figure 3.13(b) shows the statistics of measured received power from the robot: the received power at target receiver is 0.63mw, which is the maximum received power of all measured spots. 62% of measured received power is less than 0.063mw and 99% of measured received power is less than 0.31mw.

As far as the MRC beamforming based WPT is concerned, Figure 3.14(b) shows the measured received power distribution. A strong energy beam projects toward the target receiver, and most of the received powers (89% of measured locations on the line of main beam) on this beam are higher than the received power at the target receiver. Figure 3.14(c) shows its statistics: received power at target receiver is 0.54mw, but there are 8% of measured spots have received power higher than the target receiver.

We note that on our facility, we cannot move these USRP antennas around, and as a result, the distances between the transmitters and the receiver in these two systems are different. Because of this, it is hard for us to directly compare the delivered power amount in both systems, nor can we compare their charging

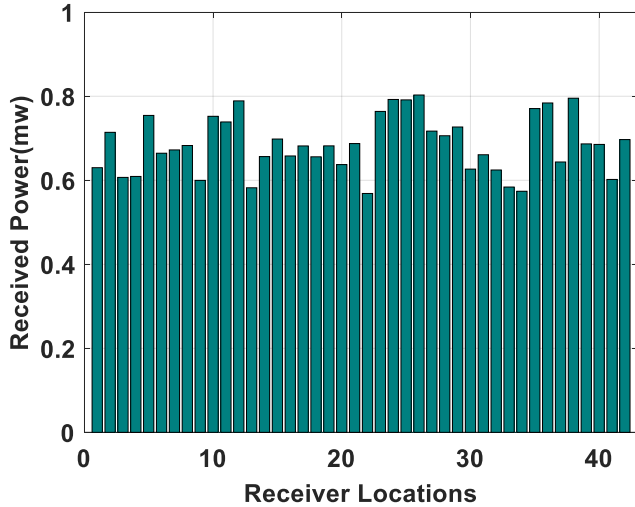


Figure 3.15: In our $20 \times 20 m^2$ test area, we place the *Energy-Ball* receiver at 42 locations, in which location 1 is the center of the area and the other 41 locations are randomly chosen. We show the received power at each of these receiver locations here. Results show the received power at most of the locations is higher than the received power level at the center of the deployment area (location 1).

efficiency. However, we do see that these two systems lead to very different energy density distribution patterns. *Energy-Ball* has the energy peak only at the target receiver. Specifically, the peak/average received power ratio in this experiment is 8.72. As we noted in Section 3.2.2, these patterns potentially have different implications on safety of the system especially when the delivered energy amount goes up.

3.5.2 *Energy-Ball* Delivers Energy at Any Point across the Room

We have built a $20 \times 20 m^2$ area testbed. We now show *Energy-Ball* can align phases and delivery energy at any point within this area. For this purpose, we place the target receiver at 42 different locations, measure the delivered energy at each spot, and show the results in Figure 3.15. Among these 42 locations,

location 1 is the center of the charging area while the other 41 locations are randomly chosen. Specifically, the received power at location 1 is 0.57mw . When we move the receiver to a different location, our system re-align transmitters' phases. Experiment results show they all converge to over 90% of the optimal received power. Among these 42 measurements, the minimum, average and maximum received power are 0.51mw , 0.63mw and 0.74mw , respectively.

3.5.3 *Energy-Ball* Charges Mobile Receivers

Next, we show that our *Energy-Ball* testbed can successfully deliver energy to a mobile receiver as well. In this experiment, the trajectory of the mobile receiver is unknown to the transmitters.

Experimental Setup: We mount the receiver on our robot that moves on a straight line at constant speeds, 0.1, 0.2, 0.3, 0.4, 0.5 m/s. Here, as shown in Figure 3.16(a), while the robot is stationary, we first measure optimal energies at 13 different positions along each moving track of 0.6m. Then the robot starts moving on a straight line as well as running *Energy-Ball*. We did this experiment for 13 times at each speed. The receiving USRP records received power data on the target receiver while the robot is moving. We use the average of 13 optimal measured energy as reference (100%), we compare the received power among (1) different moving speeds and (2) the performance between *Energy-Ball* is working and *Energy-Ball* is not turning on.

Results: Figure 3.16(b) shows around 80% of optimal received power is received for mobile receiver while *Energy-Ball* is working, only 14.7% of optimal received power is received while we turn off *Energy-Ball*. The adaptive Kalman filter design enables the mobile target receives significantly more energy, which is comparable with optimal energy (when the receiver is stationary). This result also suggests the received power under these 5 different tested speeds are similar.

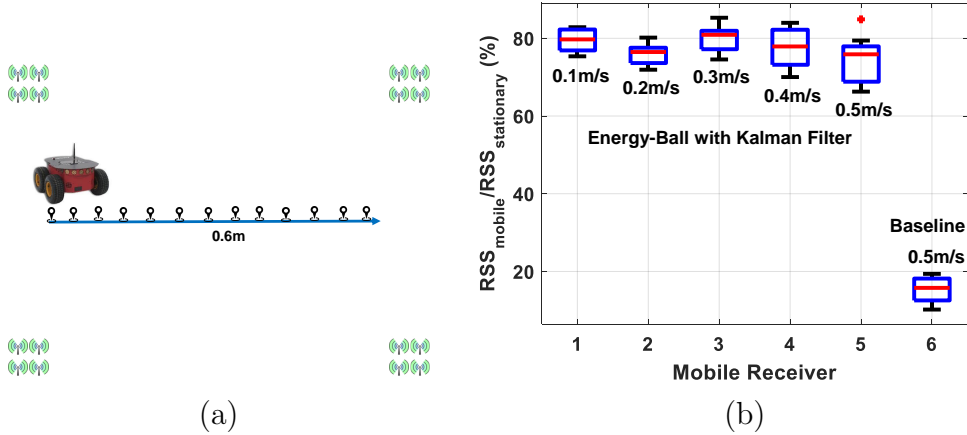


Figure 3.16: (a) We place the receiver on the robot, which moves at a constant speed along a 0.6 meter long trajectory. We measure received power at 13 different positions on the trajectory (transmitters are placed at 4 corners). (b) The received power percentage values at the mobile receiver with different moving speeds. The rightmost box represents the received power percentage value when *Energy-Ball* is turned off (transmitter phases are still aligned to the original receiver location).

3.5.4 Application Example- Charging Low-Power PIPs Sensors

Lastly, in this subsection, we provide evaluation results of charging PIPs (hardware details are given in Section 3.4) through a Powercast P2110-EVB harvester. With the delivered energy, we show that the PIPs sensor board is able to work without battery.

Enabling Battery-less IoT: In this experiment, we place PIPs in 13 randomly chosen locations in the charging area. At all 13 locations, *Energy-Ball* delivers over 0.6mw power that enables PIPs sensing and transmitting data continuously. The measured minimum, average and maximum received power across the room are 0.61mw , 0.67mw and 0.79mw respectively. Figure 3.17(a) shows a portion of the reported sensor data from the sensor charged by our testbed. We observe no dropped packet during the entire experiment.

Powering Specific PIPs through Precise Energy Delivery: Next we place

the harvester and PIPs in location 7-14 (red square in Figure 3.17(b), O in Figure 3.17(c)). After a short charging period, the PIPs board is powered and begin to collect/report data continuously. Again, we observe no packet drop during the entire experimentation period.

With transmitters' phases locked, we move the harvester and PIPs to other locations (we move PIPs's location instead of having a different sensor at that location because we don't have enough number of power harvesters):

- *A short distance (wavelength 30cm) away from the energy focus.* We move the PIPs one λ (around 30 cm) away from the focus point O , i.e., A, B, C, D in Figure 3.17(c) (still within the red square in Figure 3.17(b)). At these locations, the harvester can be charged slowly but PIPs fails to work continuously. For example at location A, PIPs could work for 90 seconds then it is down for a 20 minutes to charge, because the charging speed of P2110-EVB's on board energy storing capacitor is less than the rate of energy being consumed.
- *Farther away from the energy focus.* Next, we move the harvester and PIPs further away, to locations 7-13, 7-12, 8-14, 9-14, 7-15, 7-16, 6-14, 5-14, 15-15, 13-16, 15-7, and 7-6, one by one. As expected, PIPs did not get charged to a level where it could sense/communicate. These locations are marked by blue squares in Figure 3.17(b), and summarized as 'others' in Figure 3.17(c).

End-to-end Efficiency: Since our transmitters work in far-field settings, the end-to-end energy transferring efficiency ($p_{rx}/\Sigma p_{tx}$) is rather low, ranging from 1/1000 to 1/3000 across our 20 by 20 meter testbed. However, it is the physical limitation of any far-field WPT system. The end-to-end efficiency could be increased by using directional transmitters. We argue that such an energy delivery system is still valuable, mainly because the value of transmitted power and the value of received power is often asymmetric, especially if the receiving node is

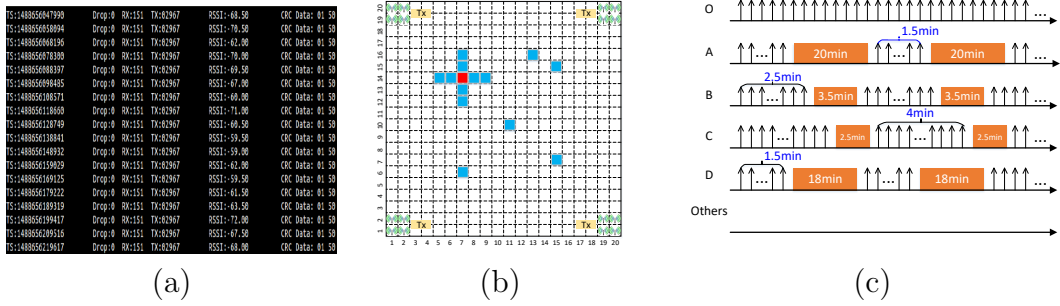


Figure 3.17: In this experiment, we investigate whether sensors at locations other than the target can be powered. (a) Data reported by PIPs, including timestamp, dropped packet ID, server ID, sensor ID, RSSI and sensed data. (b) shows the experiment set up where the target sensor (O) is in the center of the red block, and A , B , C , and D are within the red blocks, 30cm away from O , and a few others are located in the blue squares. (c) shows how sensors at different locations operate when the energy is focused at O . O can work perfectly, $A-D$ can work partially even though they are only 30cm away, and those sensors that are placed in the blue blocks do not have sufficient power to sense or communicate.

in a hard-to-access region. As IoT devices are made increasingly low-power, this concern becomes less severe.

3.6 Conclusion

In this work, we present a new WPT approach that transfers wireless energy to intended receivers by arranging a group of distributed transmitters around the receiver and coherently combining their phases at the receiver. This approach is a departure from existing beamforming based WPT approaches which have high energy on the energy beam path. The key innovation of our approach is that it can maximize the received power solely at the receiver, and have low received power at other locations across the space. Through detailed evaluation using 21 USRP nodes across a $20 \times 20m^2$ area, we show that the proposed approach can maximize the power level at the target receiver, can deliver a consistent amount of power to any point in the area, can charge a mobile receiver, and can continuously power a low-power IoT node at any point across the area.

Chapter 4

Towards Flexible Wireless Charging for Medical Implants Using Distributed Antenna System

4.1 Introduction

Each year millions of patients improve their quality of life through medical implants [91]. These devices are inserted into the human body to replace a missing body part [92], modify a body function [93], or provide supports to organs and tissues [94]. While functional innovations on medical implants are going full steam ahead, the amount of energy required by these devices remains substantial. Though cutting-edge batteries could enable medical implants (*e.g.*, pacemaker [95]) to function for years [96, 97], the use of battery is not always feasible – there may not be enough space inside the brain or body as a battery’s size is proportional to its lifetime [98]. We have thus seen cumbrous solutions such as placing the battery of a brain stimulator in the user’s chest or even outside the body, with wires running between the battery and the stimulator. Battery replacement, on the other hand, is risky as it usually requires a surgery that may introduce extra complications [99, 100].

Wireless charging has received attention in recent years as a viable alternative. The concept of wireless charging, however, is not new. From early 1900s Tesla’s Wardenclyffe tower [101] to the later Air Force mission of powering an unmanned helicopter [53], wireless charging has witnessed significant breakthroughs over the past century. Today wireless charging can be simply performed on an office desk or in a car. As far as medical implants are concerned, they are primarily charged

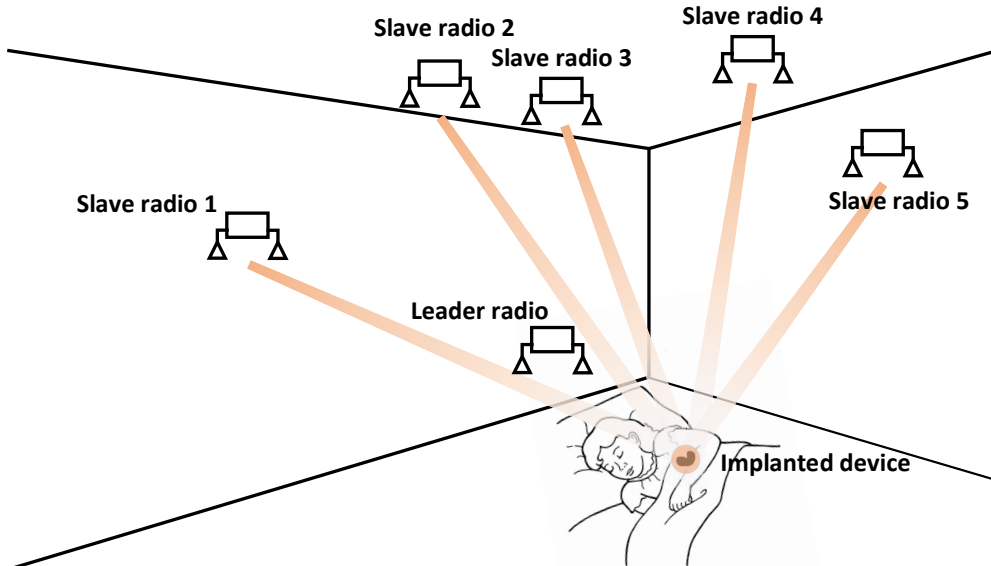


Figure 4.1: An illustration of In-N-Out deployment. The leader radio coordinates multiple slave radios to charge the pacemaker during bedtime.

through electromagnetic coupling in the near field [102, 103, 104, 105, 106]. These near-field charging systems use dedicated coils that usually require contact with human tissues. A critical drawback of these systems is that their charging efficiency drops significantly with the reduction of coil size and the increase of coil separation, which severely hinders the miniaturization of medical implants [9]. Another drawback of these near-field systems is the low flexibility: the users are required to wear bulky transmitter coils and carefully align them with the implant coils [107]. Even though the user can stay static for hours, the inter-coil coupling can be easily broken as the implant coils may move as blood flows [108]. Thus, a contactless means of wireless charging holds appeal as a flexible and less invasive alternative.

This work presents In-N-Out, a flexible far field power transfer system that owns two desirable properties: 1) it does not require the user to wear cumbersome charging devices. 2) it can continuously charge the medical implant residing in deep tissues with consistently near-optimal power, even when the implant moves around inside the human body. To do so, In-N-Out leverages *beamforming* to

combine signals coherently at the medical implant. At the heart of beamforming is the accurate measurement of channel state information (CSI) of each wireless channel. This is usually achieved by having the transmitter send a preamble, where the receiver (*e.g.*, a medical implant) uses this preamble to estimate the CSI of the forward channel. This CSI value is then fed back for transmitter beamforming.

However, CSI measurement becomes very challenging, if at all possible, for medical implants. RF signal generation is power hungry, which becomes especially challenging for medical implants that are deeply power constrained [9]. In practice, to minimize power consumption, the RF radio of a medical implant typically adopts a rather low power amplification coefficient [10]. Therefore, the resulting preamble signals are very weak, which are made even worse by the fast decaying radiation efficiency of an in-body antenna. The antenna's radiation efficiency decays significantly due to its miniature size, *i.e.*, 10 – 20 dB loss compared to the weak transmission signals [11, 12]. Furthermore, RF signals experience exponentially more attenuation in human tissues than in air, *e.g.*, 40 dB loss over just a few centimeters in muscles [13]. As a result, the received signal is usually well below the noise floor, hence the failure to provide accurate CSI estimation.

To solve these challenges, the state-of-the-art, IVN [8], proposes to encode the frequency of multiple transmission signals in hopes of these frequency-varying signals coherently combine at the medical implant from time to time, without CSI measurements. IVN achieves high beamforming power intermittently to cold start the medical implant. It is, however, ill-suited for power transfer as the beamforming power it actually produces, for most of the time, is far less than the *maximal* beamforming power.¹ The coherent-incoherent beamforming nature renders the power delivery particularly inefficient.

¹Defined as the power level measured at the target location when all wireless transmissions are coherently combined.

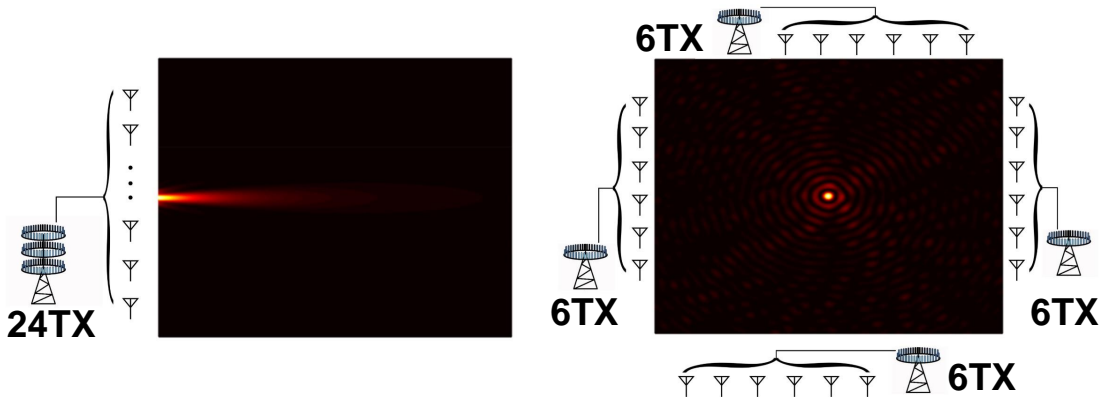


Figure 4.2: The energy heatmap produced by (left) a linear 24-antenna array and (right) a distributed 24-antenna array. The linear antenna array produces an energy beam spreading in the direction of the target, while the distributed antenna array produces an energy spot surrounding the target.

In In-N-Out, we devise a coherent beamforming algorithm that can continuously achieve the maximal beamforming power at the medical implant, even when the implant moves around inside the human body. Our algorithm builds upon the iterative one-bit phase alignment approach proposed in [79, 22], which involves the receiver sending a feedback signal to describe the received beamforming power change after each iteration until reaching the maximal. Though this approach can accomplish consistently coherent beamforming, it cannot be directly adopted in our setting because frequently measuring beamforming power and sending feedback signals would even consume more power than what can be wirelessly harvested at the implant. Thus, leveraging the one-bit phase alignment approach as a generic framework, we take into consideration the unique challenges in our scenario and design a backscatter assisted beamforming (in short, BAB) scheme. Our BAB scheme employs a customized monotonic *backscatter* radio at the implant that simply reflects signals and another nearby auxiliary radio that assesses the received backscatter signal power change. In this way we successfully offload power-consuming operations at the medical implant (*e.g.*, power assessment, signal generation and transmission) to the auxiliary radio outside human

body, and thus significantly cut down the energy consumption compared to existing systems where implant radios have to directly assess the received power change and produce feedback signals.

However, new challenges arise when we use backscatter radios at the implants. After going through excessive channel fading in both directions, the received backscatter signal is usually well below the noise floor, hence causing the new challenge of detecting/decoding the weak backscatter signal. **In-N-Out** addresses this challenge by pre-coding the carrier signal using chirp spreading spectrum (CSS) modulation. The frequency-domain processing gain of CSS enables **In-N-Out** to detect the backscatter signal even 35dB² below the noise floor.

We prototype **In-N-Out** on 21 USRP software defined radios and evaluate its performance in various settings. In our prototype, we adopt distributed antenna layout that addresses the safety concerns of wireless charging. Performing beamforming using co-located antennas will generate a high energy beam along a specific angle, as shown in Figure 2(left). This high energy beam does not only cover the medical implant but also part of the human body, likely resulting in excessive heating of human tissues. In contrast, beamforming with distributed antennas produces a tiny energy spot surrounding the target location as shown in Figure 2(right) and the energy density at other locations is significantly lower due to destructive interference [69, 109, 110, 111]. Therefore, it naturally avoids overheating other areas of the body while charging the target. Moreover, these distributed antennas have different orientations and are thus insensitive to the orientation of the implant.

Our field studies show that **In-N-Out**'s beamforming algorithm is efficient (just 0.3 s latency) and reliable (insensitive to the implant's rotation and motion). It achieves 0.37 mW charging power on average when the implant is 2 m away,

²In-N-Out does not need to decode the packet but detect the power change of backscatter signals.

which is sufficient to power a range of medical devices from outside the body. Our head-to-head comparison with IVN [8] shows that **In-N-Out** achieves $5.4\times\text{--}18.1\times$ and $5.3\times\text{--}7.4\times$ average power gain over IVN in stationary and low-speed mobile scenarios, respectively.

In-N-Out's contributions include:

- Designing a software-hardware solution for deep tissue power transfer. We devise a set of signal processing algorithms and a low-power, monotonic backscatter radio that enables **In-N-Out** to charge the medical implant at the maximal beamforming power, even when the implant moves around inside the human body. Our system consists of several technical innovations, including backscatter-leader-slave three-party beamforming without explicit CSI measurement, two-phase leader-slave chirp synchronization design, radio cold start through intentionally imperfect phase alignment, *etc.*
- Prototyping the system on software-defined radios and a PCB board, and conducting comprehensive evaluation of the system. Our evaluation takes into consideration the impact of important parameters such as the charging medium, system size, chirp bandwidth, antenna array size, *etc.* We also conduct head-to-head comparisons with the state-of-the-art approach in a range of settings.

In the next section (§4.2), we introduce the scope of our work. The system design is detailed in Section 4.4. An implementation (§4.5) and performance evaluation (§4.6) then follow. Section 4.7 summarizes related works. We discuss future works in Section 4.8 and conclude the work in Section 4.9.

4.2 Scope

This work aims to developing a practical wireless charging system, with the hope of extending the lifetime of medical implants.

The lifetime of a medical implant depends mainly on the lifetime of its battery [112]. Hence a lot of efforts have been made to improve the battery life [113], either by increasing the battery capacity or minimizing the device power consumption. Today state-of-the-art pacemakers can last for over ten years [114]. However, the user still needs a surgery for replacement when the battery is depleted. To lengthen the implant’s lifetime, **In-N-Out** can serve as a supplementary power supply – whenever the user stays in a space where a personalized **In-N-Out** system is available, the implant can be charged, without drawing power from the regular battery. As a result, the lifetime of the implant can be significantly extended.

We note that though **In-N-Out** is primarily designed for wireless power transfer, its application scope can be much broader. For example, **In-N-Out** could potentially serve as a communication system to collect the biomedical data from inbody sensors [115, 116]. Compared with conventional gastroscopy that requires the patient to swallow a tube for data collection [117], our solution is much less invasive.

Possible Deployment Scenarios: We envision the **In-N-Out** system will be deployed in the user’s personal space (home and/or office). Given a typical bedroom ($4 \times 4 \text{ m}^2$ rectangular area with a 2.8 m average target-antenna distance), if we keep the number of radios to a reasonable number, i.e., less than 14 (each emitting 30 dBm signals), then the resulting power density at any location in the room is well below the power limit specified by FCC regulation (0.6 mw/cm^2 [64]).

4.3 Beamforming Without CSI Feedback

Due to excessive channel fading and inhomogeneous channel propagation in deep tissues, CSI measurement becomes very challenging, if at all possible, for medical

implants embedded in deep tissues (will be explained in §4.4). Instead of pursuing a precise CSI measurement, we employ a non-CSI beamforming approach proposed in [79, 22], referred as one-bit phase alignment algorithm.

Algorithm overview

. The one-bit phase alignment algorithm goes through multiple rounds and then converges to the optimal phase settings. In each round, each transmitter updates the phase of the transmission signal based on the feedback sent from the receiver. The phase value in the current round is randomly selected within the range of $\pm\Phi$ with respect to the phase value in the previous round (we discuss the optimal Φ setting in §4.4.3.). Phase update can be formulated as follows:

$$\theta_i(n+1) = \begin{cases} \theta_i(n) + \delta_i(n), & \text{if } y[n] > y[n-1], -\Phi^\circ \leq \delta_i(n) \leq \Phi, \\ \theta_i(n-1) + \delta_i(n), & \text{otherwise,} \end{cases}$$

where $\theta_i(n)$ is the phase setting of the i^{th} transmitter in the n^{th} round and $y[n]$ is the received signal power in the n^{th} round.

An example

. We use a simple example scenario involving three transmitters to explain this algorithm. In the first round, each transmitter randomly chooses a phase value, as shown in Figure 4.3(a). The receiver records beamforming power. In the second round, each transmitter randomly chooses a phase that is within the range of $\pm\Phi$ from its phase value in the first round. This new phase leads to an increased beamforming power, as shown in Figure 4.3(b). The receiver notifies transmitters this power increase (\uparrow) with a single bit feedback. Hence in the third round, each transmitter uses its round two phase value as the reference and updates its phase accordingly, which unfortunately leads to a degraded beamforming power (\downarrow), shown in Figure 4.3(c). Therefore, in the fourth round, each transmitter

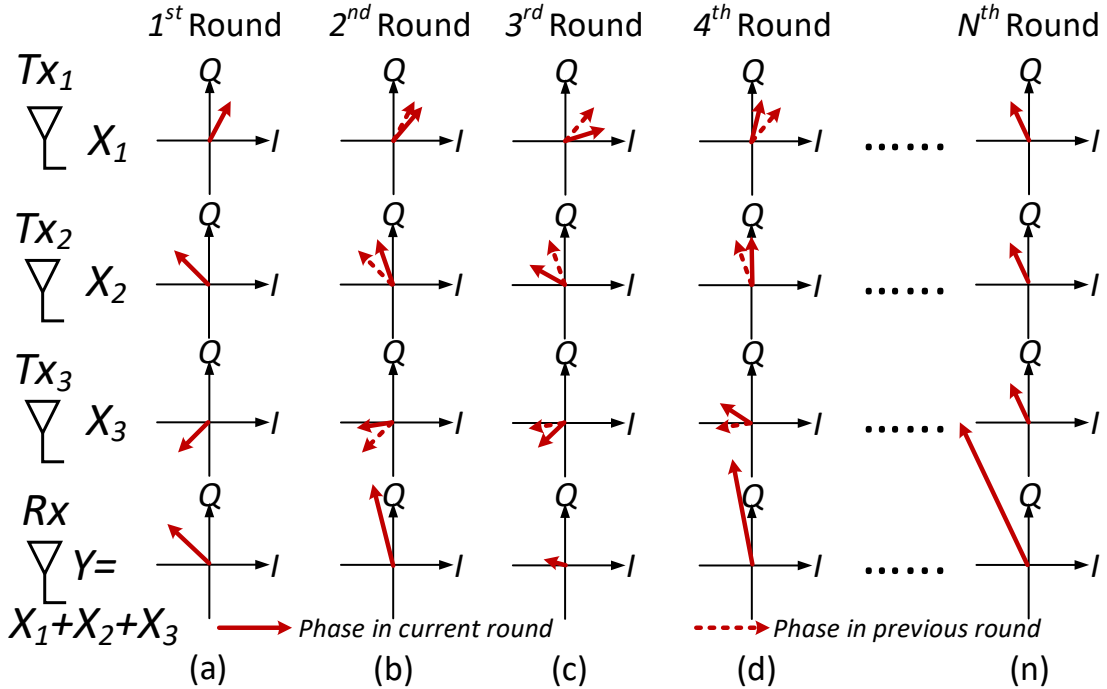


Figure 4.3: A running example of the one-bit phase alignment algorithm with three transmitters. Each transmitter adjusts its phase based on the feedback from the receiver and gradually converges to the optimal phase alignment.

again uses its round two phase value as the reference (Figure 4.3(d)). The algorithm iterates in the fashion until the beamforming power reaches its maximum (Figure 4.3(n)).

4.4 System Design

In-N-Out involves a *leader* radio and several *slave* radios working on 915 MHz ISM band,³ as shown in Figure 4.1. The leader node detects and decodes feedback signals sent from the medical implant and uses decoded information to govern the phase alignment of slaves in the next round. As the medical implant may move around while charging, we do not assume any prior knowledge of the implant's location. To minimize the energy consumption due to feedback signal creation and

³Working on 2.4 Ghz or 5 Ghz ISM band may introduce severe interference to ongoing Wi-Fi traffic, whereas working on lower ISM band (*i.e.* 433 MHz) requires a bulky receiving antenna which is not suited for implant devices.

Tx power (dBm)	Air path loss dist. (1 – 10m) [dBm]	Skin reflection /absorption (dBm)	Muscle path loss dist. (2 – 6cm) [dBm]	Insertion loss [dBm]	Muscle path loss dist. (2 – 6cm) [dBm]	Skin reflection /absorption (dBm)	Air path loss dist. (1 – 10m) [dBm]	Rx power (dBm)
30 [64]	31.67 – 51.67 [118]	3[119]	9.2 – 27.6 [120, 121]	30 [122]	9.2 – 27.6 [120, 121]	5[119]	31.67 – 51.67 [118]	-89.74 – -166.54

Table 4.1: The power loss at different part of the round-trip path between the transmitter (outside body) and the receiver (inside body). The transmission power is set to the maximum value under FCC regulation.

transmission, we design a low-power backscatter radio that offloads the computation from the medical implant to the leader radio that is outside of the human body (§4.4.1). As a proof of concept, we use a dedicated radio (*i.e.* USRP) as the leader radio. However, we envision the leader radio can simply be a smartphone being able to talk with slave radios wirelessly (*e.g.*, through Wi-Fi).

In the rest of this section, we explain the details of each design component, including carrier signal design and synchronization (§4.4), low-power backscatter radio design (§4.4.1), and power change inference algorithm (§4.4.1). Finally, we explain the way to bootstrap the system during the cold start in §4.4.2 and discuss the way to balance beamforming convergence and delay in §4.4.3.

Carrier Signal

Backscatter radio neither generates carrier signals nor amplifies transmission signals. It instead modulates data on top of the ambient carrier signal (a sinusoidal tone coming from a nearby active radio) and reflects the modulated signal (termed as backscatter signal) back to the receiver. Compared with the active radio, the backscatter radio saves three to four orders of magnitude transmission power by avoiding power consumption on carrier generator and power amplifier [123]. However, the lack of power amplifier renders the backscatter signal extremely weak, which is then made much worse by the excessive fading in deep tissues. Table 4.1 shows the break-down signal attenuation as the carrier signal goes through the human body and reflected by the backscatter radio. The receiving power is around -128 dBm on average, well below the ambient RF noise floor measured by an

USRP N210 in the same frequency band.⁴ Hence, both CSI and RSS measurement are unreliable for channel estimation (CSI measurement at 915MHz band requires at least 6 dB higher signal strength than RSS measurement [124]).

An intuitive approach is to have the backscatter radio leverage more advanced coding mechanisms to improve the signal to noise ratio (SNR) of the backscatter signal. However, this requires more complicated, power hungry analog-to-digital (ADC) and digital circuits and will again complicate the implant radio design and boost the overall energy consumption.

4.4.1 Backscatter Assisted Beamforming (BAB)

Directly applying one-bit phase alignment algorithm to in-body wireless charging is unfeasible due to its excessive energy overhead. Generating a feedback signal with even the simplest modulation scheme (*i.e.* frequency shift keying (FSK)) costs at least tens of milliwatts [125], which can quickly add up when we go through each iteration. This operation alone would consume more power than what can be wirelessly delivered to the implant. To address this dilemma, we replace the default active radio on the medical implant with a low-power backscatter radio. A backscatter radio, while being able to minimize the implant’s power consumption, raises new challenges and complicates the system design nonetheless. Below we discuss these challenges in detail as well as our solutions.

To minimize the power consumption of the backscatter radio, we offload most of its operations to the radios outside the human body. Taking a step further, we adopt chirp spread spectrum (CSS) – a chirp pulse modulation that linearly sweeps a frequency band to generate the carrier signal – to further cut down the power consumption. Compared with conventional sinusoidal tone, CSS enables the wireless signal to be decodable below the noise floor (*e.g.*, -137dBm for

⁴-70 dBm on 915 MHz frequency band measured in an office building.

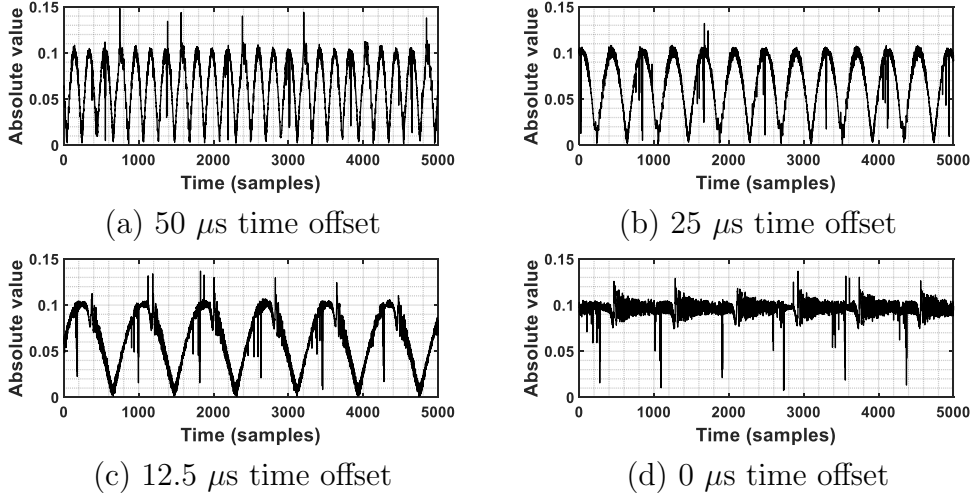


Figure 4.4: RSS measurements in different time offset settings. A larger time offset leads to a higher RSS fluctuation rate. The RSS converges to a relatively stable value when all chirps are tightly time synchronized.

LoRa [126]) by introducing the unique processing gain on the frequency domain. Given a fixed transmission power, the processing gain (PG) is proportional to the product of the chirp symbol time S_t and the bandwidth S_{bw} : $PG \propto S_t \times S_{bw}$ [127]. We can thus have different trade-offs between system delay and spectrum utilization in different scenarios, without hurting the signal detection accuracy. In the following examples, we set the chirp bandwidth and symbol time to 40 KHz and 4 ms. We have also explored other settings in our evaluation (§4.6.1).

Chirp synchronization: Tight time synchronization of chirp signals is the key to the success of beamforming. Otherwise the beamforming power will fluctuate drastically due to the periodical coherent and incoherent signal combinations. We design a *two-step chirp synchronization algorithm* for this purpose. In the first step, the leader radio broadcasts a chirp preamble. The slave radio synchronizes with this preamble through cross-correlation. The resulting lag then translates into a sample offset between the reference chirp and the received chirp preamble. Each slave radio can thus compensate for this initial time offset. However, due to heterogeneous software and hardware processing delays among radios, residual

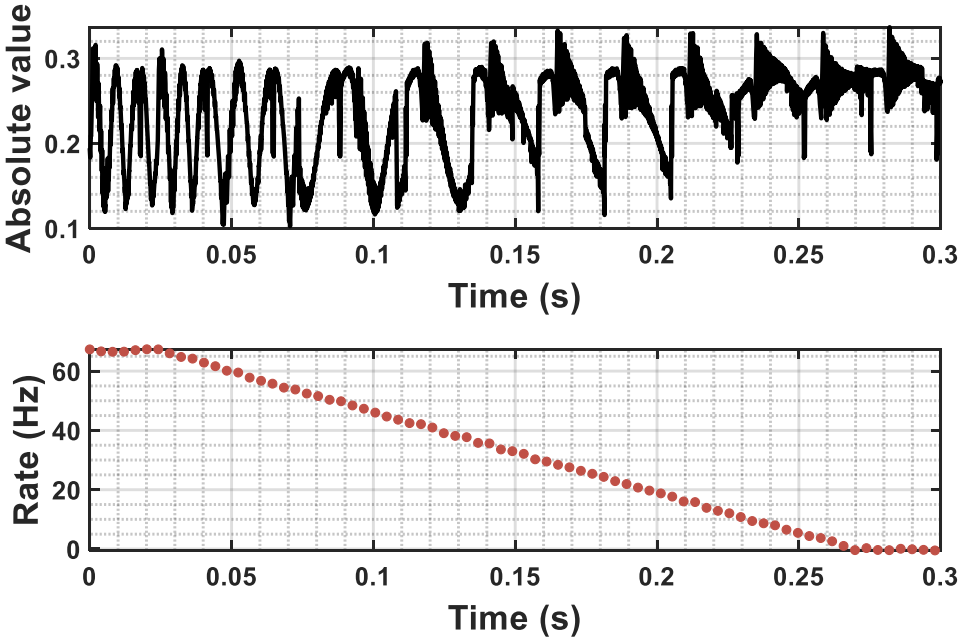


Figure 4.5: A snapshot of RSS samples (top) and the fluctuation rate (bottom) in one period. The fluctuation rate decreases with time. The signal amplitude converges when the two radios are synchronized.

time offset still remains.

In the second step, the slave radios transmit a continuous chirp signal; the leader radio listens. All slave radios then take turns to compensate for the residual time offset under the guidance of the leader radio. This is based on the realization that the amplitude of the superimposed signal (at the leader radio) will fluctuate periodically if the incoming chirps are not tightly time synchronized. In fact, the larger the time offset, the faster the received signal amplitude fluctuates, as shown in Figure 4.4. The leader radio computes the fluctuation rate of the received signal amplitude using fast Fourier transform (FFT) and then guides slave radios to compensate for the residual time offset.

The second step goes through a total of $N - 1$ periods. In each period i , In-N-Out aligns the initial time of the $i + 1^{th}$ slave to the first slave. Specifically, in the first period, two slave radios S_1 and S_2 send a continuous chirp signal simultaneously. These two signals add up at the leader radio. Since S_1 and S_2

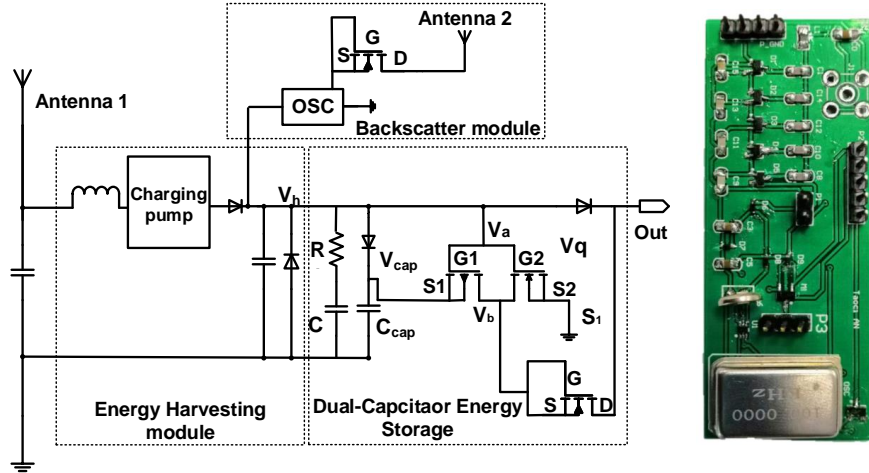


Figure 4.6: Our monotonic backscatter radio design (left) and the PCB board prototype (right). We envision the board size can be reduced to the sub-centimeter scale when implementing In-N-Out on an Integrated Circuit (IC).

are not strictly time synchronized, we will see fluctuations of the received signal at the leader radio. The leader then sends a two-bit feedback to S_2 , telling this node to add or subtract one sample time, or to stop. S_2 calibrates its clock based on this feedback, and then regenerate a chirp signal with an updated clock. The leader radio detects the change of the fluctuation rate and sends an updated feedback to S_2 . The algorithm iterates as above until all slave radios are synchronized. The algorithm then enters the next period and involves one more slave radio. All slaves are tightly time synchronized at the end of the last period.

Considering its iterative nature, one may fear our synchronization algorithm may cause an excessively long delay. However, the first step of the algorithm can already yield small residual time offset and usually a reasonable number of iterations (tens) are needed in each period. Figure 4.5 shows the variation of received signals (top) and the fluctuation rate (bottom) in one period. The fluctuation rate drops to almost zero in 0.27 s.

Backscatter Design

The chirp modulation enables the leader radio to detect the weak backscatter signal. However, generating this backscatter signal requires the backscatter radio to measure the received power and compare it with the signal power measured in previous round. These operations require extra hardware, computation and more importantly, power consumption.

To solve this challenge, we offload power measurement from the backscatter radio to the leader radio outside human body. We choose this design based on the key observation of the monotonic backscatter system: the backscatter signal power changes monotonically with the received beamforming power. By observing the power change of the received backscatter signals, the leader radio could infer the power change of the received beamforming power.

In **In-N-Out**, the backscatter radio shifts the superimposed carrier signal to another frequency band (for interference avoidance) and reflects it directly back to the leader radio. This is achieved by letting the backscatter radio generate a baseband signal at frequency f_s and mix this baseband with the superimposed carrier signal at frequency f_1 . The mixer operation will shift this superimposed carrier signal to another two frequency bands: $f_1 + f_s$ and $f_1 - f_s$. The leader radio detects the backscatter signal on one of these two frequency bands and infers the beamforming power change accordingly. Following the iterative beamforming algorithm introduced in §4.3, the leader radio then guides slave radios to adjust their signal phase settings. To avoid interference between the carrier signal and the backscatter signal, we conservatively set f_s to 100 KHz, which is 1.5× larger than the default chirp bandwidth (40 KHz).

Radio hardware design: Conventional backscatter design (*e.g.*, RFID), however, is not always monotonic, as shown in Figure 4.7(top). This non-monotonic

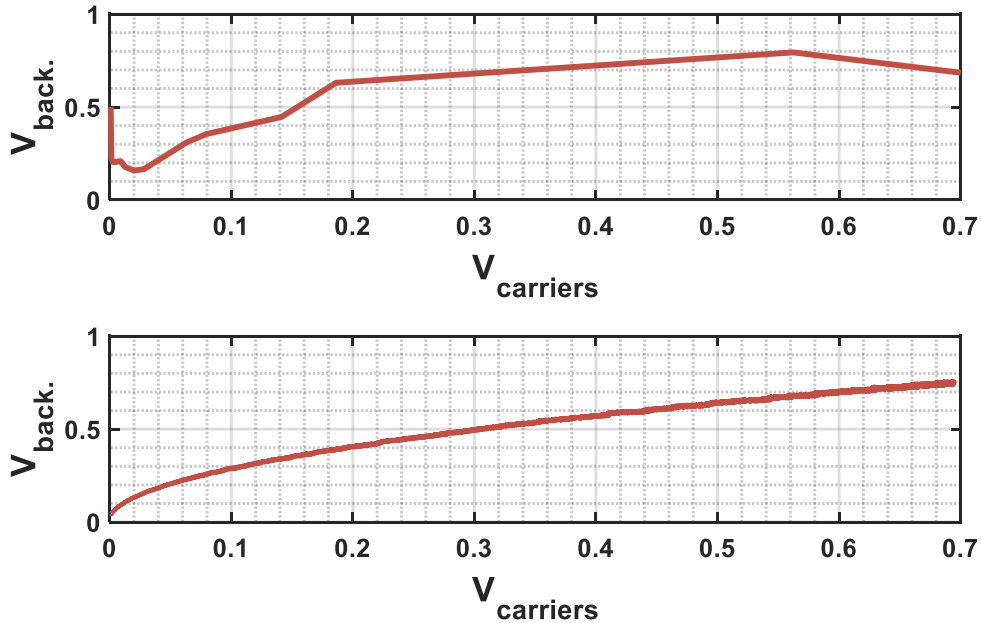


Figure 4.7: Non-monotonic (top, passive RFID [1]) and monotonic backscatter radio (bottom, In-N-Out). The top figure is adapted from [1].

property arises from the energy harvesting circuit where the impedance of matching network changes with input RF power.

To this end we design a low-power, monotonic backscatter radio. The hardware schematic is shown in Figure 4.6. Our backscatter radio contains two RF chains, one for energy harvesting (through antenna one) and another for backscatter (through antenna two). It allows the energy harvesting and backscatter to operate in parallel, without interfering each other. To achieve a consistent impedance, the RF power on the backscatter radio should be relatively stable. Hence we put a diode in-between these two modules, which allows the electric current to pass through in one direction (from the bacskcatter module to the energy harvesting module), while block it in the opposite direction. We measure the backscatter signal power as we gradually increase the carrier signal power. The result is shown in Figure 4.7. We observe that the backscatter signal power changes monotonically with the carrier signal, which confirms the effectiveness of

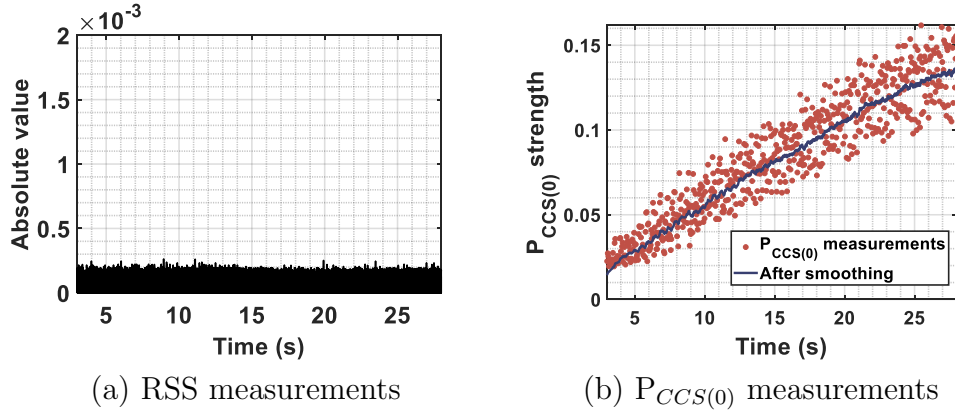


Figure 4.8: (a) RSS and (b) $P_{CCS(0)}$ measurements of the received backscatter signal as the carrier signal power grows linearly.

the hardware design. The dynamic power consumption of this backscatter radio is $42 \mu\text{W}$, which takes up only around 12% of the energy harvested from our testbed (0.37 mW).

Beamforming Power Change Inference

The leader radio infers the power change of the beamforming signal by observing the power change of the received backscatter signal. A new challenge arises due to the extremely weak backscatter signal – after going through considerable channel fading, the backscatter signal is usually below the minimum detectable strength (MDS) of the commercial RF radios (*e.g.*, around -75 dBm for an USRP N210 software defined radio [128]). To verify this challenge, we put a backscatter radio into a 10 cm thick pork belly and conduct the following experiment. A transmitter node that is five meters away sends a continuous chirp pulse, with its power grows linearly from 0 to 20 dBm. A receiver node that is one meter away from the backscatter radio measures the received backscatter signal. Figure 4.8(a) plots the amplitude of the received backscatter signal. We observe noisy power measurements which fail to reflect the power change of the backscatter signal.

We define a new metric called $P_{CCS(\omega)}$ and use it to infer the power change of

the backscatter signal. $P_{CCS(\omega)}$ is computed by correlating the received backscatter signal with the reference chirp in the frequency domain. We have proved that the peak value of $P_{CCS(\omega)}$, namely, $P_{CCS(0)}$, changes monotonically with the power change of the backscatter signal, and demonstrated that $P_{CCS(0)}$ has sufficient resolution to reflect the power change of the backscatter signal. We detail the mathematical proof in Appendix 4.10.1.

Figure 4.8(b) shows $P_{CCS(0)}$ samples extracted from the received signals. We observe an increasing trend of $P_{CCS(0)}$ as we increase the power of carrier signal. However, due to signal noises and measurement errors, $P_{CCS(0)}$ fluctuates drastically, which may confuse the leader radio and introduce extra beamforming iterations. To solve this problem, we adopt an adaptive Kalman filter [129] to smooth the $P_{CCS(0)}$ samples. Figure 4.8(b) shows that the filtered samples can fairly reflect the power change of the backscatter signal.

4.4.2 Cold Start

Previous sections focus on how to beamform towards the backscatter radio that is already awake. In this section, we describe how we bootstrap the backscatter radio during the cold start period. Cold start is a “chicken-n-egg” problem: without enough power (-20 dBm at least [130]) the backscatter radio cannot wake up to provide feedback (by simply reflecting the signal). On the other hand, without the feedback, we cannot beamform to provide energy. Exhaustively searching all the beamforming space in hope of accidentally waking up the backscatter radio is obviously not a viable approach. Employing PushID [131] to wake up the backscatter radio, on the other hand, requires a much stronger carrier signal to compensate the excessive channel fading inside the human body, which may overheating human tissues and cause safety issues.

We propose a beamforming-based space searching algorithm to bootstrap the backscatter radio. Recall that the leader node can be a mobile phone or a wearable

device worn by the user, it is thus reasonable to assume the leader node is close to the medical implant. In **In-N-Out**, we first align all beams towards the leader node and then search the limited space around the leader node. The space searching algorithm is based on the realization that different phase combining can lead to a significant different beamforming patterns. Specifically, let ϕ_i be the current phase setting of the slave radio i . As we introduce a phase perturbation δ_ϕ to ϕ_i , the carrier signals will coherently combine at other locations, resulting in side lobes. This new phase combination also spreads the main beamforming lobe over a larger area, as shown in Figure 4.9(b). Accordingly, by introducing different phase perturbation δ_ϕ ($-\sigma < \delta_\phi < \sigma$) to each slave radio, we can produce different beamforming patterns and use them for space searching. When the backscatter radio gains enough energy as a result of this searching effort, it wakes up and starts to backscatter. Once the leader radio receives this bacskcatter signal, it goes back to serve its functions described in §4.4 and §4.4.1.

As the beamforming power spreads over the main lobe and side lobes, the question here is whether these lobes are strong enough to wake up the backscatter radio. To answer this question, we measure the power distribution of the beams shown in Figure 4.9(b)–(d) and find a 3.6 dB power drop with repesect to the optimal beamforming power (Figure 4.9(a)). Note that to achieve a desirable charging efficiency, the optimal beamforming power of a multi-antenna system is much higher than the power required in the cold start period (-15 dBm). Hence, these newly emerging beams are strong enough to wake up the backscatter radio. Our micro-benchmark result (§4.6.1) also confirms the efficacy of this cold start method.

Determining the phase perturbation range σ : We define the scanned area as the space where the received energy is higher than 30% of the optimal beamforming power (equivalent to ± 5 dB loss). We then conduct simulations to investigate the impact of the phase perturbation range σ on the scanning ratio – the ratio

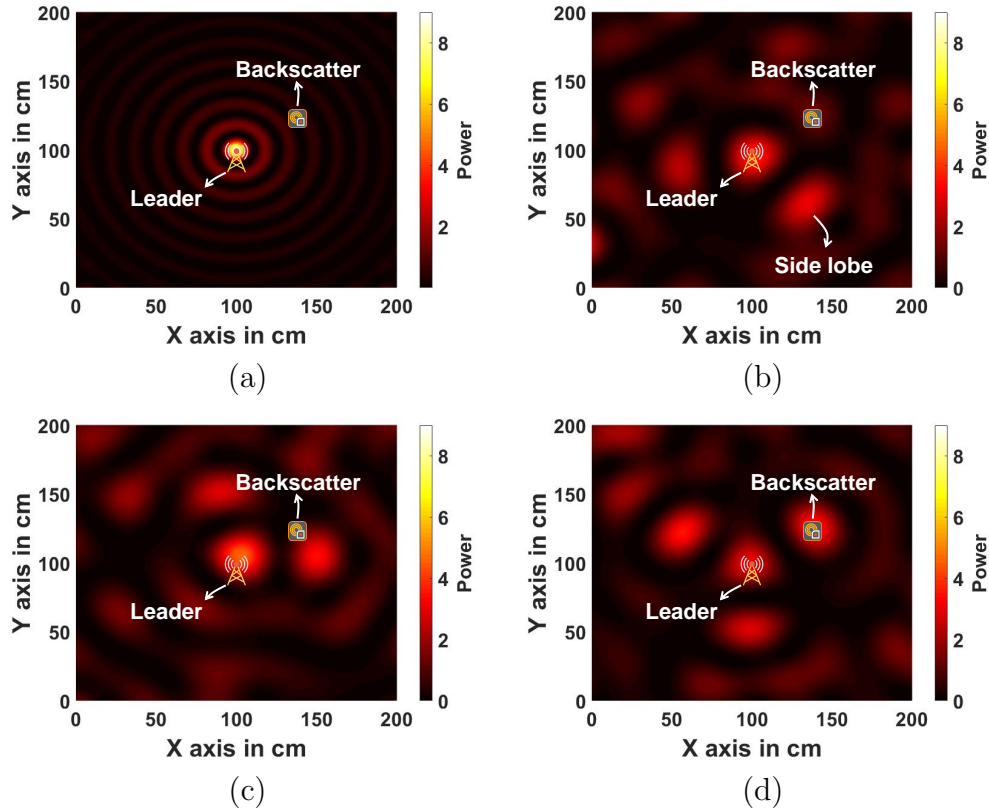


Figure 4.9: Beamforming energy patterns with different phase perturbations: (a) optimal phase alignment, (b)-(d) with different phase perturbations. With phase perturbations, we observe an enlarged main lobe and many side lobes. These side lobes can provide sufficient energy to wake up the backscatter radio.

of the scanned area to the entire searching space (a $2 \times 2 \times 2$ m³ Cube centered at the receiver). Figure 4.10(a) shows the scanning ratio as a function of phase adjustment in different σ settings. The scanning ratio grows rapidly as we increase σ from 10° to 30° and further to 60°. The growth of scanning ratio then slows down as σ increases further. To better understand this result, we further repeat the above experiment 100 times in different σ settings and show the result in Figure 4.10(b). We can see the scanning ratio peaks the maximal when $45^\circ \leq \sigma \leq 65^\circ$. Suggested by this simulation result, we set σ to 55°.

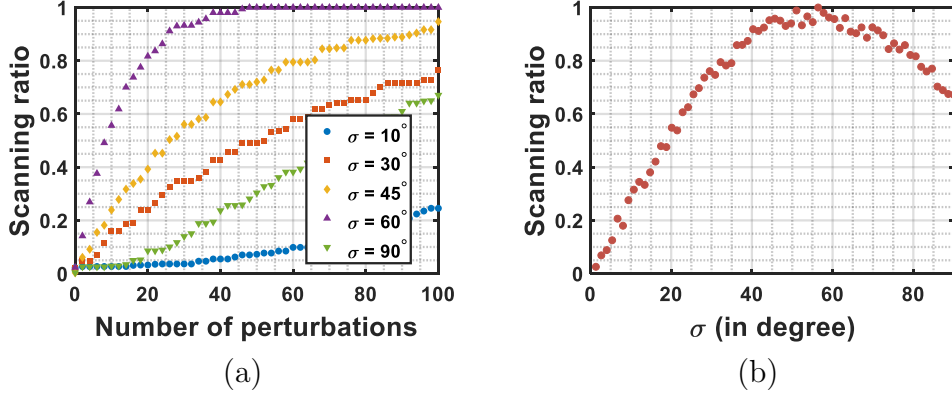


Figure 4.10: Phase perturbation range σ analysis (a) Scanning ratio CDF vs. number of perturbations. (b) Scanning ratio values after 100 perturbations vs. σ .

4.4.3 Balancing Convergence and Delay

In our iterative beamforming algorithm, the phase searching bound Φ is critical to system performance (Φ is introduced in §4.3). If Φ is too large, the algorithm may rapidly converge to a non-optimal beamforming result. In contrast, a smaller Φ will lead to better beamforming results, but with a longer delay. In **In-N-Out**, we use a larger phase bound at the beginning of the algorithm and then a smaller value as the algorithm iterates. We compute a suitable phase searching bound in each iteration based on a high order polynomial function $\Phi = P(n)$, where n is the iteration index. We detail this polynomial function and its derivation in Appendix 4.10.2.

4.5 Implementation

We describe the system implementation in this section.

4.5.1 Testbed Setup

We deploy 17 USRP N210 and four USRP B210 software defined radios on the ceiling of an office building, as illustrated in Figure 4.11. Each USRP is equipped

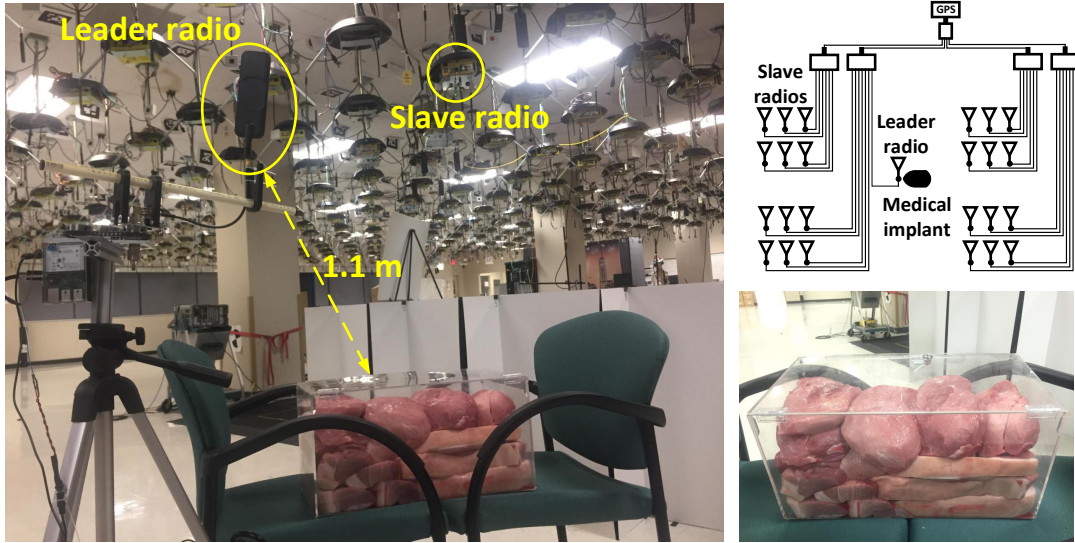


Figure 4.11: Testbed setup. Our testbed consists of 17 USRP N210 and four USRP B210 nodes, all mounted on the ceiling of an office building.

with a WBX RF daughter board [132] and works on FDD full duplex mode. We use a Mini-Circuits ZFL-1000VH RF amplifier [133] to boost the signal power and send out the amplified signal through a 4 dBi Taoglas TG.35.8113 antenna [134]. As USRP only supports relative signal power measurement [90], we conduct a one-time power calibration using an Agilent E4405B spectrum analyzer [135] to acquire the absolute signal power.

USRP Synchronization: To mitigate the clock drift and carrier frequency offset (CFO), all USRPs are wired to an Octoclock-G GPS disciplined oscillator (GPS-SDO) [136] with 10MHz reference signal. This centralized time synchronization method provides an accurate timing reference. Wireless-based time synchronization methods such as [137, 138] can be further employed for an even larger system deployment.

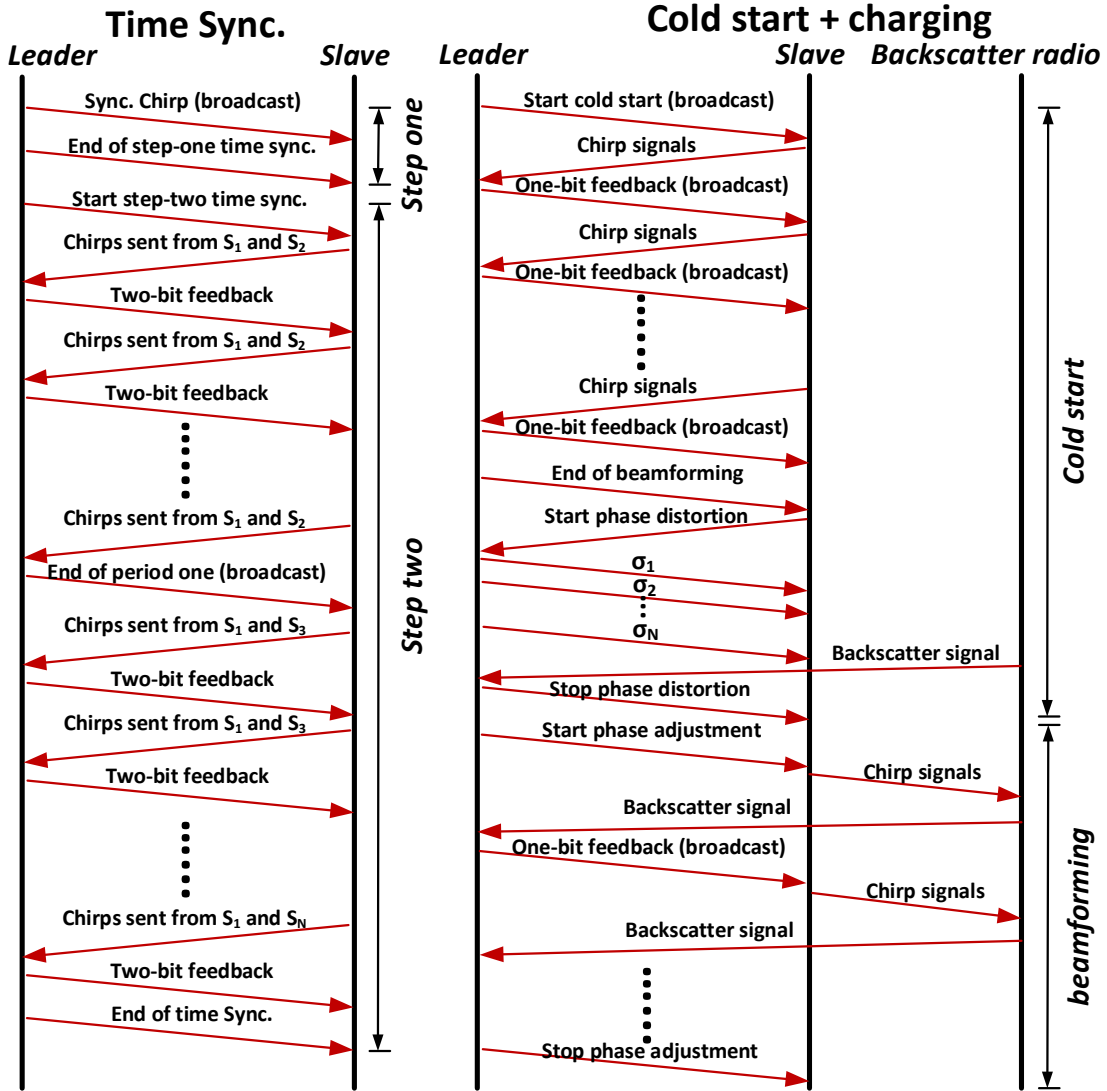


Figure 4.12: Message flow of In-N-Out.

4.5.2 Software Implementation

We implement all signal processing modules in C++ (version 4.8.4) with UHD driver V3.10.1 and GNU Radio Companion V3.7.6.1. Figure 4.12 shows the message flow of these signal processing modules. We next describe the module implementation on the leader radio and the slave radio.

Leader radio has three modules: chirp signal synchronization, backscatter radio cold start, and beamforming orchestration. We implement the following signal processing functions to support the above three modules: chirp preamble

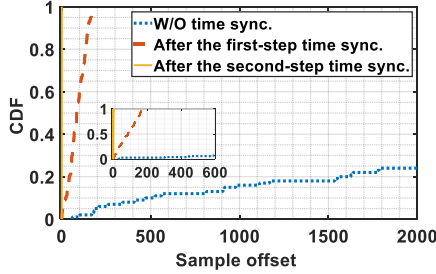


Figure 4.13: CDF of residual time offset without and with chirp synchronization.

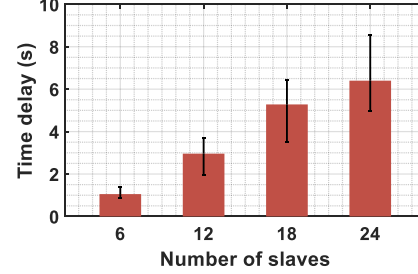


Figure 4.14: Chirp synchronization delay vs. number of slave radios.

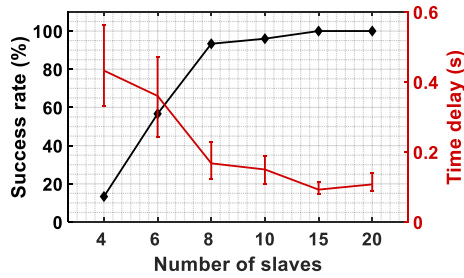


Figure 4.15: Cold start success rate (left) and delay (right) vs. number of slave radios.

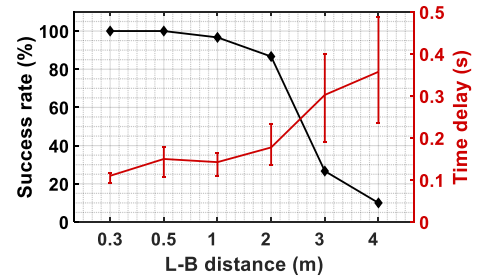


Figure 4.16: Cold start success rate (left) and delay (right) vs. L–B distance.

generation and transmission, RSS fluctuation detection, two-bit feedback signal generation and transmission, backscatter signal detection, $P_{CCS(0)}$ calculation, smoothing, and comparison.

Slave radios participate in all the three modules mentioned above. We implement the following signal processing functions on each slave radio: chirp preamble detection, two-bit feedback signal detection and decoding, time calibration, beamforming signal detection, random number generator, phase adjustment, chirp carrier generation, and transmission.

4.5.3 RF Power Limit

Exposure to high levels of RF radiation can be harmful.

Transmission power: According to Federal Communications Commission (FCC)

regulation, the transmission power of a single radio (with a 4 dBi antenna gain) should be below 32 dBm [139]. In our deployment, the maximum transmission power is 30 dBm and thus complies with the FCC regulation.

Power density in space: FCC and Food and Drug Administration (FDA) have different regulations for power density. Specifically, FCC requires the power density in ISM band to be below 0.6 mW/cm^2 [64], whereas FDA requires the power density to be below 10 mW/cm^2 [140]. In our testbed, 24 antennas are distributed on the ceiling of an $18 \times 18 \text{ m}^2$ office building. The theoretically maximal power density at the receiver is 0.08 mW/cm^2 based on [141], which satisfies both FCC and FDA requirements. In our experiments, we also measure the beamforming power at different locations across the room. The maximum measured power density is 0.05 mW/cm^2 , well below the power limits specified by FCC and FDA. In practical deployments, we only need to compute/measure the power density at the receiver (target location) and make sure this value is below the safety limit because in distributed antenna system the power density at the target location is proved significantly higher than other

4.6 Evaluation

We present the evaluation results in this section. By default the chirp bandwidth and symbol time are set as 40 KHz and 4 ms (8192 samples), unless otherwise noted (when we investigate their impact on the system performance).

4.6.1 Micro-benchmark

We start with performing micro-benchmarks to evaluate the effectiveness of each function module in In-N-Out.

Chirp Synchronization

Experiments in this section aim to i) evaluate the overall performance of the two-step chirp synchronization algorithm, and ii) understand the relationship between synchronization delay and number of slave radios.

i). **The accuracy of chirp synchronization algorithm:** We synchronize chirp signals from all 24 slave radios using the two-step chirp synchronization algorithm. We repeat this experiment 100 times and plot the CDF of the residual time offsets before and after applying our algorithm in Figure 4.13. Without chirp synchronization, the median and maximum time offsets are 3630 and 8182 samples, respectively. These two values drop to around 86 and 168 samples after the first-step chirp synchronization, and 0.4 and 0.9 sample after the second-step chirp synchronization. The trend clearly demonstrates that our chirp synchronization algorithm can effectively calibrate out the initial time offset among radios.

ii). **Synchronization delay vs. slave count:** We then evaluate the chirp synchronization delay (termed as delay) under a different number of slave radios. We repeat this experiment 100 times in each setting and plot the results in Figure 4.14. We observe the delay increases with the number of slave radios. Specifically, the delay is below 1.4 s when we have six slave radios, 2.9 s for 12 slaves, 5.3 s for 18 slaves, and 6.4 s for 24 slaves. Please note that our chirp synchronization needs to run only once, and the one-time delay of 6.4 s would not have a noticeable effect on the user experience.

Cold Start

Experiments in this section aim to evaluate the cold start success rate and delay when we vary i) number of slave radios and ii) distance between the leader and the backscatter (termed as L-B distance).

i). **Success rate and delay vs. slave count:** In these experiments, we insert a

backscatter radio into a 10 cm-thick pork belly and cold start it using a different number of slave radios. The leader radio is half a meter away from this pork belly. We perform this experiment 100 times in each setting and plot the success rate and delay in Figure 4.15. We observe the success rate is low when we use only four slave radios. This is as expected since beamforming power of four slave radios is too low. The success rate soon jumps to 90% as we double the number of slave radios. It then approaches to 100% when the slave count is larger than 15. These results demonstrate the effectiveness of our cold start algorithm. On the other hand, we see the delay of cold start decreases as we increase the number of slave participates. The longest delay, however, is only 0.56 s. These results clearly demonstrate the effectiveness of our cold start algorithm.

ii). Success rate and delay vs. L–B distance: We then test success rate and delay of our cold start algorithm in different L–B distance settings. In these experiments, we insert a backscatter radio into a 10 cm-thick pork belly and cold start it using 10 slave radios. Results are shown in Figure 4.16. The success rate is around 100% when the leader radio is close to the backscatter radio, *e.g.*, 0.3 m and 0.5 m away. It then decreases slightly to 96.7% and further to 86.6% as we increase the L–B distance to 1 m and 2 m, respectively. We observe a significant performance degradation (from 96.7% to 26.3%) when the leader is 3 m away from the backscatter radio. This is because the searching space is too large, hence the power of side lobes is not strong enough to wake up the backscatter radio. As for cold start delay, we observe that it grows smoothly as we increase the L–B distance from 0.3 m to 2 m. It then jumps to around 0.3 s and further to 0.35 s as we place the leader radio 3 m and 4 m away from the backscatter radio, respectively. By default, the leader radio is placed less than 1 m away from the human body. This is very practical because in real life, the leader radio can simply be the smartphone carried by the target or the smartwatch on the target’s wrist. These devices are usually less than 1 m away from the implant inside the

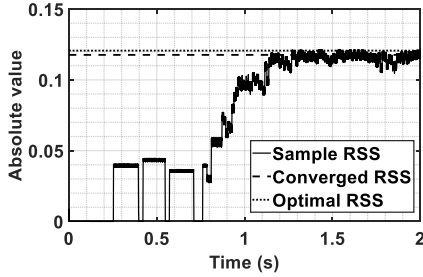


Figure 4.17: RSS during a beamforming episode.

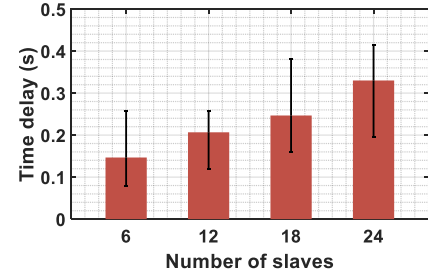


Figure 4.18: Beamforming delay vs. number of slave radios.

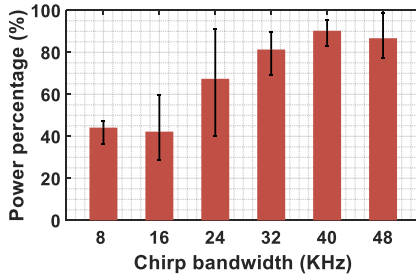


Figure 4.19: Power percentage vs. chirp bandwidth.

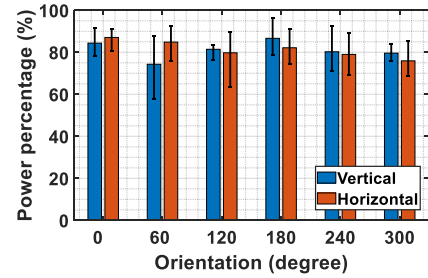


Figure 4.20: Power percentage vs. backscatter orientation.

body.

Beamforming

Experiments in this section aim to evaluate the delay and power gain of our beamforming algorithm in various parameter settings, *e.g.*, different number of slave radios and different chirp bandwidths. To measure the power gain gap between our beamforming algorithm and the optimal one, we define a new metric, namely

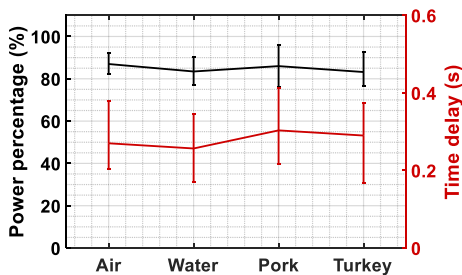


Figure 4.21: Power percentage across different media.

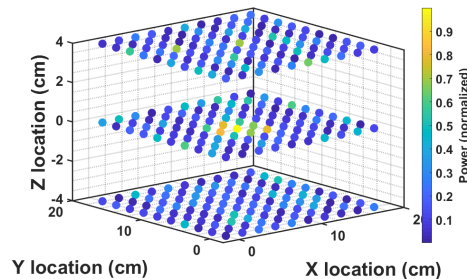


Figure 4.22: In-tissue 3D power distribution.

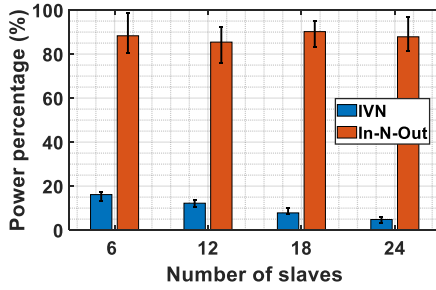


Figure 4.23: Power percentage vs. slave count.

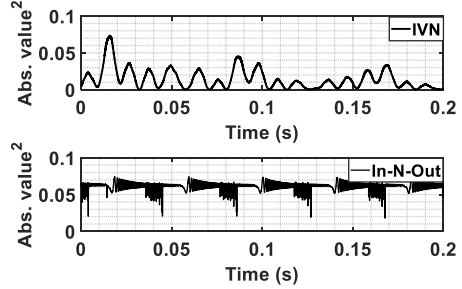


Figure 4.24: Beamforming power samples.

power percentage, as the square of the ratio between the averaged beamforming amplitude (achieved by *In-N-Out*) and the optimal beamforming amplitude. In reality, however, the optimal beamforming amplitude cannot be measured directly. We thus start each slave radio at a time and record the received signal amplitude at the backscatter radio. The summation of these signal amplitudes serves as an alternative to the optimal beamforming amplitude. We also define the *beamforming delay* as the execution time of our beamforming algorithm until the beamforming power at the backscatter radio converges.

i). **Close to optimal beamforming amplitude:** We measure the beamforming amplitude gap between our algorithm and the optimal one. In this demonstrating experiment, we run our beamforming algorithm on three slave radios. The backscatter radio is inserted into a 10 cm thick pork belly placed 2 m away from each slave radio. For a better illustration, we sequentially start these three slaves and measure their signal amplitude at the backscatter radio. Figure 4.17 shows the result. We can see the beamforming amplitude grows rapidly and converges to a large value. The convergence signal amplitude (dashed line) stays closely to the optimal beamforming amplitude (dotted line), with the average amplitude percentage of 96.5%. This result clearly demonstrates the high efficiency of the proposed beamforming algorithm.

ii). **Convergence delay vs. slave count:** Short convergence delay is crucial

to our system, especially in mobile scenarios. We next examine the impact of slave count on the resulting beamforming delay. The experiment setup follows the previous experiment. We run the beamforming algorithm 100 times in each setting and plot the delay in Figure 4.18. As we can see, the beamforming delay grows slowly as we increase the number of slave radios. Specifically, the average delay is 0.15 s, 0.21 s, 0.25 s and 0.33 s with 6, 12, 18 and 24 slave radios, respectively. Further, we observe that though the beamforming delay fluctuates from experiment to experiment, the maximum delay is less than 0.41 s. Hence, we believe that our iterative beamforming algorithm is fast enough for most of the in-body charging scenarios.

iii). Power percentage vs. chirp bandwidth: We then examine the impact of chirp bandwidth on the beamforming power percentage. Similar to previous experiments, the backscatter radio is inserted into a 15 cm thick pork belly placed 2 m away from 20 slave radios that are randomly picked from our testbed. We run the experiment 100 times in each setting and plot the achieved power percentage values in Figure 4.19. As shown, the power percentage grows as we first increase the chirp bandwidth – a higher chirp bandwidth improves the accuracy of the power inference algorithm. An accurate power inference result further improves the beamforming efficiency. Meanwhile, we observe that the power percentage increase rate decreases with the chirp bandwidth, indicating that the marginal utility of the frequency-domain processing gain decreases. Considering both trends, we set 40 KHz as the default chirp bandwidth setting.

iv). Power percentage vs. backscatter radio orientation: We further examine how the backscatter radio’s orientation affects the beamforming efficiency, which also indicates our system’s robustness against the radio placement. In these experiments, we rotate the backscatter radio (inside a 15 cm thick pork belly) horizontally and vertically from 0° to 300° and measure the power percentage at the backscatter radio. We repeat the experiment 100 times in each rotation

Device	Pacemaker	Cardiac defibrillator	neuro-stimulator	CIDR	In-N-Out
Power (μW)	10–100	25–250	40–500	100–800	372

Table 4.2: Power requirements of several commercial medical implants. In-N-Out can achieve average $372 \mu\text{W}$ by using 24 slave radios, which is sufficient to power up most of commercial pacemakers and cardiac defibrillators, as well as many neuro-stimulators and CIDRs.

angle and plot the results in Figure 4.20. We observe that In-N-Out achieves a consistently high power percentage (an average of 83.5%, minimum of 74.3% and maximum of 87.1%) in all rotation angle settings. This is because the antennas in our system are placed in a distributed fashion and thus are insensitive to the backscatter radio orientation.

v). **Sufficient power for commercial medical implants:** To examine whether the beamforming power achieved by In-N-Out is sufficient to charge commercial medical implant, we conduct a survey on the power consumption of several representative medical implants [142, 143], including pacemaker, cardiac defibrillator, neuro-stimulator, and controlled internal drug release (CIDR). For comparison, we also calculate the average beamforming power (in μW -scale) achieved by In-N-Out. Table 4.2 summarize the result. We measured $107 \mu\text{W}$ – $617 \mu\text{W}$ (average $372 \mu\text{W}$) beamforming power across the $18 \times 18 \text{ m}^2$ testbed area. The available power is higher than the power consumption of pacemakers and cardiac defibrillators, and only slightly lower than some neuro-stimulator and CIDR devices. We envision by shortening the signal prorogation path, such as deploying the system in smaller areas such as bedrooms or offices, In-N-Out would achieve a substantially higher beamforming power.

4.6.2 Field Study

We next conduct field studies to evaluate the performance of In-N-Out in different mediums. Although there are a surge of inbody wireless charging competitors, we



Figure 4.25: Experimental setup for mobile cases.

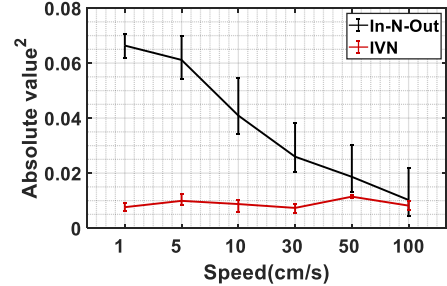


Figure 4.26: Average beamforming power vs speed.

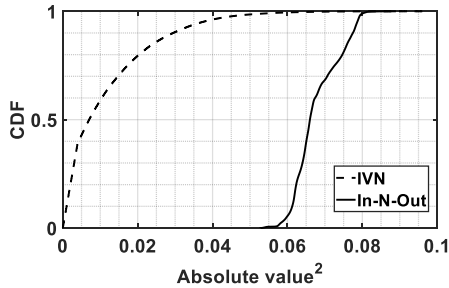


Figure 4.27: CDF of the beamforming power. ($v = 5 \text{ cm/s}$)

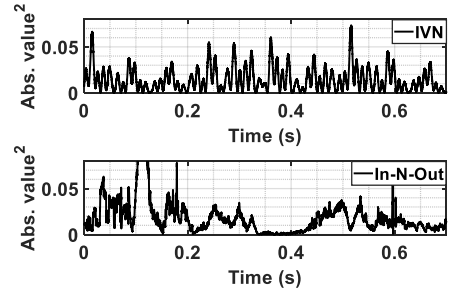


Figure 4.28: Beamforming power samples. ($v=1 \text{ m/s}$)

choose the state-of-the-art work IVN [8] for comparison as IVN shares the most similar hardware setup with In-N-Out. We carefully implement IVN and compare the performance of these two approaches in both stationary and mobile scenarios.

i). Impact of Medium: We first examine whether our system can be used in other media. In these experiments, we place the backscatter radio in four different media with significantly different channel characteristics, *i.e.*, air, water, pork and turkey. We measure the resulting power percentage and delay (excluding chirp synchronization) of our system in each setting. 24 slave radios are involved in these experiments. As shown in Figure 4.21, In-N-Out achieves the highest average power percentage in the air (86%), followed by 85% in the water, 83% in the pork belly, and finally 83% in the turkey. While the beamforming delays in these four media are slightly different, they are all below 0.41 s and would not cause noticeable delays in most of the cases. These experiment results demonstrate that

In-N-Out can be used to charge objects in various media.

ii). In-tissue Power Distribution: We then examine **In-N-Out**'s power distribution in deep tissues. The backscatter radio is placed inside a 10 cm-thick pork belly. Figure 4.22 shows the power distribution measured across three slices (with 10 cm depth) of the pork belly. The backscatter radio is placed at (8, 8, 0). We observe a clear hot spot around the backscatter radio (with a radius around 2 cm) in the 3D space where the beamforming power is the highest. The power at other locations, however, stays at a relatively low level. The average power at the hot spot is $10.3\times$ higher than the average power measured at the other locations. This result clearly demonstrates that **In-N-Out** can successfully concentrate the beamforming energy to a tiny energy spot in a non-uniform medium like pork belly.

iii). Comparison with IVN in stationary cases: We first compare the power gain of **In-N-Out** and IVN in stationary cases. In these experiments, we insert a backscatter radio into a 10 cm thick pork belly and place them on a stationary table. We then vary the number of slave radios from 6 to 24 and measure the power percentage achieved by both **In-N-Out** and IVN. The experiment setup stays the same as the setup in the previous experiment. We repeat this experiment 100 times in each setting and plot the results in Figure 4.23. As shown, **In-N-Out** achieves a consistently higher power percentage than IVN. Specifically, when we have 6 slave radios, the average power percentage achieved by **In-N-Out** is 87.32%, $5.4\times$ higher than that achieved by IVN (16.2%). When we triple the number of slave radios (18), **In-N-Out** achieves $12.8\times$ higher power percentage than IVN. This gap further increases ($18.1\times$) as we use 24 slave radios.

To better understand the performance gap, we profile the instantaneous beamforming power of these two approaches and show the result in Figure 4.24. Both IVN and **In-N-Out** can achieve high beamforming power, but IVN only achieves

high power levels at some time points. Its power level in most of the time, including the charging period, stays rather low, leading to a low average power level. In contrast, the beamforming power achieved by **In-N-Out** is rather consistent, hence a much higher average power level.

iv). Comparison with IVN in Mobile Cases: We further conduct the performance comparison in mobile cases where the charging target moves around during the charging process. In these experiments, we put a backscatter radio inside a 21 lb turkey. The turkey is then fixed on a Pioneer-p3dx robot [88] running ROS (Robot Operating System) [87]. Figure 4.25 shows the mobile experiment setup. We use 10 slave radios and measure the received power level at the backscatter radio while the robot moves around. The experiment is repeated 100 times in each speed setting. Figure 4.26 shows the average power achieved by **In-N-Out** and IVN. When the robot moves at a relatively slow speed (*e.g.*, 1 cm/s and 5 cm/s), **In-N-Out** outperforms IVN by 7.4 \times and 5.3 \times , respectively. To understand this difference, we plot the CDF of the beamforming power of these two systems when the robot moves at 5 cm/s. The result is shown in Figure 4.27. For **In-N-Out**, we find its power level stays rather consistent, with the lowest and highest power level of 0.053 and 0.089. In contrast, the power level variation of IVN is much larger, with its 90% percentile value below 0.029. This result demonstrates that **In-N-Out** is agile enough to handle the target’s slow movement. *e.g.*, moving with the blood flowing.

As we increase the speed, the performance gap between these two systems decreases. Specifically, when the robot moves at 1 m/s, the two approaches deliver similar power levels. To understand this trend, we randomly select a 0.8 s time window and measure the instantaneous beamforming power levels, as shown in Figure 4.28. The results show that at such a high speed, the power levels by both approaches vary drastically. However, we expect that lower movement speeds such as 1 cm/s and 5 cm/s are much more commonplace than speeds as

high as 1 m/s in medical implant charging scenarios. We believe In-N-Out can handle such common cases successfully.

4.7 Related Work

Our system is related to wireless charging and backscatter, while quantitatively differ from either one.

4.7.1 Wireless Charging in Bioelectronics

Wireless charging in bio-electronics can be broadly divided into three categories: near-filed inductive coupling, far-field electromagnetic radiation, and others.

Near-field inductive coupling exploits magnetic field induction effect to deliver energy between two coils [144]. Research works in this domain focus on inductive power link optimization [106, 144, 104, 145], source-load decoupling [146], and multi-coil linkage design [37, 147]. While near-field method achieves satisfying power delivery efficiency, it requires the user to wear bulky coils and align them with the implanted coil [107]. As a result, the users need to sit still for hours to have their implants fully charged. Moreover, the charging efficiency of near-field methods drops significantly with the reduction of coil size, which limits their working range to less than a centimeter [148, 10]. Hence the focus in this field has shifted towards overcoming the coil misalignment problem and improving the system robustness.

Far-field wireless charging transfers power to the target through electromagnetic radiation [149, 150, 151], microwave radiation [152], or laser [39, 153]. Compared to the near-field method, the far-field method supports wireless charging over a longer distance at the cost of lower wireless charging efficiency. Research in this field focuses on RF diode and DC impedance optimization [149], antenna optimization [150], and effective system implementation [151]. IVN [8] introduces an

opportunistic frequency-encoding method in hope of combining signals constructively at the medical implant. However, IVN’s beamforming power, for most of the time, is far below the maximum value it can potentially achieve. In contrast, **In-N-Out** aligns the phase of signals at the medical implant rapidly and keeps this coherent phase combining over the entire wireless charging period. Hence it can continuously charge the medical implant with consistently near-optimal beamforming power. The different design principle of **In-N-Out** and IVN leads to a significant gap in power delivery efficiency: **In-N-Out** achieves $5.4 - 18.1 \times$ and $5.3 - 7.4 \times$ power gain over IVN in stationary and mobile case, respectively.

In-N-Out also builds upon past works that leverage one-bit phase alignment algorithm [109, 154] for wireless charging. Energy-ball [109] adopts this algorithm to charge IoT devices where CSI is unavailable. WiFED [154] employs this algorithm to realize near optimal power transferring and communication over Wi-Fi links. However, both of these pioneer works assume the receiver has enough battery to assess the beamforming power and produce feedback signals, which is not true for the ultra-low power, energy-scarce medical implants. Besides, the excessive link budget renders the feedback signal far below the noise floor, and thus fail the feedback signal detection and decoding on the transmitter side. Accordingly, we cannot directly borrow these techniques for inbody wireless charging.

As another alternative, mid-field resonant power transfer that combines both near-field and far-field methods is proposed [155, 9, 50, 50]. While this method can work over longer distances in the free space, the working range in the human body is still constrained by the coil spacing. Although the focus of this review is on RF-based methods, there are also related works on leveraging ultrasound for power transfer [156, 157, 158, 159, 160, 161]. In [158, 157, 156], the authors demonstrate the feasibility and advantages of ultrasonic power charging for implanted devices in animal tissues and tissue mimicking materials. In [159, 160, 161], the authors proposed end-to-end ultrasonic charging and communication systems,

whereas they focus on protocol design, hardware form-factor minimization and system rechargeability. Although ultrasound-based methods achieve higher power transfer efficiency, they are still intrusive due to the requirement of placing the transmitter coil close to the receiver (*e.g.*, attach to the human skin).

4.7.2 Backscatter Communication

Backscatter systems encode information on top of the remote carrier signal for ultra-low-power communication. Recent studies on backscatter communication aim to improve the backscatter range [162, 123, 163], enhance the ubiquity [35, 34, 164, 122, 165], and enable new applications such as fine-grained localization [166, 167, 168], material identification [169, 170], and vehicle counting and localization [171]. **In-N-Out** takes advantage of the backscatter design to reduce the energy consumption of the medical implant.

There are also several works studying wireless charging on backscatter node without explicit channel measurement [1, 172]. However, these works still require CSI measurement at transmitters, which is very challenging due to the severe signal attenuation in deep tissues. **In-N-Out** addresses this challenge by precoding the carrier signal using chirp modulation and leveraging its unique processing gain in the frequency domain to improve the SNR of backscatter signals. Additionally, **In-N-Out** introduces a new metric $P_{CCS(0)}$ to replace the unreliable power measurement, and uses this metric to guide the execution of beamforming algorithm.

4.8 Discussion

In-N-Out leaves room for further investigations, as discussed below:

Reducing deployment cost: As a proof-of-concept, we implement **In-N-Out** on software-defined radios (*i.e.* USRP) for fast-prototyping. In the future we plan

to customize the RF radio design to reduce the overall system cost. Given the light-weight computation tasks and narrow band communication nature of our system, one can customize the RF radio with a MSP430 [173] MCU (\$2.09), a MAX2235 [174] power amplifier (\$2.16), a TI SN74LS624N [175] oscillator (\$3.94), two cc1100 [176] radio transceivers (\$3.65), and two W5017 [177] antennas (\$7.25), which leads to a total cost around \$25.

Scaling to multiple targets: While the system design is illustrated in the single target settings, **In-N-Out** can be easily extended to multi-user scenario by introducing a MAC layer protocol such as time duplex multiple access (TDMA) or Frequency duplex multiple access (FDMA). We leave this for our future work.

4.9 Concluding Remarks

In this work, we present the design, implementation, and evaluation of **In-N-Out**: a multi-antenna system that can continuously charge the medical implant at the near optimal beamforming power, even when the implant moves around inside the human body. To achieve this, **In-N-Out** proposes a set of novel signal processing algorithms and a low-power, monotonic backscatter radio design. We prototype **In-N-Out** on software defined radios and PCB boards. The head-to-head comparison on a multi-antenna testbed demonstrates that **In-N-Out** achieves $5.4\times$ – $18.1\times$ and $5.3\times$ – $7.4\times$ average power gain over the state-of-the-art solution in stationary and low-speed mobile scenarios, respectively. **In-N-Out** is the first step towards flexible wireless charging for medical implants. Moving forward, we will endeavor to address the following technical challenges: achieving optimal deployment of the antenna array, mitigating the impact of strong multi-path effects, charging multiple implants simultaneously, etc. We also plan to pursue subsequent clinical experiments for further validations.

4.10 Appendix

4.10.1 $P_{CCS(0)}$ extraction

Let $x(t)$, $X(\omega)$, $p(t)$, $P(\omega)$, $n(t)$, and $N(\omega)$ be the reference chirp symbol, received backscatter signal, and channel noise in the time domain and frequency domain, respectively. When the leader radio detects the backscatter signal, it multiplies incoming signals with the complex-conjugate copy of the reference chirp: $(p(t) + n(t))x^*(t)$. Next we prove $P_{CCS(0)}$ is the peak value of $(p(t) + n(t))x^*(t)$, and it changes monotonically with the strength of backscatter input signal $p(t)$.

Recall that multiplication in time domain is equivalent to the convolution in the frequency domain, we can rewrite the former expression as:

$$x^*(t)(p(t) + n(t)) = X^*(-\omega) * P(\omega) + X^*(-\omega) * N(\omega) \quad (4.1)$$

On the other hand, the cross-correlation can be represented as $X(\omega) \otimes P(\omega) = X(-\omega) * P(\omega)$ [178]. Hence we can rewrite above expression as:

$$x^*(t)(p(t) + n(t)) = X(\omega) \otimes P(\omega) + X(\omega) \otimes N(\omega) \quad (4.2)$$

where $X(\omega) \otimes N(\omega)$ is a constant noise term, $X(\omega) \otimes P(\omega)$ is the cross-correlation between the reference chirp and the backscatter signal, and ω is the cross-correlation lag. When In-N-Out detects the incoming backscatter signal, it synchronizes the reference chirp with this backscatter signal by shifting the reference chirp at the frequency domain. This operation leads to a cross-correlation peak (if there is a peak) shows at the zero lag position. Without loss of generality, we neglect the noise term of the above expression and use $P_{CCS(\omega)}$ to represent the frequency domain cross-correlation between the incoming backscatter signal and the reference

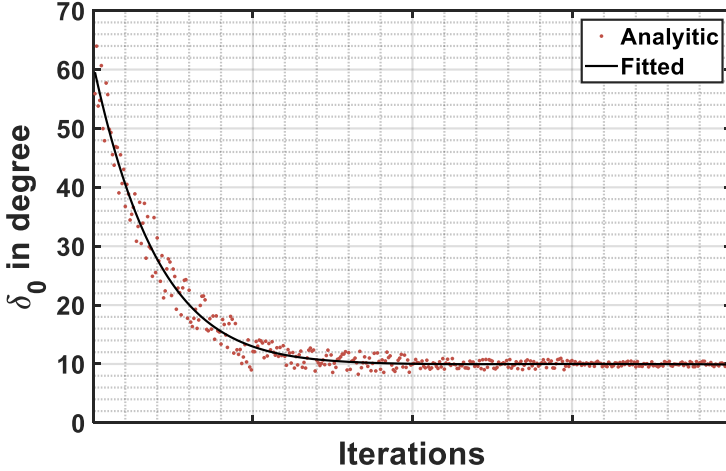


Figure 4.29: Optimal phase searching bond and its corresponding 7 order polynomial fitting curve in the context of backscatter assisted beamforming.

chirp.

$$\begin{aligned}
 P_{CCS(\omega)} &= X(\omega) \otimes P(\omega) \\
 &= \frac{1}{2\pi} \int_0^{2\pi} \left(\sum_{m=-\infty}^{\infty} x(-m) e^{i\sigma m} \right) \left(\sum_{k=-\infty}^{\infty} p(k) e^{-i(\omega-\sigma)k} \right) d\sigma \\
 &= \sum_{m=-\infty}^{\infty} x(-m) \sum_{k=-\infty}^{\infty} p(k) e^{-i\omega k} \frac{1}{2\pi} \int_0^{2\pi} (e^{-i\sigma(-m-k)}) d\sigma \\
 &= \sum_{m=-\infty}^{\infty} x(-m) \sum_{k=-\infty}^{\infty} p(k) e^{-i\omega k}.
 \end{aligned} \tag{4.3}$$

Hence the $P_{CCS(0)}$ (zero lag peak strength) can be expressed as:

$$P_{CCS(0)} = \sum_{m=-\infty}^{\infty} x(-m)p(m) \tag{4.4}$$

The above expression indicates that $P_{CCS(0)}$ is *linearly proportional* to the power of backscatter signal $p(\cdot)$. The leader radio thus adopts the power change of $P_{CCS(0)}$ as the indicator of the power change received at the backscatter.

4.10.2 Optimal phase searching bound estimation

According to the Proposition 3 in [179], the expected value of the beamforming amplitude after n^{th} period is:

$$y[n+1] = y[n](1 - p(1 - C_{\Phi})) + \frac{\sigma_1}{\sqrt{2\pi}} e^{-\frac{(y[n](1-C_{\Phi}))^2}{2\sigma_1}}. \quad (4.5)$$

where

$$\begin{aligned} p &= Q\left(\frac{y[n](1-C_{\Phi})}{\sigma_1}\right), \\ \sigma_1^2 &= \frac{N}{2}\left((1-C_{\Phi}^2) - \frac{I_2(\eta_n)}{I_0(\eta_n)}(C_{\Phi}^2 - C_{2\Phi})\right), \\ C_{\Phi} &\doteq E_{\Phi}(\cos\Phi_i), \\ I_k(x) &= \frac{1}{2\pi} \int_{-\pi}^{\pi} \cos(k\phi) e^{x\cos(\phi)} d\phi. \end{aligned} \quad (4.6)$$

where $I_k(x)$ is the modified first-kind, n-order Bessel function, η_n is characterized by $\frac{I_1(\eta_n)}{I_0(\eta_n)} = \frac{y[n]}{N}$. $Q(\cdot)$ is the tail distribution function of the standard normal distribution.

In the context of the backscatter assisted beamforming system. We first measure the backscatter signal power at different carrier signal power settings. These results are then fitted using a nonlinear function, which is denoted by $P_o = \wp(P_i)$. Combining this nonlinear function with Equation 4.5, we have:

$$y[n+1] = \wp(y[n](1 - p(1 - C_{\Phi})) + \frac{\sigma_1}{\sqrt{2\pi}} e^{-\frac{(y[n](1-C_{\Phi}))^2}{2\sigma_1}}). \quad (4.7)$$

At each time slot n , we can calculate the optimal distribution of phase searching bound $g_n(\Phi_i)$ by solving the following optimization problem:

$$\arg \max_{g_n(\Phi_i)} (y[n+1] - y[n]) \quad (4.8)$$

The problem of choosing an optimal distribution of phase searching bound is equivalent to the problem of finding the optimal variation of the phase searching bound. Given the fitted power function $P_o = \wp(P_i)$, We compute the optimal phase searching bond at each iterations and plot the result in Figure 4.29. To

minimize the jitters, we then fit this analytic result using a high order nonlinear polynomial curve function $\Phi = P(n)$. This function is then employed for setting the phase searching bound in each beamforming iteration.

Chapter 5

Conclusion and Proposed Research

5.1 Summary

This thesis lies deeply into the physical layer, and all research items are coherently aligned with beamforming and system level signal processing. We have re-explored lots of design and implementation details that have been largely overlooked before. Many new characteristics hidden deeply in the signals have been revealed. We have taken advantages of those new properties to address the three questions asked above. Compared to traditional beamforming structures, which generate a high energy path along the beam path between the phased array and the target, our approaches come from the inspiration of Fresnel zone plates [180] focus light. In our design, in a manner analogous to creating a Fresnel zone plate, we discretize the zone plates into multiple independent phase shifters. Each phase shifter is a far-field RF transmitter in our system. We establish a constructive superposition of these far-field emitters at the target receiver. By increasing the number of RF emitters, we find that we could focus the energy to desired locations. As such, our key contribution is to leverage this unique energy pattern of distributed antenna array to enable array of new IoT applications.

5.1.1 Contribution Summary

Overall, the key systems and contributions of this thesis are:

- A PHY layer secret communication approach for IoTs that requires no extra

jamming noise or the eavesdroppers' locations information.

- A distributed beamforming based WPT approach that can deliver higher RF power than traditional beamforming WPT methods under the same transfer distance and safety constraints.
- A software-hardware solution for deep tissue power transfer that enable charging the medical implant at a near-optimal power level, even when the implant moves around inside the human body.

5.2 End Note

Besides from the research items in my thesis, distributed beamforming technology can potentially enable much more novel applications. I would like to explore them in the future.

5.2.1 IoT identifications using PHY layer fingerprints

The MAC IP together with authentication protocols can take up to 90% of packet space in low energy IoT communications. Physical layer fingerprints are promising to replace the device IP and authentication bits. This could be an enormous energy saving and confidentiality gain for the emerging IoT. Distributed receiver beamforming can potentially enhance the PHY layer finger print. However, there are many challenges I need to address:

1. How to acquire a robust PHY layer fingerprints use distributed beamforming that are long lasting but can be used for differentiating the IoT devices itself at the same time?
2. How to handle mobility?
3. How to acquire strong enough PHY fingerprints that can fight against possible attack (PHY layer fingerprints stealth)?

5.2.2 Channel state information (CSI) inference for massive phase arrays

As the advances of microelectronics and small antenna designs, MIMO capability is possible for the future IoT. Accurate CSI estimation is required for each TX-RX pair and each sub-carriers within the communication bandwidth. But a full CSI matrix measurement is a large overhead and can even make the communication impossible (larger than channel coherent time). This research aims at answering following questions:

1. Given the layout of a phase array, can we infer the CSI information from a partially available CSI matrix?
2. How to resolve possible radio paths in order to do the channel inference?
3. Can we use deep learning approaches to solve this highly non-linear problem?

5.2.3 Make the sweet spot of your stereo follows you

This is my personal favourite. As the distributed beamforming enables a lot of applications in radio, we can also adapt this idea in acoustics. Realizing distributed beamforming in acoustic is much easier due to easier synchronization (much lower speed compare to EM wave). An exciting idea is to focus the acoustic wave adaptively to the target listeners. This will make the sweet spot of your stereo follows you. Nowadays, people buy expensive electronics to enlarge the sweet spot in a home theatre system. It can take up to 1 million US dollar to have a reasonable large size sweet spot in a home theatre system.

We have to address following challenges in this research:

1. What frequency bands affect the sweet spot?
2. Acoustic is wide band signal. How we realize beamforming in wide band signals?

3. How we make a light weight and small form factor device to provide feed-back?

5.2.4 RF interaction in Biology

We have collaborated with the cancer institute of New Jersey during the study of deep tissue power delivery. We found the focusing effect of distributed beam-forming might be very useful for cancer treatments, i.e, heating the tumor while keep other locations safe. On the other hand, we are also trying to study how weak RF signal alters biological behaviours in animals, such as the bee feeding and bird navigation. This research is now at primitive stages. I envision it can be very impactful in human daily life.

References

- [1] D. Arnitz and M. S. Reynolds, “Wireless power transfer optimization for nonlinear passive backscatter devices,” in *In IEEE RFID*, 2013.
- [2] J. Wang, H. Zhu, and N. J. Gomes, “Distributed antenna systems for mobile communications in high speed trains,” *IEEE JSAC*, 2012.
- [3] L. Dai, S. Zhou, and Y. Yao, “Capacity analysis in cdma distributed antenna systems,” *IEEE TWC*, 2005.
- [4] J. Xiong, K. Sundaresan, K. Jamieson, M. A. Khojastepour, and S. Rangarajan, “Midas: Empowering 802.11 ac networks with multiple-input distributed antenna systems,” in *In ACM CoNEXT*, 2014.
- [5] R. K Sheshadri, M. Y. Arslan, K. Sundaresan, S. Rangarajan, and D. Koutsoukolas, “Amorfi: amorphous wifi networks for high-density deployments,” in *In ACM CoNEXT*, 2016.
- [6] A. Swiston Jr, G. A. Ciccarelli, G. Traverso, S. Schwartz, T. Hughes, T. Boettcher, R. Barman, and R. Langer, “Physiologic status monitoring via the gastrointestinal tract,” Tech. Rep., 2015.
- [7] J. James, V. Iyer, Y. Chukewad, S. Gollakota, and S. B. Fuller, “Liftoff of a 190 mg laser-powered aerial vehicle: The lightest wireless robot to fly,” in *In IEEE ICRA*, 2018.
- [8] Y. Ma, Z. Luo, C. Steiger, G. Traverso, and F. Adib, “Enabling deep-tissue networking for miniature medical devices,” in *In ACM SIGCOMM*, 2018.
- [9] J. S. Ho, A. J. Yeh, E. Neofytou, S. Kim, Y. Tanabe, B. Patlolla, R. E. Beygui, and A. S. Poon, “Wireless power transfer to deep-tissue microimplants,” *Proceedings of the National Academy of Sciences*, 2014.
- [10] M. A. Hannan, S. Mutashar, S. A. Samad, and A. Hussain, “Energy harvesting for the implantable biomedical devices: issues and challenges,” *Biomedical engineering online*, 2014.
- [11] J. Kim and Y. Rahmat-Samii, “Implanted antennas inside a human body: Simulations, designs, and characterizations,” *IEEE Transactions on microwave theory and techniques*, 2004.

- [12] A. Surowiec, S. Stuchly, L. Eidus, and A. Swarup, “In vitro dielectric properties of human tissues at radiofrequencies,” *Physics in Medicine & Biology*, 1987.
- [13] I. Dove, “Analysis of radio propagation inside the human body for in-body localization purposes,” Master’s thesis, University of Twente, 2014.
- [14] S. Haykin, “Cognitive radio: Brain-empowered wireless communications,” *IEEE Journal on Selected Areas in Communications*, vol. 23, no. 2, pp. 201–220, 2005.
- [15] R. Liu and W. Trappe, *Securing Wireless Communications at the Physical Layer*. Springer, 2010.
- [16] S. Mathur, A. Reznik, C. Ye, R. Mukherjee, A. Rahman, Y. Shah, W. Trappe, and N. Mandayam, “Exploiting the Physical Layer for Enhanced Security,” *IEEE Wireless Communications Magazine*, vol. 17, pp. 63–70, 2010.
- [17] L. Xiao, Y. Li, G. Han, G. Liu, and W. Zhuang, “Phy-layer spoofing detection with reinforcement learning in wireless networks,” *IEEE Transactions on Vehicular Technology*, vol. 65, no. 12, pp. 10 037–10 047, 2016.
- [18] N. Anand, S.-J. Lee, and E. W. Knightly, “Strobe: Actively securing wireless communications using zero-forcing beamforming,” in *Proceedings of the IEEE Conference on Computer Communications (INFOCOM)*, 2012, pp. 720–728.
- [19] W.-C. Liao, T.-H. Chang, W.-K. Ma, and C.-Y. Chi, “Qos-based transmit beamforming in the presence of eavesdroppers: An optimized artificial-noise-aided approach,” *IEEE Transactions on Signal Processing*, vol. 59, no. 3, pp. 1202–1216, 2011.
- [20] L. Lai and H. El Gamal, “The Relay–Eavesdropper Channel: Cooperation for Secrecy,” *IEEE Transactions on Information Theory*, vol. 54, no. 9, pp. 4005–4019, 2008.
- [21] D. M. Laverty, D. J. Morrow, R. Best, and P. A. Crossley, “Telecommunications for Smart Grid: Backhaul Solutions for the Distribution Network,” in *Proceedings of the IEEE Power and Energy Society General Meeting*, 2010, pp. 1–6.
- [22] R. Mudumbai, B. Wild, U. Madhow, and K. Ramchandran, “Distributed beamforming using 1 bit feedback: from concept to realization,” in *In Cite-seer Allerton*, 2006.
- [23] Z. Li, R. Yates, and W. Trappe, “Achieving Secret Communication for Fast Rayleigh Fading Channels,” *IEEE Transactions on Wireless Communications*, vol. 9, no. 9, pp. 2792 –2799, September 2010.

- [24] S. Goel and R. Negi, "Guaranteeing secrecy using artificial noise," *IEEE Transactions on Wireless Communications*, vol. 7, no. 6, pp. 2180–2189, June 2008.
- [25] S. Gollakota and D. Katabi, "Physical layer wireless security made fast and channel independent," in *Proceedings IEEE INFOCOM*, April 2011, pp. 1125–1133.
- [26] A. Yener and S. Ulukus, "Wireless physical-layer security: Lessons learned from information theory," *Proceedings of the IEEE*, vol. 103, no. 10, pp. 1814–1825, Oct 2015.
- [27] L. Dong, Z. Han, A. P. Petropulu, and H. V. Poor, "Improving wireless physical layer security via cooperating relays," *IEEE Transactions on Signal Processing*, vol. 58, no. 3, pp. 1875–1888, Mar. 2010.
- [28] L. Liu, R. Zhang, and K.-C. Chua, "Secrecy wireless information and power transfer with miso beamforming," in *Global Communications Conference (GLOBECOM), 2013 IEEE*. IEEE, 2013.
- [29] S. Bashar, Z. Ding, and C. Xiao, "On the secrecy rate of multi-antenna wiretap channel under finite-alphabet input," *IEEE Communications Letters*, vol. 15, no. 5, pp. 527–529, May 2011.
- [30] J. V. Michalowicz, J. M. Nichols, and F. Bucholtz, "Calculation of differential entropy for a mixed gaussian distribution," *Entropy*, vol. 10, no. 3, pp. 200–206, Aug 2008.
- [31] G. Webb, I. Minin, and O. V. Minin, "Variable reference phase in diffractive antennas: Review, applications, new results," *IEEE Antennas and Propagation Magazine*, vol. 53, no. 2, pp. 77–94, Apr. 2011.
- [32] M. Graule, P. Chirarattananon, S. Fuller, N. Jafferis, K. Ma, M. Spenko, R. Kornbluh, and R. Wood, "Perching and takeoff of a robotic insect on overhangs using switchable electrostatic adhesion," *Science*, 2016.
- [33] M. Gorlatova, R. Margolies, J. Sarik, G. Stanje, J. Zhu, B. Vigraham, M. Szczodrak, L. Carloni, P. Kinget, I. Kymmissis *et al.*, "Prototyping energy harvesting active networked tags (enhants)," in *In IEEE INFOCOM*, 2013.
- [34] V. Talla, B. Kellogg, B. Ransford, S. Naderiparizi, S. Gollakota, and J. R. Smith, "Powering the next billion devices with wi-fi," in *In ACM CoNext*, 2015.
- [35] V. Liu, A. Parks, V. Talla, S. Gollakota, D. Wetherall, and J. R. Smith, "Ambient backscatter: wireless communication out of thin air," *In ACM SIGCOMM*, 2013.

- [36] M. J. Chabalko, M. Shahmohammadi, and A. P. Sample, “Quasistatic cavity resonance for ubiquitous wireless power transfer,” *PloS ONE*, 2017.
- [37] J. Jadian and D. Katabi, “Magnetic mimo: How to charge your phone in your pocket,” in *In ACM MobiCom*, 2014.
- [38] B. Griffin and C. Detweiler, “Resonant wireless power transfer to ground sensors from a uav,” in *In IEEE ICRA*, 2012.
- [39] V. Iyer, E. Bayati, R. Nandakumar, A. Majumdar, and S. Gollakota, “Charging a smartphone across a room using lasers,” *Proceedings of the ACM on Interactive, Mobile, Wearable and Ubiquitous Technologies*, 2018.
- [40] “Ossia just released a wireless charger kit that works like wifi,” Webpage.
- [41] H. Krim and M. Viberg, “Two decades of array signal processing research: the parametric approach,” *IEEE Signal Processing Magazine*, 1996.
- [42] “Agricultural drones relatively cheap drones with advanced sensors and imaging capabilities are giving farmers new ways to increase yields and reduce crop damage,” Webpage.
- [43] “Robots, drones and heart-detectors: How disaster technology is saving lives,” Webpage.
- [44] “The next generation of robotic assembly lines are emerging,” Webpage.
- [45] B. Firner, S. Medhekar, Y. Zhang, R. Howard, W. Trappe, P. Wolniansky, and E. Fenson, “Pip tags: Hardware design and power optimization,” in *In ACM HotEmNets*, 2008.
- [46] “Definition on near and far field,” Webpage.
- [47] “Highly resonant wireless power transfer: Safe, efficient, and over distance,” Webpage.
- [48] “Pi wireless charging,” Webpage.
- [49] X. Lu, P. Wang, D. Niyato, D. I. Kim, and Z. Han, “Wireless charging technologies: Fundamentals, standards, and network applications,” *IEEE Communications Surveys & Tutorials*, 2016.
- [50] S. Kim, J. S. Ho, L. Y. Chen, and A. S. Poon, “Wireless power transfer to a cardiac implant,” *Applied Physics Letters*, 2012.
- [51] A. Madhja, S. Nikoletseas, and T. P. Raptis, “Distributed wireless power transfer in sensor networks with multiple mobile chargers,” *Computer Networks*, 2015.

- [52] F. Zhang, S. A. Hackworth, X. Liu, H. Chen, R. J. Sclabassi, and M. Sun, “Wireless energy transfer platform for medical sensors and implantable devices,” in *In IEEE EMBC*, 2009.
- [53] W. C. Brown, “Experimental airborne microwave supported platform,” DTIC Document, Tech. Rep., 1965.
- [54] “Fcc approves first wireless ‘power-at-a-distance’ charging system,” Web-page.
- [55] M. R. V. Moghadam and R. Zhang, “Node placement and distributed magnetic beamforming optimization for wireless power transfer,” *IEEE Transactions on Signal and Information Processing over Networks*, 2017.
- [56] R. Wang, R. David, and D. R. Brown, “Feedback rate optimization in receiver-coordinated distributed transmit beamforming for wireless power transfer,” in *In IEEE CISS*, 2015.
- [57] U. Muncuk, S. Mohanti, K. Alemdar, M. Y. Naderi, and K. R. Chowdhury, “Software-defined wireless charging of internet of things using distributed beamforming: Demo abstract,” in *In ACM SenSys*, 2016.
- [58] H. Nittby, B. Widegren, M. Krogh, G. Grafström, H. Berlin, G. Rehn, J. L. Eberhardt, L. Malmgren, B. R. Persson, and L. G. Salford, “Exposure to radiation from global system for mobile communications at 1,800 mhz significantly changes gene expression in rat hippocampus and cortex,” *The Environmentalist*, vol. 28, no. 4, pp. 458–465, 2008.
- [59] S. Engels, N.-L. Schneider, N. Lefeldt, C. M. Hein, M. Zapka, A. Michalik, D. Elbers, A. Kittel, P. Hore, and H. Mouritsen, “Anthropogenic electromagnetic noise disrupts magnetic compass orientation in a migratory bird,” *Nature*, 2014.
- [60] J. L. Kirschvink, “Sensory biology: Radio waves zap the biomagnetic compass,” *Nature*, 2014.
- [61] O. P. Gandhi, L. L. Morgan, A. A. de Salles, Y.-Y. Han, R. B. Herberman, and D. L. Davis, “Exposure limits: the underestimation of absorbed cell phone radiation, especially in children,” *Electromagnetic Biology and Medicine*, vol. 31, no. 1, pp. 34–51, 2012.
- [62] M. Havas, J. Marrongelle, B. Pollner, E. Kelley, C. R. Rees, and L. Tully, “Provocation study using heart rate variability shows microwave radiation from 2.4 ghz cordless phone affects autonomic nervous system,” *European Journal of Oncology Library*, vol. 5, pp. 273–300, 2010.
- [63] M. P. Ntzouni, A. Skouroliakou, N. Kostomitsopoulos, and L. H. Margaritis, “Transient and cumulative memory impairments induced by gsm 1.8 ghz

- cell phone signal in a mouse model,” *Electromagnetic biology and medicine*, vol. 32, no. 1, pp. 95–120, 2013.
- [64] “Oet bulletin no. 65 (august 1997),” Webpage, 1997.
 - [65] G. Melia, “Electromagnetic absorption by the human body from 1-15 ghz,” Ph.D. dissertation, University of York, 2013.
 - [66] “Fcc part 15,” , 2010.
 - [67] H. Dai, Y. Liu, G. Chen, X. Wu, and T. He, “Safe charging for wireless power transfer,” in *INFOCOM, 2014 Proceedings IEEE*. IEEE, 2014, pp. 1105–1113.
 - [68] U. Martin and M. Grigat, “A statistical simulation model for the directional mobile radio channel and its configuration,” in *Spread Spectrum Techniques and Applications Proceedings, 1996., IEEE 4th International Symposium on*, vol. 1. IEEE, 1996, pp. 86–90.
 - [69] X. Fan, Z. Zhang, W. Trappe, Y. Zhang, R. E. Howard, and Z. Han, “Secret-focus: A practical physical layer secret communication system by perturbing focused phases in distributed beamforming,” in *In IEEE INFOCOM*, 2018.
 - [70] A. J. Paulraj, D. A. Gore, R. U. Nabar, and H. Bolcskei, “An overview of mimo communications-a key to gigabit wireless,” *Proceedings of the IEEE*, vol. 92, no. 2, pp. 198–218, 2004.
 - [71] R. Rogalin, O. Y. Bursalioglu, H. Papadopoulos, G. Caire, A. F. Molisch, A. Michaloliakos, V. Balan, and K. Psounis, “Scalable synchronization and reciprocity calibration for distributed multiuser mimo,” *IEEE Transactions on Wireless Communications*, 2014.
 - [72] F. Kaltenberger, H. Jiang, M. Guillaud, and R. Knopp, “Relative channel reciprocity calibration in mimo/tdd systems,” in *Future Network and Mobile Summit, 2010.* IEEE, 2010.
 - [73] J.-C. Guey and L. D. Larsson, “Modeling and evaluation of mimo systems exploiting channel reciprocity in tdd mode,” in *Vehicular Technology Conference, 2004. VTC2004-Fall. 2004 IEEE 60th.* IEEE, 2004.
 - [74] M. Guillaud, D. T. Slock, and R. Knopp, “A practical method for wireless channel reciprocity exploitation through relative calibration.” in *ISSPA*, 2005.
 - [75] T. Wang, Y. Liu, and A. V. Vasilakos, “Survey on channel reciprocity based key establishment techniques for wireless systems,” *Wireless Networks*, 2015.

- [76] Y. Han, J. Ni, and G. Du, “The potential approaches to achieve channel reciprocity in fdd system with frequency correction algorithms,” in *In IEEE CHINACOM*, 2010.
- [77] P. W. Chan, E. S. Lo, R. R. Wang, E. K. Au, V. K. Lau, R. S. Cheng, W. H. Mow, R. D. Murch, and K. B. Letaief, “The evolution path of 4g networks: Fdd or tdd?” *IEEE Communications Magazine*, 2006.
- [78] A. P. Dempster, N. M. Laird, and D. B. Rubin, “Maximum likelihood from incomplete data via the em algorithm,” *Journal of the royal statistical society. Series B (methodological)*, 1977.
- [79] R. Mudumbai, J. Hespanha, U. Madhow, and G. Barriac, “Scalable feedback control for distributed beamforming in sensor networks,” in *In IEEE ISIT*, 2005.
- [80] P. J. Van Laarhoven and E. H. Aarts, “Simulated annealing,” in *Simulated annealing: Theory and applications*. Springer, 1987.
- [81] F. Qutin, U. Madhow, M. M. U. Rahman, and R. Mudumbai, “Demonstrating distributed transmit beamforming with software-defined radios,” in *In IEEE WoWMoM*, 2012.
- [82] F. Qutin, M. M. U. Rahman, R. Mudumbai, and U. Madhow, “Distributed beamforming with software-defined radios: frequency synchronization and digital feedback,” in *In IEEE GLOBECOM*, 2012.
- [83] Y. Zhang, B. Firner, R. Howard, R. Martin, N. Mandayam, J. Fukuyama, and C. Xu, “Transmit only: An ultra low overhead mac protocol for dense wireless systems,” in *In IEEE SMARTCOMP*, 2017.
- [84] B. Firner, R. S. Moore, R. Howard, R. P. Martin, and Y. Zhang, “Poster: Smart buildings, sensor networks, and the internet of things,” in *In ACM SenSys*, 2011.
- [85] “Datasheet of powercast p2110 harvester chip,” Webpage.
- [86] “Agilent e4405b spectrum analyzer,” 2016, <http://literature.cdn.keysight.com/litweb/pdf/E4401-90473.pdf>.
- [87] M. Quigley, K. Conley, B. Gerkey, J. Faust, T. Foote, J. Leibs, R. Wheeler, and A. Y. Ng, “Ros: an open-source robot operating system,” in *ICRA workshop on open source software*. Kobe, 2009.
- [88] “Pioneer p3-dx robot,” Webpage, 2011.
- [89] Q. Bonnard, G. Zufferey, A. Mazzei, S. Cuendet, N. Li, and P. Dillenbourg, “Chilitags: Robust fiducial markers for augmented reality,” *CHILI, EPFL, Switzerland*, 2013.

- [90] “Compare your daughterboard’s data from,” Webpage, 2015.
- [91] W. Khan, E. Muntimadugu, M. Jaffe, and A. J. Domb, “Implantable medical devices,” in *Focal controlled drug delivery*. Springer, 2014.
- [92] “Prosthesis,” Webpage, 2019.
- [93] “Cochlear Implants,” Webpage, 2009.
- [94] “Transvaginal mesh to fix pelvic organ prolapse,” Webpage, 2019.
- [95] “Pacemaker,” Webpage, 2019.
- [96] “Nuclear power battery lasts 12 years,” Webpage, 2005.
- [97] M. Rasouli and L. S. J. Phee, “Energy sources and their development for application in medical devices,” *Expert review of medical devices*, 2010.
- [98] M. Armand and J.-M. Tarascon, “Building better batteries,” *nature*, 2008.
- [99] “Pacemaker battery replacement causes cardiac arrest,” Webpage, 2012.
- [100] E. E. Gul and M. Kayrak, “Common pacemaker problems: lead and pocket complications,” in *Modern Pacemakers-Present and Future*. InTech, 2011.
- [101] “Wardenclyffe Tower,” Webpage, 2019.
- [102] J. Schuler, “High-level electromagnetic energy transfer through a closed chest wall,” *IRE International Conv. Rec. pt 9*, 1961.
- [103] B. Lenaerts and R. Puers, “An inductive power link for a wireless endoscope,” *Biosensors and Bioelectronics*, 2007.
- [104] U.-M. Jow and M. Ghovanloo, “Design and optimization of printed spiral coils for efficient transcutaneous inductive power transmission,” *IEEE Transactions on biomedical circuits and systems*, 2007.
- [105] J. M. Donelan, Q. Li, V. Naing, J. Hoffer, D. Weber, and A. D. Kuo, “Biomechanical energy harvesting: generating electricity during walking with minimal user effort,” *Science*, 2008.
- [106] A. K. RamRakhiani, S. Mirabbasi, and M. Chiao, “Design and optimization of resonance-based efficient wireless power delivery systems for biomedical implants,” *IEEE Transactions on Biomedical Circuits and Systems*, 2011.
- [107] “Wirelessly charging medical devices breakthrough brings new solution,” Webpage, 2018.
- [108] “Implants and Prosthetics,” Webpage, 2019.

- [109] X. Fan, H. Ding, S. Li, M. Sanzari, Y. Zhang, W. Trappe, Z. Han, and R. E. Howard, “Energy-ball: Wireless power transfer for batteryless internet of things through distributed beamforming,” *Proceedings of the ACM on Interactive, Mobile, Wearable and Ubiquitous Technologies*, 2018.
- [110] X. Fan, Z. Qi, Z. Jia, and Y. Zhang, “Enabling concurrent iot transmissions in distributed c-ran,” in *ACM SenSys*, 2018.
- [111] X. Fan, “Facilitating the deployment of next billion iot devices with distributed antenna systems,” in *The ACM MobiSys 2019 on Rising Stars Forum*, 2019.
- [112] “Expected lifetime analysis for medical devices,” Webpage, 2017.
- [113] V. S. Mallela, V. Ilankumaran, and N. S. Rao, “Trends in cardiac pacemaker batteries,” *Indian pacing and electrophysiology journal*, 2004.
- [114] “The real-life applications of IoT and why battery life is critical,” Webpage, 2019.
- [115] H.-K. Cha, W.-T. Park, and M. Je, “A cmos rectifier with a cross-coupled latched comparator for wireless power transfer in biomedical applications,” *IEEE Transactions on Circuits and Systems II: Express Briefs*, 2012.
- [116] A. Kiourtzi and K. S. Nikita, “A review of implantable patch antennas for biomedical telemetry: Challenges and solutions [wireless corner],” *IEEE Antennas and Propagation Magazine*, 2012.
- [117] “Gastroscopy,” Webpage, 2019.
- [118] D. Tse and P. Viswanath, *Fundamentals of wireless communication*. Cambridge university press, 2005.
- [119] G. R. Rani and G. Raju, “Transmission and reflection characteristics of electromagnetic energy in biological tissues,” *International Journal of Electronics and Communication Engineering*, 2013.
- [120] A. Stango, K. Y. Yazdandoost, F. Negro, and D. Farina, “Characterization of in-body to on-body wireless radio frequency link for upper limb prostheses,” *PloS one*, 2016.
- [121] C. W. Kim and T. S. P. See, “Rf transmission power loss variation with abdominal tissues thicknesses for ingestible source,” in *In IEEE Healthcom*, 2011.
- [122] P. Zhang, M. Rostami, P. Hu, and D. Ganesan, “Enabling practical backscatter communication for on-body sensors,” in *In ACM SIGCOMM*, 2016.

- [123] V. Talla, M. Hessar, B. Kellogg, A. Najafi, J. R. Smith, and S. Gollakota, “Lora backscatter: Enabling the vision of ubiquitous connectivity,” *Proceedings of the ACM on Interactive, Mobile, Wearable and Ubiquitous Technologies*, 2017.
- [124] M. Hervás, R. Alsina-Pagès, F. Orga, D. Altadill, J. Pijoan, and D. Badia, “Narrowband and wideband channel sounding of an antarctica to spain ionospheric radio link,” *Remote Sensing*, 2015.
- [125] P. Hu, P. Zhang, M. Rostami, and D. Ganesan, “Braido: An integrated active-passive radio for mobile devices with asymmetric energy budgets,” in *In ACM SIGCOMM*, 2016.
- [126] “LoraWAN Specification v1.3,” Webpage, 2017.
- [127] K. Olsson and S. Finnsson, “Exploring lora and lorawan,” 2017.
- [128] “Usrp n210 minimum detectable signal strength,” Webpage, 2012.
- [129] R. G. Brown, P. Y. Hwang *et al.*, *Introduction to random signals and applied Kalman filtering*. Wiley New York, 1992.
- [130] “Monza r6 datasheet,” Webpage, 2019.
- [131] J. Wang, J. Zhang, R. Saha, H. Jin, and S. Kumar, “Pushing the range limits of commercial passive rfids,” in *In USENIX NSDI*, 2019.
- [132] “WBX 50-2200 MHz Rx/Tx (40 MHz),” Webpage, 2019.
- [133] “ZFL-1000VH+ 10-1000 MHz high dynamic range RF amplifier,” Webpage, 2019.
- [134] “Apex II TG.35 antenna ,” Webpage, 2019.
- [135] “E4405B ESA-E spectrum analyzer,” Webpage, 2019.
- [136] “OctoClock-G CDA-2990,” Webpage, 2019.
- [137] E. Hamed, H. Rahul, and B. Partov, “Chorus: truly distributed distributed-mimo,” in *In ACM SIGCOMM*, 2018.
- [138] H. S. Rahul, S. Kumar, and D. Katabi, “Jmb: scaling wireless capacity with user demands,” in *In ACM SIGCOMM*, 2012.
- [139] “FCC Rules for Unlicensed Wireless Equipment operating in the ISM bands,” Webpage, 2019.
- [140] “CFR - Code of Federal Regulations Title 21,” Webpage, 2019.
- [141] “RF power density calculator,” Webpage, 2019.

- [142] D. Halperin, T. S. Heydt-Benjamin, B. Ransford, S. S. Clark, B. Defend, W. Morgan, K. Fu, T. Kohno, and W. H. Maisel, “Pacemakers and implantable cardiac defibrillators: Software radio attacks and zero-power defenses,” in *In IEEE Symposium on Security and Privacy*, 2008.
- [143] A. Amar, A. Kouki, and H. Cao, “Power approaches for implantable medical devices,” *sensors*, 2015.
- [144] A. Kurs, A. Karalis, R. Moffatt, J. D. Joannopoulos, P. Fisher, and M. Soljačić, “Wireless power transfer via strongly coupled magnetic resonances,” *science*, 2007.
- [145] C. Zhang, S. Kumar, and D. Bharadia, “Capttery: Scalable battery-like room-level wireless power,” in *In ACM MobiSys*, 2019.
- [146] A. K. RamRakhiani and G. Lazzi, “On the design of efficient multi-coil telemetry system for biomedical implants,” *IEEE Transactions on Biomedical Circuits and Systems*, 2013.
- [147] M. Kiani, U.-M. Jow, and M. Ghovanloo, “Design and optimization of a 3-coil inductive link for efficient wireless power transmission,” *IEEE transactions on biomedical circuits and systems*, 2011.
- [148] A. Arbabian, T. C. Chang, M. L. Wang, J. Charthad, S. Baltsavias, M. Fal-lahpour, and M. J. Weber, “Sound technologies, sound bodies: Medical implants with ultrasonic links,” *IEEE Microwave Magazine*, 2016.
- [149] E. Falkenstein, M. Roberg, and Z. Popovic, “Low-power wireless power delivery,” *IEEE Transactions on microwave theory and techniques*, 2012.
- [150] C. Liu, Y.-X. Guo, H. Sun, and S. Xiao, “Design and safety considerations of an implantable rectenna for far-field wireless power transfer,” *IEEE Transactions on antennas and Propagation*, 2014.
- [151] E. Y. Chow, A. L. Chlebowski, S. Chakraborty, W. J. Chappell, and P. P. Irazoqui, “Fully wireless implantable cardiovascular pressure monitor integrated with a medical stent,” *IEEE Transactions on Biomedical Engineering*, 2010.
- [152] A. Karalis, J. D. Joannopoulos, and M. Soljačić, “Efficient wireless non-radiative mid-range energy transfer,” *Annals of physics*, 2008.
- [153] V. Iyer, R. Nandakumar, A. Wang, S. B. Fuller, and S. Gollakota, “Living iot: A flying wireless platform on live insects,” in *In ACM MobiCom*, 2019.
- [154] S. Mohanti, E. Bozkaya, M. Y. Naderi, B. Canberk, and K. Chowdhury, “Wifed: Wifi friendly energy delivery with distributed beamforming,” in *In IEEE INFOCOM*, 2018.

- [155] A. S. Poon, S. O'Driscoll, and T. H. Meng, "Optimal frequency for wireless power transmission into dispersive tissue," *IEEE Transactions on Antennas and Propagation*, 2010.
- [156] T. Maleki, N. Cao, S. H. Song, C. Kao, S.-C. Ko, and B. Ziaie, "An ultrasonically powered implantable micro-oxygen generator (imog)," *IEEE transactions on Biomedical Engineering*, 2011.
- [157] S.-n. Suzuki, S. Kimura, T. Katane, H. Saotome, O. Saito, and K. Kobayashi, "Power and interactive information transmission to implanted medical device using ultrasonic," *Japanese journal of applied physics*, 2002.
- [158] R. Guida, G. E. Santagati, and T. Melodia, "A 700 khz ultrasonic link for wireless powering of implantable medical devices," in *In IEEE SENSORS*, 2016.
- [159] G. E. Santagati and T. Melodia, "U-wear: Software-defined ultrasonic networking for wearable devices," in *In ACM MobiSys*, 2015.
- [160] ——, "An implantable low-power ultrasonic platform for the internet of medical things," in *In IEEE INFOCOM*, 2017.
- [161] R. Guida, N. Dave, F. Restuccia, E. Demirors, and T. Melodia, "U-verse: a miniaturized platform for end-to-end closed-loop implantable internet of medical things systems," in *In ACM SenSys*, 2019.
- [162] Y. Peng, L. Shangguan, Y. Hu, Y. Qian, X. Lin, X. Chen, D. Fang, and K. Jamieson, "Plora: A passive long-range data network from ambient lora transmissions," in *In ACM SIGCOMM*, 2018.
- [163] Y. Ma, N. Selby, and F. Adib, "Drone relays for battery-free networks," in *In ACM SIGCOMM*, 2017.
- [164] B. Kellogg, V. Talla, S. Gollakota, and J. R. Smith, "Passive wi-fi: Bringing low power to wi-fi transmissions." in *In USENIX NSDI*, 2016.
- [165] M. Hessar, A. Najafi, and S. Gollakota, "Netscatter: Enabling large-scale backscatter networks." in *In USENIX NSDI*, 2019.
- [166] Y. Ma, N. Seby, and F. Adib, "Minding the billions: Ultra-wideband localization for deployed rfid tags," in *In ACM MobiCom*, 2017.
- [167] L. Shangguan and K. Jamieson, "The design and implementation of a mobile rfid tag sorting robot," in *In ACM MobiSys*, 2016.
- [168] D. Vasisht, G. Zhang, O. Abari, H.-M. Lu, J. Flanz, and D. Katabi, "In-body backscatter communication and localization," in *In ACM SIGCOMM*, 2018.

- [169] J. Wang, J. Xiong, X. Chen, H. Jiang, R. K. Balan, and D. Fang, “Tagscan: Simultaneous target imaging and material identification with commodity rfid devices,” in *In ACM MobiCom*, 2017.
- [170] U. Ha, Y. Ma, Z. Zhong, T.-M. Hsu, and F. Adib, “Learning food quality and safety from wireless stickers,” in *In ACM HotNets*, 2018.
- [171] O. Abari, D. Vasisht, D. Katabi, and A. Chandrakasan, “Caraoke: An e-toll transponder network for smart cities,” in *In ACM SIGCOMM*, 2015.
- [172] E. Denicke, H. Hartmann, N. Peitzmeier, and B. Geck, “Backscatter beam-forming: A transponder for novel mimo rfid transmission schemes,” *IEEE Journal of Radio Frequency Identification*, 2018.
- [173] “MSP430 Datasheet,” Webpage, 2019.
- [174] “MAX2235 Datasheet,” Webpage, 2019.
- [175] “SN74LS624N Datasheet,” Webpage, 2019.
- [176] “cc1100 Datasheet,” Webpage, 2019.
- [177] “W5017 Datasheet,” Webpage, 2019.
- [178] “Cross-correlation ,” Webpage, 2019.
- [179] R. Mudumbai, *Energy efficient wireless communication using distributed beamforming*. University of California, Santa Barbara, 2007.
- [180] “Fresnel zone plates,” Webpage.